Rochester Institute of Technology

RIT Digital Institutional Repository

Theses

1-16-2014

Reduction of Line Edge Roughness (LER) in Interference-Like Large Field Lithography

Burak Baylav

Follow this and additional works at: https://repository.rit.edu/theses

Recommended Citation

Baylav, Burak, "Reduction of Line Edge Roughness (LER) in Interference-Like Large Field Lithography" (2014). Thesis. Rochester Institute of Technology. Accessed from

This Dissertation is brought to you for free and open access by the RIT Libraries. For more information, please contact repository@rit.edu.

R·I·T

REDUCTION OF LINE EDGE ROUGHNESS (LER) IN INTERFERENCE-LIKE LARGE FIELD LITHOGRAPHY

by

Burak Baylav

A dissertation submitted in partial fulfillment of the requirements for the degree of Doctorate of Philosophy in Microsystems Engineering

Microsystems Engineering Program
Kate Gleason College of Engineering

Rochester Institute of Technology
Rochester, New York

January 16, 2014

REDUCTION OF LINE EDGE ROUGHNESS (LER) IN INTERFERENCE-LIKE LARGE FIELD LITHOGRAPHY

by

Burak Baylav

Committee Approval:

We, the undersigned committee members, certify that we have advised and/or supervised the candidate on the work described in this dissertation. We further certify that we have reviewed the dissertation manuscript and approve it in partial fulfillment of the requirements of the degree of Doctor of Philosophy in Microsystems Engineering.

Dr. Bruce W. Smith — Date
Committee Chair and Dissertation Advisor

Dr. Robert Pearson — Date
Committee Member

Dr. Zhaolin Lu — Date
Committee Member

Dr. Mark Schattenburg — Date
Committee Member

Dr. Pawitter Mangat — Date
Committee Member

Certified by:

Dr. Bruce W. Smith — Date
Director, Microsystems Engineering Program

Dr. Harvey J. Palmer — Date
Dean, Kate Gleason College of Engineering

ABSTRACT

Kate Gleason College of Engineering
Rochester Institute of Technology

Degree: Doctor of Philosophy **Program:** Microsystems Engineering

Author's Name: Burak Baylav

Advisor's Name: Dr. Bruce W. Smith

Dissertation Title: REDUCTION OF LINE EDGE ROUGHNESS (LER) IN INTERFERENCE-LIKE LARGE FIELD LITHOGRAPHY

Line edge roughness (LER) is seen as one of the most crucial challenges to be addressed in advanced technology nodes. In order to alleviate it, several options were explored in this work for the interference-like lithography imaging conditions.

The most straight forward option was to scale interference lithography (IL) for large field integrated circuit (IC) applications. IL not only serves as a simple method to create high resolution period patterns, but, it also provides the highest theoretical contrast achievable compared to other optical lithography systems. Higher contrast yields a smaller transition region between the low and high intensity parts of the image, therefore, inherently lowers LER. Two of the challenges that would prohibit scaling IL for large field IC applications were addressed in this work: (1) field size limitations, and (2) magnification correction (i.e., pitch fine-tuning) ability.

Experimental results showed less than 0.5 nm pitch adjustment capability using fused silica wedges mounted on rotational stages at 300 nm pitch pattern. A detailed discussion on maximum practical IL field size was outlined by considering the subsequent trim exposures and optical path difference effects between the interfering diffraction orders. The practical limit on the IL field size was assessed to be 10 mm for the conditions specified in this work.

One of the contributors of LER is the mask absorber roughness. To mitigate it, two methods were explored that are also applicable to scanners working under interference-like conditions: (1) aerial image averaging via directional translation, and (2) pupil plane filtering. Experiments on pupil plane filtering approach were performed at Imec in Leuven, Belgium, on the ASML:NXT1950i scanner equipped with FlexWAVE wavefront manipulator. Utilizing an optimized phase filter at the pupil plane and a programmed roughness mask, the transfer of 200 nm roughness period to the wafer plane was eliminated. This mitigation effect was found to be strongly dependent on the focus.

ACKNOWLEDGMENTS

Here, I would like to acknowledge the people who helped me to grow not only as an aspiring researcher in a challenging field, but also inspired me to be a better person in a challenging world in the recent years of my life.

Earning the doctorate degree was not an easy task, at times it felt draining both physically and emotionally. The following people will forever have my gratitude for being my support, my teacher, my rock, my advisor, my friend, my colleague and more importantly my believer even when I started to doubt myself.

I would like to thank Dr. Bruce Smith for introducing me to the field of nanolithography. Since the day I met him, he inspired me to be an innovative researcher. He has given me many opportunities that led me to where I am today. I am also thankful to my past and present group members Chris Maloney, Zac Levinson, Andrew Estroff, Germain Fenger, Andrew Burbine, Monica Sears, Peng Xie, Neal Lafferty, Anatoly Bourov, Jianming Zhao, and Steve Smith. Anytime I felt stuck or felt frustrated, our brainstorming and heated discussions always helped me solve the challenges I faced. I also want to thank our department secretary Lisa Zimmerman for tirelessly answering the most tedious questions I had, always with a warm smile on her face. I will miss them dearly.

I would also like to thank my committee members Dr. Pawitter Mangat, Dr. Mark Schattenburg, Dr. Robert Pearson, and Dr. Zhaolin Lu for their invaluable guidance and helpful insight throughout the research.

I don't think I would be able to finish this work without the support I got from Matt Burgess, my mom Nisa Serefli, my brothers Murat Baylav and Mert Baylav. They believed in me and encouraged me whenever I felt depressed and exhausted which happened more than one occasion, especially towards the end. I know the sacrifices they have made for me; I can only hope they know how much I appreciate them.

I would like to thank IMEC research facility in Leuven, Belgium, for their help with important parts of the experiments. I would like to especially acknowledge Joost Bekaert and Alessandro Vaglio Pret, both of whom are extremely knowledgeable and great people that I admire.

Finally, this work was made possible with the financial aid from Semiconductor Research Corporation (SRC), Global Research Corporation (GRC) and GLOBALFOUNDRIES through the task number 2126.002. I also acknowledge EUV Technology's SuMMIT and KLA Tencor's PROLITH™ for the free use of their software.

Table of Contents

Abstract i
Acknowledgments ii
List of Figures vi
List of Tables xiii
List of Acronyms xiv
1. Introduction to Lithography 1
1.1 Background of Lithography 2
1.2 Excimer Laser Review 4
1.3 Next Generation Lithography (NGL) Approaches 6
1.3.1 Double patterning (DP) technology 7
1.3.2 EUV lithography technology 8
1.3.3 Maskless lithography technology 9
1.3.4 Nanoimprint lithography technology 10
1.3.5 Directed self-assembly technology 12
1.3.6 Interference lithography 14
1.4 One Dimensional Regular Design Approaches 17
1.5 Problem Statement 18
2. Theory and Background 21
2.1 Coherent Image Formation 21
2.1.1 Effect of partial coherence on imaging 24
2.1.2 Effect of aberrations on imaging 26
2.1.3 Effect of vibration on imaging 27
2.2 Reduction Talbot Specific Derivations 31
2.2.1 Effect of OPD on field size 35
2.3 Line Edge Roughness (LER) 37
2.3.1 Mask roughness transfer 47
2.3.2 Previous LER mitigation attempts 51
2.4 Speckle Theory in Imaging 53
2.5 Pupil Filtering Applications 56
2.6 Previous Large Field IL Attempts 57

2.7 Translational Image Averaging: Characterization and Measurement 60
3. Approach and Experimental Procedure 65
3.1 IL Specific LER Mitigation Studies 65
3.1.1 Translational image averaging for LER smoothing 65
3.1.2 Pupil plane filtering 71
3.2 Magnification Correction Studies for Machine Mix and Match 85
3.2.1 Approach 86
3.2.2 Experimental procedure 88
3.3 Effect of OPD on Field Size 89
3.3.1 Approach 91
3.3.2 Experimental procedure 93
4. Results and Discussions 95
4.1 IL Specific LER Mitigation Studies 95
4.1.1 Aerial image averaging via directional translation 95
4.1.2 Pupil plane filtering 102
4.2 Magnification Correction Results 114
4.3 Maskless IL Results 115
5. CONCLUSIONS 117
6. Appendix A 119
7. Appendix B 123
8. Appendix C 130
9. References 136

LIST OF FIGURES

Figure 1.1: A simplified schematic of a projection lens system. 2

Figure 1.2: Lithography exposure tool potential solutions for MPU and DRAM 7

Figure 1.3: Process flows for DE, DP, and SP approaches 8

Figure 1.4: Comparison of DUV and EUV aerial images for 45 nm line end structures ...9

Figure 1.5: Comparison of electron beam lithography techniques for single and multiple beam approaches 10

Figure 1.6: (a) Schematic of simple NIL process showing mold imprinting and RIE. The SEM images of the (b) mold and (c) resulting PMMA profiles before RIE 11

Figure 1.7: Defect classification results for the process of record by [64]. Out of 91 randomly selected defects for SEM review, zero was classified as a fundamental DSA polymer phase separation defect 13

Figure 1.8: Different IL setups utilized in literature (reproduced from [85]). 15

Figure 1.9: 6T SRAM. Left: GRD. Right: 2D design with 3 problematic locations 17

Figure 1.10: SEM images showing experimental hybrid optical maskless approach results in which IL and trim exposures were performed in the same resist 18

Figure 2.1: Monochromatic plane waves intersecting at the origin with half angle of θ. .22

Figure 2.2: (a) Definition of partial coherence. (b) Effect of partial coherence on imaging for an isolated 500 nm wide line. 25

Figure 2.3: (a) Measured time vibration data for an optical stepper. (b) Corresponding histograms based on 5-s and 60-s intervals. (c) Triangular vibration histogram approximation to (b) 28

Figure 2.4: (a) Sinusoidal vibration of a single frequency. (b) Its histogram 29

Figure 2.5: Schematic of reduction Talbot IL setup for important derivations. 31

Figure 2.6: Effect of optical path difference (OPD) on interference of correlated wave groups (modified from[108]). 35

Figure 2.7: Effect of OPD and source bandwidth (i.e. beating) on image contrast degradation across the field for 193 nm ArF laser. Three different source bandwidths are considered: broadband, 100 pm FWHM, and 2 pm FWHM. 36

Figure 2.8: LER framework proposed by [110]..39

Figure 2.9: ITRS LWR roadmap, shown with total LWR (3σ) and contribution of speckle for 5 different resists. Resist A is highlighted for discussion 40

Figure 2.10: SEM images depicting LER for varying resist thicknesses and for two resists with different sensitivities. Resist B has 2.5X more photo-acid generator concentration than resist A 41

Figure 2.11: LER degradation as a function of contrast loss shown for (a) UV6 chemically amplified resist, and (b) PMMA chain scissioning resist 42

Figure 2.12: LER comparison of 90 nm dense line/space pattern for an IL system (Amphibian) and ASML /1150i 43

Figure 2.13: The effect of LWR on (a) V_{th}, (b) I_{off} variability 44

Figure 2.14: The FinFET device performance variability as a function of roughness frequency for the same amplitude 45

Figure 2.15: (a) The mask roughness influence region [129]. (b) Mask roughness contribution as a function of resist quality and optical system cut off frequency .46

Figure 2.16: (a) Ideal mask diffraction information at the pupil plane. (b) Roughness diffraction order filtering by the optical system. (c) Simplified LTF definition. ..48

Figure 2.17: Schematic of two main sources of mask induced roughness for EUV: absorber roughness and replicated surface roughness 50

Figure 2.18: Effect of (a) special rinse, and (b) ion beam smoothing techniques on LER PSD … 52

Figure 2.19: Effect of increasing pulse duration with respect to the coherence time. Integrated dose (W) has less of a variation for longer pulses. $T << \tau_c$ corresponds to the conventional (static) pattern 53

Figure 2.20: Pupil filtering idea. Left: No filter case, right: with filter case 56

Figure 2.21: Enhancing resolution of EUV ADT tool by using a pupil plane amplitude filter at 22 nm half image pitch for resist A 57

Figure 2.22: Micrographs of stitched areas by optical and scanning electron microscope 58

Figure 2.23: (a) Parallel SBIL, (b) Doppler SBIL 59

Figure 2.24: Schematic of achromatic IL set up for 100 nm period image pattern 60

Figure 2.25: Examples of vendor specifications of a typical toolset used in 250 nm to 700 nm fabrication and VC curves from A to E 62

Figure 2.26: Comparison of pre- and post- startup vertical vibration for (a) narrow band data, (b) one third octave data 64

Figure 3.1: Contrast loss due to transverse shift error for uniform and sinusoidal type motions...66

Figure 3.2: (a) Mask with anti-correlated (L_1), random (L_2), and perfectly correlated (L_3) rough lines. (b) Aerial image from single pass exposure. (c) Aerial image from double pass exposure. Simulations performed with KLA-Tencor PROLITH™...67

Figure 3.3: (a) Interference lithography set up for the aerial image averaging experiments [18]. (b) Translation approach: the wedge is moved in x direction at mid exposure, resulting in shift of the image in y direction (along the lines). (c) Co-processed nominal and translated dies on the same wafer piece to minimize processing related variations. 68

Figure 3.4: Exposed module on the scanner and imaging conditions for each die 71

Figure 3.5: (a) 1D mask with smooth vertical line space features and corresponding diffraction information. (b) Mask with absorber roughness and corresponding diffraction information. Dashed regions: main diffraction orders coming from smooth vertical features 72

Figure 3.6: Collection of (a) many diffraction orders or (b) just the main diffraction orders at the pupil plane. Top down views of photoresist profiles generated with a constant threshold resist model are shown for each case 73

Figure 3.7: ASML's FexWave wavefront manipulator 74

Figure 3.8: (a) Programmed defect mask and the measurement locations along two cutlines. (b) Diffraction pattern of the mask with optimized dipole. (c) Effect of different aberrations on the aerial image profile and ΔCD along two cut locations.75

Figure 3.9: (a) Definition of an ideal (smooth) mask with vertical line space pattern, and corresponding (b) anti-correlated and (c) correlated programmed roughness masks ………..76

Figure 3.10: (a) Roughness transfer as a function of introduced defocus. (b) Optimized pupil plane phase filter for vertical line space patterns...77

Figure 3.11: (a) White noise mask. (b) Diffraction information at the pupil plane with optimized dipole illumination. Resulting aerial images for the (c) nominal case, (d) phase filtered case. 78

Figure 3.12: (a) Top-down aerial image intensity distribution for nominal anti-correlated and correlated masks. (b) Corresponding phase filtered distribution. (c) Comparison of intensity distributions along the cutlines......................................79

Figure 3.13: (a) Aerial image Bossung curves for nominal and phase filtered cases at two cutlines, (b) ΔCD between the two cutlines for nominal and phase filtered cases. "Nominal" refers to without the filter case. 80

Figure 3.14: Diffraction information for 200 nm and 500 nm roughness periods.............81

Figure 3.15: Optimization of phase filters for 200 nm (W1) and 500 nm (W2) roughness periods and corresponding Zernike combinations to create them. 82

Figure 3.16: (a) MATLAB surface fitting routine. (b) Effect of cost function inclusion on the fit efficiency. 83

Figure 3.17: (a) Target and experimental filters ($\Delta\Phi_{AB} \approx 0.25$ waves). (b) Zernike coefficients for the target and experimental filters. 85

Figure 3.18: Effect of pitch error in overlay of subsequent exposures.............................86

Figure 3.19: (a) Talbot set up with wedges for pitch fine tuning. (b) The definition of deviation angle from the wedge prism. (c) Deviation angle as a function of incident angle for the wedge prism with apex angle of 1.05°................................87

Figure 3.20: (a) Dies exposed over various θ, (b) Line-outs measured over 10 line/space pairs across the SEM field to calculate the pitch. 89

Figure 3.21: Comparison of theoretical OPD calculations with simulated results. 90

Figure 3.22: Maskless IL set up for studying OPD effect on contrast loss. 93

Figure 4.1: Initial problems associated with the interference lithography experiments: (a) ringing issue and (b) pattern collapse issue. (c) Spatial filtering. 95

Figure 4.2: (a) Co-processing of static (nominal) and image averaged (translated) dies. Comparison of nominal case LER to image averaged case LER with translation amounts of (a) 250 nm, (b) 500 nm, and (c) 750 nm. 96

Figure 4.3: Effect of contrast loss through flood exposure on LER PSD (a) for 139 nm thick resist, (b) for 75 nm thick resist 97

Figure 4.4: (a) Location dependency is observed for IL experiments. (b) Imperfect mask is one of the sources of variations. (c) Intra-field LER values 99

Figure 4.5: SEM pictures of 3 µm long patterns for the pitches of (a) 130 nm (Die 1), (b) 140 nm (Die 1), (c) 150 nm (Die 1), (d) 150 nm (Die 2), and (e) 150 nm (Die 8). 100

Figure 4.6: Effect of aerial image averaging on LER PSD for die 3 and die 8. Best case mitigation was for die 8 and highlighted with dashed box 102

Figure 4.7: Comparison of roughness transfer for nominal and filtered cases through focus for 200 nm and 500 nm roughness periods. 103

Figure 4.8: Nominal and phase filtered SEM images for 200 nm roughness period in (a) anti-correlated and (b) correlated fashions. 104

Figure 4.9: Nominal and phase filtered SEM images for 500 nm roughness period in (a) anti-correlated and (b) correlated fashions. 105

Figure 4.10: Through slit LWR values for the nominal and wavefront cases programmed with periods of (a) 200 nm and (b) 500 nm, in both correlation types. Error bars correspond to average 1σ LWR variations. 106

Figure 4.11: Through slit LER values for the nominal and phase filtered cases programmed with periods of (a) 200 nm and (b) 500 nm, in both correlation types. Error bars correspond to average 1σ LER variations...107

Figure 4.12: Through slit LF LER values for the nominal and wavefront cases programmed with periods of (a) 200 nm and (b) 500 nm, in both correlation types. Error bars correspond to average 1σ LER variations...108

Figure 4.13: Slit center LER values for (a) 200 nm, and (b) 500 nm roughness periods at the slit center. Both correlation types are considered 109

Figure 4.14: LER PSD of nominal and phase filtered wafers. Comparison for 200 nm roughness period with amplitudes of (a) 1nm/edge and (b) 5nm/edge. Comparison for 500 nm roughness period with amplitudes of (c) 1 nm/edge and (d) 5 nm/edge.110

Figure 4.15: Experimentally calculated correlation factor for (a) 200 nm, (b) 500 nm roughness periods...112

Figure 4.16: Effect of filtering on (a) smooth line 3σ LWR through bias. (b) NILS reduction and LWR increase through roughness amplitude for the filtered case.113

Figure 4.17: Pitch fine tuning via change in rotational angle of the wedge prism holder. Dashed line corresponds to a trend line fit to the experimental data points. 115

Figure 4.18: Effect of OPD on image quality as a function of DC.................................116

LIST OF TABLES

Table 1.1: Comparison of Excimer and Solid State Lasers (modified from [92])...........16

Table 2.1: Summary of vibration tolerance at k_1=0.64 and σ=0.8 30

Table 2.2: 2011 Edition ITRS LWR requirements (generated from data of [32]) 37

Table 2.3: Acceleration measurement methods and properties 61

Table 2.4: Application and interpretation of the generic VCC as shown in Fig. 2.25.......63

Table 3.1: IPE tolerances for DRAM nodes (adapted from 2007 edition of ITRS [159]) 91

Table 4.1: LER (3σ) values for all frequencies and low frequencies (S: static, P: pass). The amount of shift between passes is given in Fig. 3.4. The inter-field LER variation is less than 0.1 nm (1σ)...101

LIST OF ACRONYMS

ACP	Air cushion press
ADT	Alpha demo tool
BARC	Bottom anti-reflective coating
CD	Critical dimension, [nm]
CF	Correlation factor
CoO	Cost of ownership
DE	Double exposure
DIW	Deionized water
DOF	Depth of focus
DP	Double patterning
DSA	Directed self-assembly
DUV	Deep ultraviolet region of the radiation (100–300 nm wavelength)
EBL	E-beam lithography
EL	Exposure latitude
EUV	Extreme ultraviolet region of the radiation (10–30 nm wavelength)
EUVL	Extreme ultraviolet lithography
FEM	Focus-exposure matrix
FIB	Focused-ion-beam
FWHM	Full width half maximum
GRD	Gridded regular design
HIF	High index fluid
HVM	High volume manufacturing
IC	Integrated circuit
IL	Interference lithography
IPE	Image placement error

ITRS	International Technology Roadmap for Semiconductors
LELE	Litho-etch-litho-etch
LER	Line edge roughness
LFLE	Litho-freeze-litho-etch
LPLE	Litho-process-litho-etch
LTF	Line edge roughness transfer function
LWR	Line width roughness
MAPPER	Multi aperture pixel by pixel enhancement of resolution
MEEF	Mask error enhancement factor
ML2	Maskless lithography
MTF	Modulation transfer function
NA	Numerical aperture
NGL	Next generation lithography
NIL	Nanoimprint lithography
NILS	Normalized image log slope
OPC	Optical proximity correction
OPD	Optical path difference
OPL	Optical path length
OTF	Optical transfer function
PAG	Photo-acid generator
PML2	Projection maskless lithography
POR	Process of record
PS	Pitch splitting
PSM	Phase shifting mask
REBL	Reflection electron beam lithography
RET	Resolution enhancement techniques

RMS	Root-mean-square
RSR	Replicated surface roughness
SBIL	Scanning beam interference lithography
SEM	Scanning electron microscope
SFIL	Step-and-flash imprint lithography
SMO	Source mask optimization
SP	Spacer patterning
SR	Surfactinated rinse
UV	Ultraviolet region of the radiation (150–400 nm wavelength)
VCC	Vibration criteria curves
WPH	Wafer per hour

1. INTRODUCTION TO LITHOGRAPHY

Since the invention of the transistor more than 60 years ago, semiconductor industry has witnessed significant progress in device manufacturing. The developments resulted in more powerful and sophisticated products that are also cost effective. Some of these recent developments can be listed as realization of strained silicon, low-k insulators and high-k gate metal. More recently, Intel announced their 22 nm technology node which uses a tri-gate transistor to boost the gate control over the short channel, instead of the conventional planar transistors [1, 2].

In integrated circuit (IC) manufacturing process, the photolithography step is repeated several times; hence, it accounts for about 30% of the cost of manufacturing [3]. In addition, it is also the photolithography step that limits the critical dimension of the printed features; hence, the speed of transistors. The reduction in device scales has resulted in the trend of doubling of number of transistors on a chip approximately every two years, which is widely known as Moore's law [2]-[4].

Figure 1.1 shows a simple projection lithography system set up composed of a deep-UV (DUV) source, a condenser lens, mask, and an objective lens located at the pupil plane with a size defined by the numerical aperture (NA) of the system. The projection system creates an aerial image that is approximate to the patterns defined in the mask, but at a fixed reduction ratio (usually reduction factor of 4). The aerial image subsequently exposes a photo-reactive medium called "photoresist." Depending on the chemical makeup of the material and the developer utilized, the process can result in

either positive tone or negative tone imaging, where the former requires removal of the photoresist materials that corresponds to the transparent parts on the mask [3, 5].

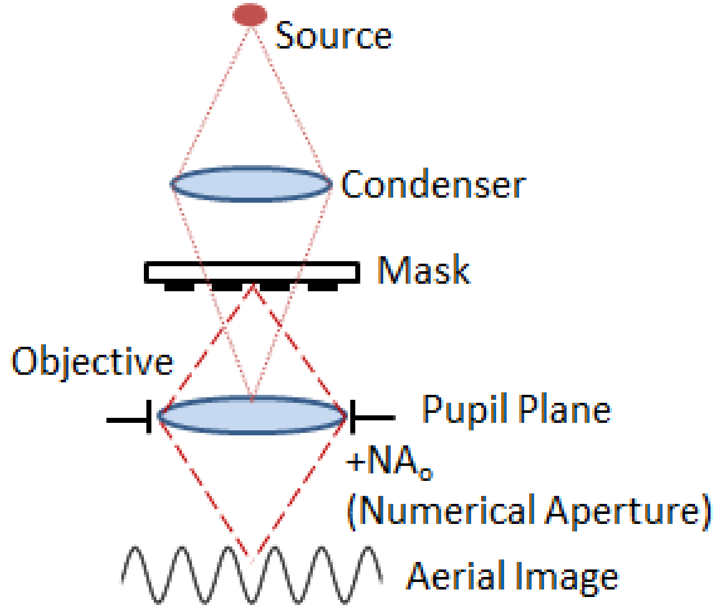

Figure 1.1: A simplified schematic of a projection lens system.

1.1 **Background of Lithography**

The main goal of semiconductor manufacturing has been to produce smaller, faster and more sophisticated devices, which is achievable by reducing the feature sizes through lithography processes. For periodic features, the minimum resolution of an imaging system is characterized by the "Rayleigh's criterion", which is given as

$$R = \frac{k_1 \lambda}{n sin(\theta)} = \frac{k_1 \lambda}{NA} \tag{1.1}$$

where critical dimension, exposure wavelength, refractive index of imaging medium, half angle subtended by the objective lens, and numerical aperture of the system are denoted by R, λ, n, θ, and NA, respectively [6]. The process dependent factor is shown as k_1,

which can be pushed close to its theoretical limit of 0.25 by utilizing resolution enhancement techniques (RET) [7, 8]. Some of the resolution enhancement techniques that have been pursued for further improvements can be listed as optical proximity correction (OPC) [9, 10], phase shifting mask (PSM) [11], off axis illumination [12, 13], and source mask optimization (SMO) [14, 15].

Another criterion that is important in characterizing the performance of the lithography system is called the "Depth of Focus" (DOF), given as [3]

$$DOF = \pm \frac{k_2 n \lambda}{NA} \tag{1.2}$$

where k_2 is another process dependent factor. Rayleigh's criterion shows that in order to reduce the critical dimension, one can shift from longer wavelength to shorter wavelengths, increase the numerical aperture of the objective lens or improve the lithographic process. Over the past decades, the illumination wavelength has been reduced from mercury lines (436 nm *g*-line and 365 nm *i*-line) down to deep-ultraviolet (DUV) wavelengths of KrF (248 nm), ArF (193 nm), and F_2 (157 nm). The wavelength reduction trend is concluded at immersion 1.35 NA ArF. As a next step, major tool providers are investing extensively on infrastructures of 13.5 nm wavelength extreme UV (EUV) lithography [16].

Immersion ArF lithography (sometimes combined with pitch splitting approach) is the workhorse of current production lines. Currently, down to 40 nm features can be resolved with state-of-the-art water immersion projection lithography employing 193 nm ArF excimer laser source with 1.35 NA catadioptric projection optics [17]. When combined with pitch splitting, resolution can be pushed even below that [16, 17].

Aside from reducing the minimum device dimensions, the tolerances on the fidelity of the lithography defined patterns are becoming much more stringent. The impact of sidewall roughness on photoresist lines, usually referred to as the line edge (or width) roughness has been shown to impact the electrical performance of the semiconductor devices significantly. If it is not addressed, it might limit the useful resolution [3]. The ideas presented in this work, such as aerial image averaging via directional translation [18] and pupil plane filtering [19], might help reduce the roughness seen in interference-like lithography conditions.

1.2 Excimer Laser Review

The source is one of the most crucial parts of illumination systems in optical lithography. It determines the coherency of imaging, quality of patterns, and throughput of the whole system. Therefore, it is important to understand important properties of the illuminating source.

Excimer laser lithography systems are superior to e-beam writers in terms of throughput. Since 1988, through the trials for 64 Mbit DRAM, excimer lasers have become the main choice in commercial high volume manufacturing (HVM) [20].

There are certain differences between a mercury lamp and excimer lasers, which are related to the characteristics of the short wavelength excimer lasers and high power pulse energy with short pulse durations (i.e., pulsed lasing). Sometimes, such large power peaks might change material properties or even damage might occur. Other important

differences between the excimer laser and mercury sources can be listed as the small divergence values and pulse to pulse energy fluctuations [20].

The natural linewidth (full width half maximum-FWHM) of excimer lasers is usually between 0.3 nm and 1 nm. Such bandwidth values at nm levels are too large for chromatic aberrations in a lens system and needs to be reduced below 3 pm by utilizing line narrowing modules, such as etalons, dispersive prisms, gratings or their combinations in the cavity of the laser [20, 21].

Line narrowing through two etalons with different gap thicknesses in the cavity of the laser provides high efficiency and sufficiently narrow bandwidths. Using prisms, instead, provides high thermal stability and high damage threshold, at the cost of low dispersion efficiency. Therefore, it is quite common to use combination of prisms and gratings as dispersive elements in current lasers. Using such techniques, spectral bandwidth of the laser can be as low as 1.0 to 1.5 pm [21-28].

Wavelength stability is crucial for the performance of imaging since even a 1 pm drift in central wavelength might lead to more than 0.1 µm shift in focal plane for a typical chromatic lens [29]. Therefore, wavelength is monitored continuously by techniques such as observing the fringe formation by a monitoring etalon [22, 23, 25, 28], or measuring the wavelength difference of the absorption line of a gas cell [20, 26].

Narrowing the linewidth increases the temporal coherence of the beam. It also increases the spatial coherence due to the reduced divergence angle. However, increased coherence might result in unwanted interference effects and speckle patterns, which are detrimental to the illumination uniformity of the beam [20, 30].

The excimer lasers are pulsed and the output energy of varies from pulse to pulse [20, 31]. This fluctuation is problematic when a fixed number of pulses were accumulated to reach the required dose at the wafer plane. In order to guarantee a certain amount of dose accuracy (A), one can define the minimum number of pulses to be accumulated (N) as follows [20]

$$N \geq \left[\frac{\Delta P/P}{A}\right]^2 \tag{1.3}$$

where ΔP/P defines the pulse to pulse energy stability. For a scenario requiring 0.5% dose accuracy and 5% fluctuation from pulse to pulse, more than 100 pulses are required [20].

1.3 **Next Generation Lithography (NGL) Approaches**

Fig. 1.2 shows the 2011 edition of ITRS [32], summarizing applicable technologies for next technology nodes starting from 2011 up to 2026. For the 32 nm node, ArF lithography is sufficient enough by utilizing pitch splitting techniques. However, for more advanced nodes, the process complexity and the demands increase.

For instance, Intel recently revealed its 22 nm node 3D transistors to enable improved control of the channel below the gate region. The gate surrounds the silicon channel in three directions, which provides significant energy efficiency [1]. For sub-22 nm DRAM technologies, introduction of non-optical lithography approaches is seen as a necessity to sustain Moore's law and satisfy industry demands [32].

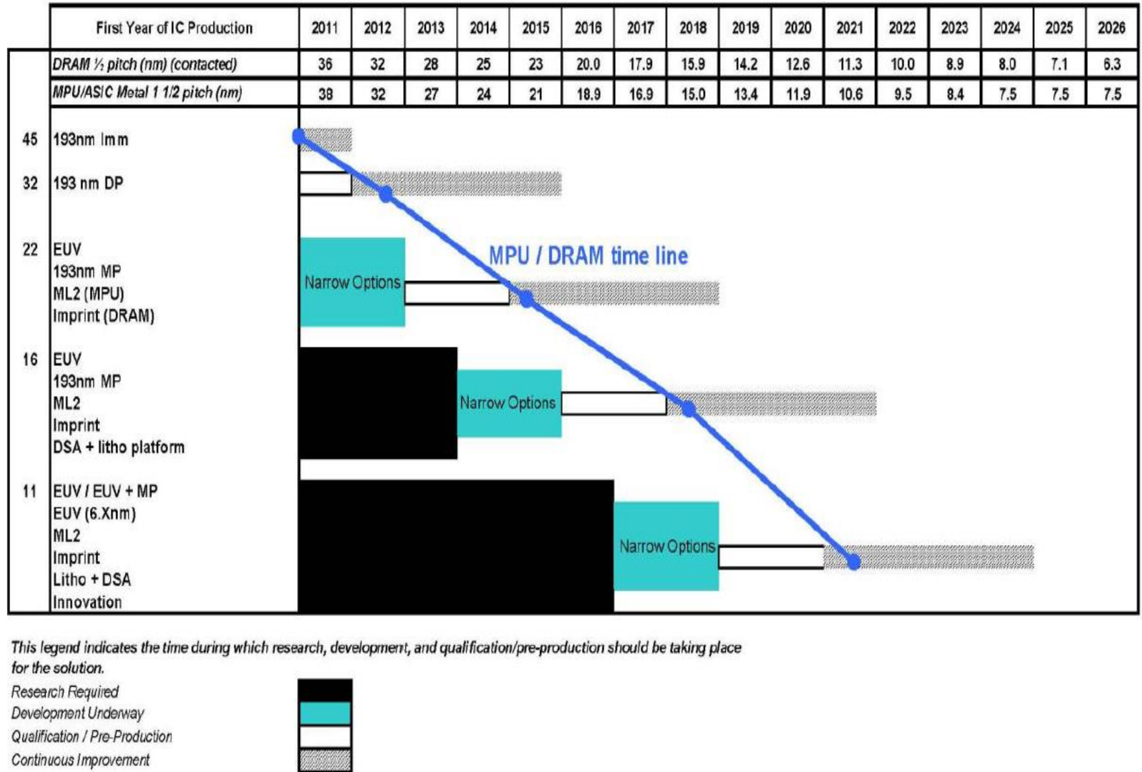

Figure 1.2: Lithography exposure tool potential solutions for MPU and DRAM [32].

1.3.1 *Double patterning (DP) technology*

In order to push k_1 beyond its theoretical limit of 0.25 and achieve smaller devices, two basic processes known as “Pitch Splitting (PS)” and “Spacer Patterning (SP)” can be utilized [33-36]. PS is achievable via Litho-Etch-Litho-Etch (LELE) or Litho-Freeze-Litho-Etch (LFLE) processes [37]. The latter is also known as Litho-Process-Litho-Etch (LPLE). The spacer patterning approach multiplies the pitch by sidewall spacer formation to the sides of the mandrel layer [34, 38]. Though, it has one critical lithography step, it requires a critical deposition and etch step very similar to spacer-like processes. Subsequent cut (trim) mask lithography is needed to remove excess parts of the layer. In a Litho-Etch-Litho-Etch method a sacrificial hard mask is used to transfer the image from each litho-etch step; however, the cost of ownership (CoO) of

this method is proportional to the complexity of processing it [39]. Fig. 1.3 shows the basic process flows for the pitch splitting and spacer multi-patterning approaches [32-34, 36, 38].

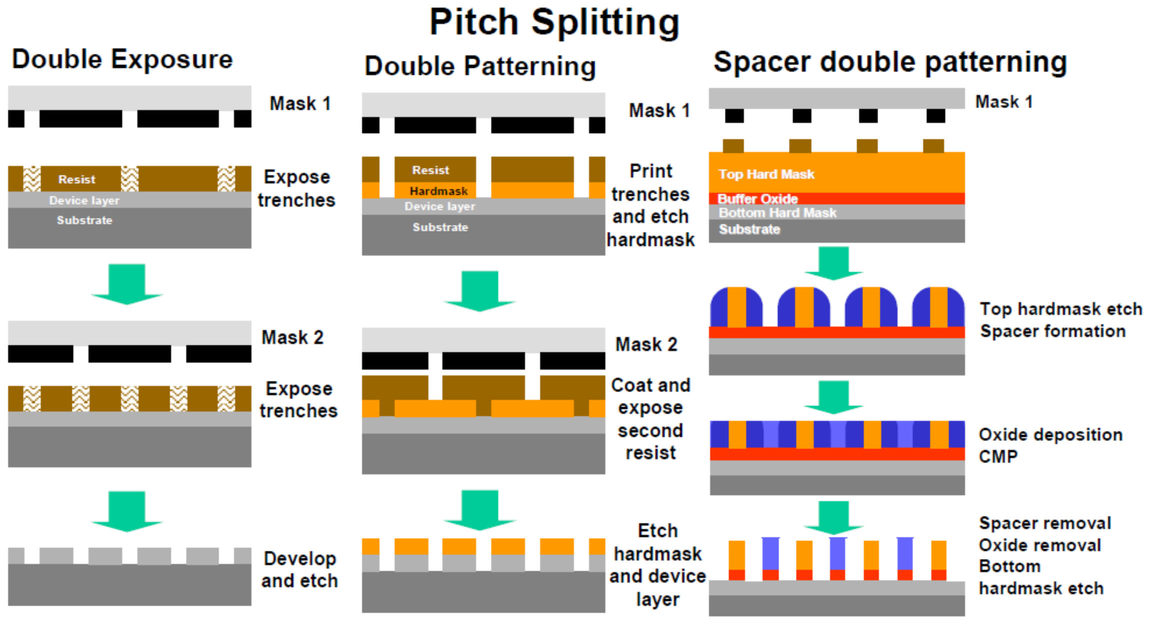

Figure 1.3: Process flows for DE, DP, and SP approaches [32].

1.3.2 *EUV lithography technology*

Improvement of low k1 values is troublesome and hard to achieve. From Rayleigh's criteria, the next logical option to improve minimum resolution is the wavelength reduction. Therefore, EUV is currently viewed as a strong candidate as far as the NGL options are concerned [40]. However, there exist many problems in terms of masks, material properties, and available source power [41-43].

The wavelength of EUV is fourteen times smaller than the deep-UV (DUV) wavelengths. By utilizing 0.25 NA EUV and a modest k_1 value of 0.6, a 32 nm half pitch pattern is easily achieved [16].

Fig. 1.4 shows the benefit of using EUV instead of DUV in terms of image fidelity, by comparing 45 nm line-end structure aerial images. With a 1.30 NA ArF immersion tool, the image is not well defined. However, due to EUV's inherent capacity to print smaller features, image fidelity is high even with a small NA value of 0.25 [40]. The main obstacle for EUV to be ever used in HVM is the dim source power resulting in less than the desired throughput levels in a HVM environment.

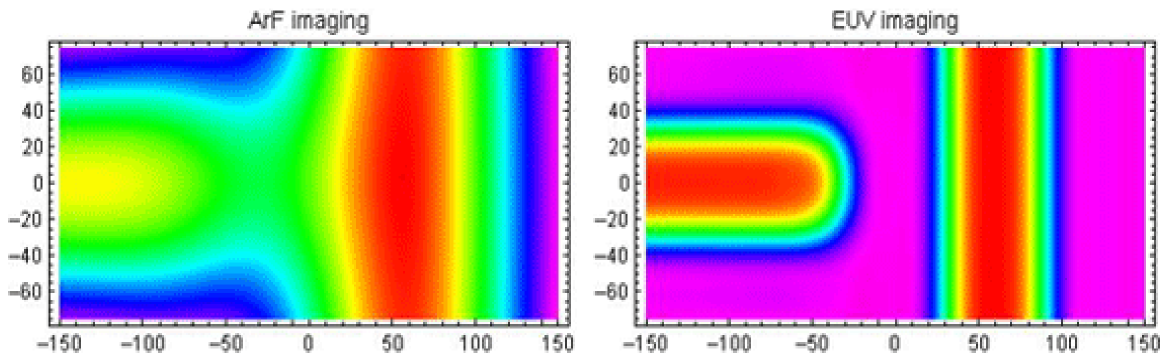

Figure 1.4: Comparison of DUV and EUV aerial images for 45 nm line end structures [40].

1.3.3 *Maskless lithography technology*

Maskless lithography (ML2) is another option proposed for sub 22 nm nodes and most of the time refers to patterning photoresists without optical illumination, such as zone-plate-array lithography [44], and focused-ion-beam (FIB) lithography [45, 46].

E-beam lithography [47, 48] is the most common maskless method, where a focused electron beam is scanned on a photoresist material to create high resolution patterns with good accuracy. Single beam writing systems have extremely slow writing times; therefore, multiple-beam writing approaches have been implemented to overcome the low throughput issues [49].

Some of such maskless lithography systems where multitude of beams are coordinated with respect to their size, dose and placement can be listed as Multiple Aperture Pixel by Pixel Enhancement of Resolution (MAPPER) [50, 51], Projection Maskless Lithography (PML2) [52], and Reflective Electron Beam Lithography (REBL) [53] (shown in Fig. 1.5). However, these direct write technologies still provide far less throughput than what is required by any HVM technology [16].

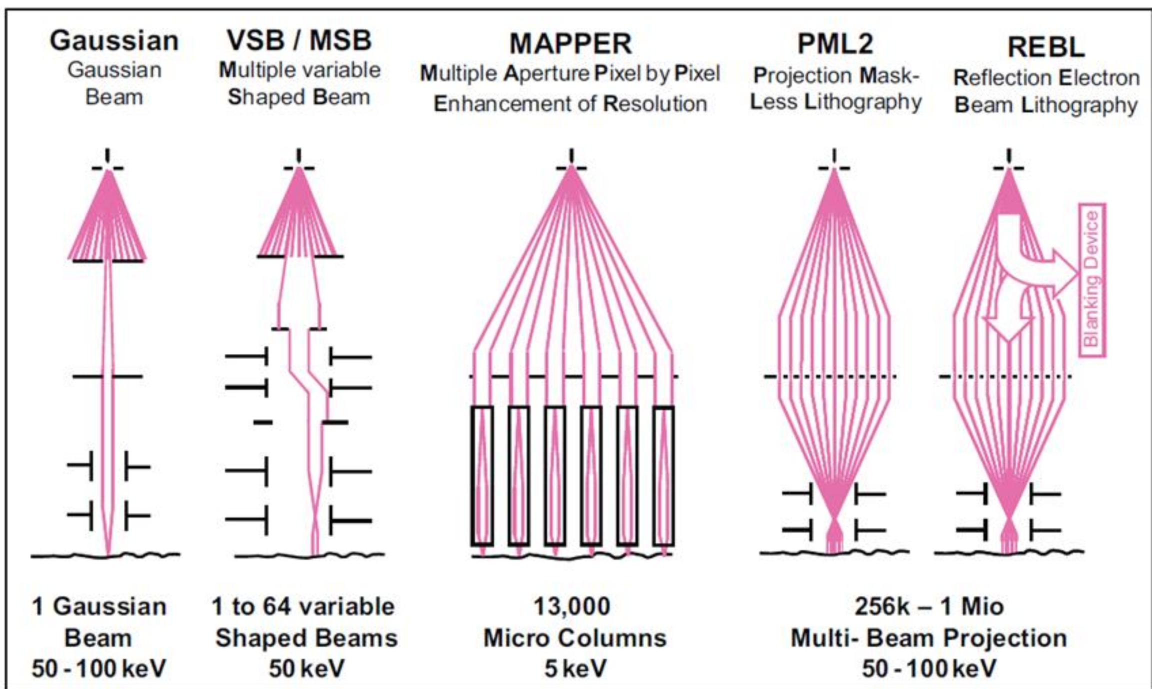

Figure 1.5: Comparison of electron beam lithography techniques for single and multiple beam approaches [49].

1.3.4 *Nanoimprint lithography technology*

Nanoimprint lithography (NIL) is another NGL method gaining more popularity due to its simplicity, high throughput, and high resolution capability without the need for a complex projection lithography set up. It is listed as one of the potential solutions for

22 nm, 16 nm and 11 nm technology nodes in ITRS reports. The basic flow of NIL is shown in Fig. 1.6 (a) which consists of mold press, mold removal and anisotropic etch to remove the residual resist material [54]. The mold imprint step requires baking the resist (e.g., poly-methyl-methacrylate-PMMA) above the glass transition temperature where it becomes thermoplastic and viscous enough to flow. Fig. 1.6 (b) and (c) show the SEM images of a sample mold/template and corresponding PMMA profile (70 nm wide) before the etch step. The durability of the mold and repeatability are seen as key challenges to extend NIL to HVM [54].

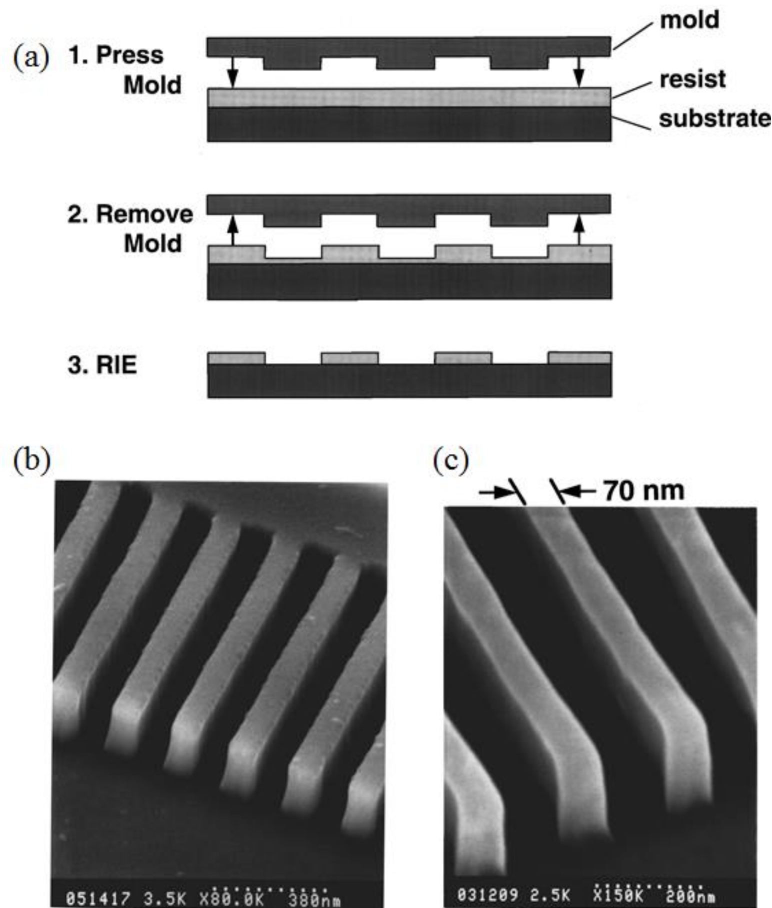

Figure 1.6: (a) Schematic of simple NIL process showing mold imprinting and RIE. The SEM images of the (b) mold and (c) resulting PMMA profiles before RIE [54].

A modified version of this basic process is called step-and-flash imprint lithography (SFIL), where a photo-polymerizable solution between the mold and the substrate is cured with UV light coming through the backside of the transparent template. Sub-60 nm features have been shown with SFIL approach [55].

Since the pattern resolution is defined by the template, this is a 1X process. The concerns for NIL is common to any contact printing process and can be listed as overlay, alignment, defect control and repair, throughput, and template lifetime [16]. In order to ensure the pressure and pattern uniformities of full wafer nanoimprint processes and prolong the mold lifetime, a pressing method utilizing isotropic fluid pressure, named Air Cushion Press (ACP) has been developed and utilized by commercial nanoimprint systems [56]. NIL is utilized in a variety of niche markets such as medicine, environmental sciences, LED, hard disk, and photonics.

1.3.5 *Directed self-assembly technology*

Directed Self Assembly (DSA) is a fairly recent addition to the NGL approaches and offers great benefits in terms of resolution and ease of implementation [16, 57]. It is also utilized in contact hole shrink applications [58, 59]. This method relies on the thermodynamic micro-phase segregation of two immiscible polymers (usually polystyrene and poly methyl methacrylate) mixed in a solution. Each polymer forms micro-blocks that will give equilibrium of minimum interfacial energy. Nanophases such as spheres, cylinders, gyroids and lamellae are results of the segregation [57, 60].

The high resolution self-assembly pattern can be directed to achieve long range order by guidance of a topographic (Grapho-epitaxy) or chemical pre-patterning [61-63]. The research on self-assembly took significant momentum after showing 193 nm compliance [16].

A process of record (POR) for 300 mm baseline process was shown using 12 nm half-pitch PS-b-PMMA lamellae block copolymer in [64]. In that paper, a successful defect density test vehicle was discussed with high sensitivity to detect DSA specific defects, e.g., “dislocations” and “disclination,” resulting from imperfect phase-separation or lack of enough thermodynamic force to drive the perfect epitaxial registration of the lamellae between the pre-patterned structures. The authors observed zero dislocation and disclination defects for < $26/cm^2$ upper limit, with a very wide process window related to the immersion pre-pattern [64]. The defect test results of their work are given in Fig. 1.7.

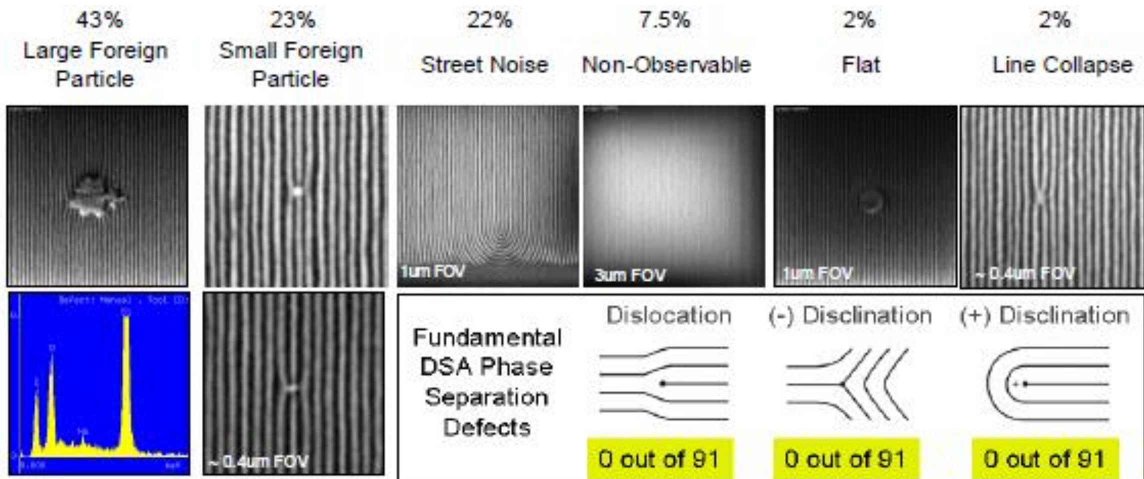

Figure 1.7: Defect classification results for the process of record by [64]. Out of 91 randomly selected defects for SEM review, zero was classified as a fundamental DSA polymer phase separation defect [64].

1.3.6 *Interference lithography*

Interference lithography (IL) generates regular 1D line/space patterns by combining two or more coherent beams of illumination without the need for expensive projection lithography lens systems [65-70]. Contacts/holes can also be generated by utilizing four-beam interference approach [71-73]. Due to its simplicity and ease of manipulation, IL has been used extensively to test photoresist materials [74-77] and in production of many components such as nanowires [78, 79], polarizers [80], and photonic crystals [81, 82].

Compared to conventional projection lithography, it offers significant benefits such as imaging at the ultimate resolution limit with very high contrast and large DOF depending on the state of the polarization. The process dependent parameter k_1 is assumed to be fixed at 0.25 [16].

IL has been a cost effective solution for EUV experiments, since alpha demo tools are very expensive [83, 84]. Throughout the years, many types of IL configurations have been used at universities and research centers, either splitting the wavefront or the amplitude. Fig. 1.8 shows a few common IL setups [85].

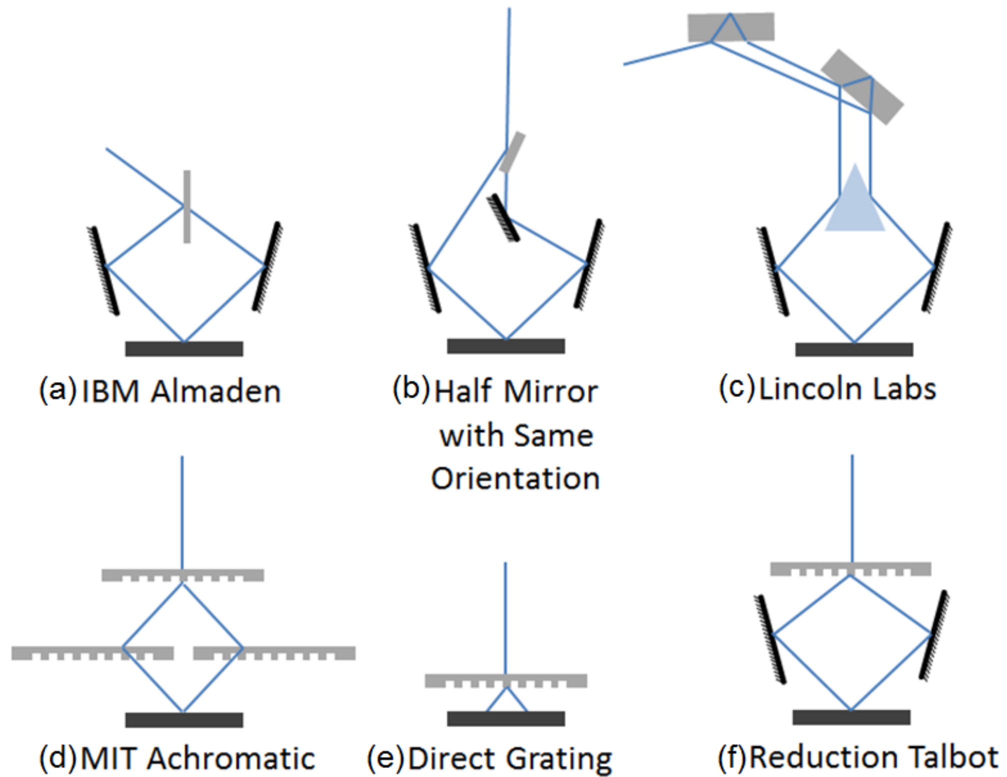

Figure 1.8: Different IL setups utilized in literature (reproduced from [85]).

Fig. 1.8(a) shows an amplitude dividing interferometer [86] with a partially transmitting mirror, serving as a beam splitter. Since different parts of the beam are recombined at image plane, this set up calls for very high spatial coherence. This problem can be overcome by including another mirror to flip one of the beams as suggested in Fig. 1.8(b); however, now the system will suffer from alignment difficulty and optical path length (OPL) difference between the combining beams, thereby degrading the temporal coherence. Fig. 1.8(c) depicts Fresnel reflection/refraction based beam splitter, which suffers from difficulty of precisely aligning many optical elements [87]. Achromatic approaches [88], such as Fig. 1.8(d), do not require a line narrowed source; but, the image pattern pitch is fixed at half of the grating pitch and the gap control between the grating stack needs to be very accurate. The direct interferometer shown in

Fig. 1.8(e) also suffers from the fixed pitch problem [89, 90]. In addition, extending these achromatic approaches to immersion lithography is troublesome. The reduction Talbot approach (Fig. 1.8 (f)) has the ability to change the spatial frequency of the image pattern by use of mirror tilting, and as long as the wafer plane is placed at an optimum location, the poor spatial coherency will not be a problem. Extending this approach for liquid and solid immersion has already been shown [16, 65, 69, 85].

IL can print patterns with half pitches down to 37 nm at 1.35 NA with 193 nm TE polarized light. Adopting double patterning would bring this limit down to 19 nm. Utilizing sapphire and high index fluid (HIF) with refractive indices greater than 1.65 enables imaging at 1.6 NA that yields 30 nm half pitch (15 nm ¼ pitch). Further increase in NA could be achieved via evanescent wave coupling [16, 91].

It should be pointed out that not all types of lasers will work for any kind of IL configuration; however, by choosing the right set up, one can alleviate the requirements for source coherency. For instance, Talbot set up is very suitable for excimer laser, as shown in Table 1.1.

Table 1.1: Comparison of Excimer and Solid State Lasers (modified from [92]).

	Excimer (193 nm)	**Solid State (Actinix)**
Power	High power (90 W)	0.25 W (can scale to 1 W)
Spatial Coherence	Medium (~2 mm)	High
Temporal Coherence	0.35 pm or better	<0.13 pm
Rep. Rate	6 kHz	1-4 MHz
Configuration/Issues	Talbot suitable (preservation of coherence). Difficult for Michelson type approaches.	Suitable for most configurations, coherence artifacts.

In the context of this work, interference-like lithography refers to imaging conditions of periodic line space patterns with commercial scanners and coherent light sources. When interference-like conditions are utilized, some unconventional approaches can be pursued in order to mitigate LER.

1.4 One Dimensional Regular Design Approaches

Recently, conversion of 2D random designs into 1D gridded regular layouts, through "Gridded Regular Design" approaches, gained significant attention. The goal is to eliminate the hassle of 2D proximity effects by benefiting ease of 1D regular patterning [38]. This is especially desirable for complex logic devices where there are many decomposition conflicts, compared to memory chips [16, 93]. With "Gridded Regular Design (GRD)" approaches, complex layout designs become very regular. As an example, comparison of 2D random design and 1D regular design for six transistor (6T) SRAM poly layer is shown in Fig. 1.9. Three problematic locations on 2D design are pointed out with numbers [94].

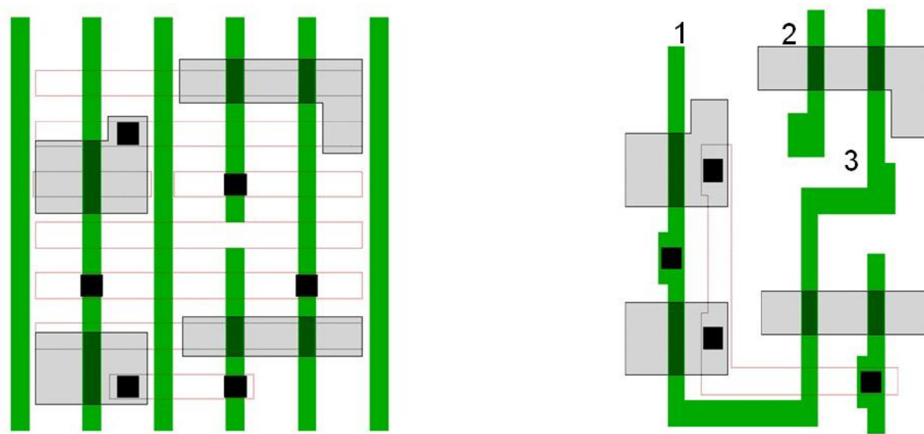

Figure 1.9: 6T SRAM. Left: GRD. Right: 2D design with 3 problematic locations [94].

Conversion of 2D structures to 1D regular design allows use of some not-so-common methods such as DSA and IL to generate the high resolution grid patterns instead of the expensive conventional methods. The combination of IL lithography with trimming exposures allows a simple and cheap way of generating regular sub 32 nm patterns as shown experimentally in Fig. 1.10 [95, 96].

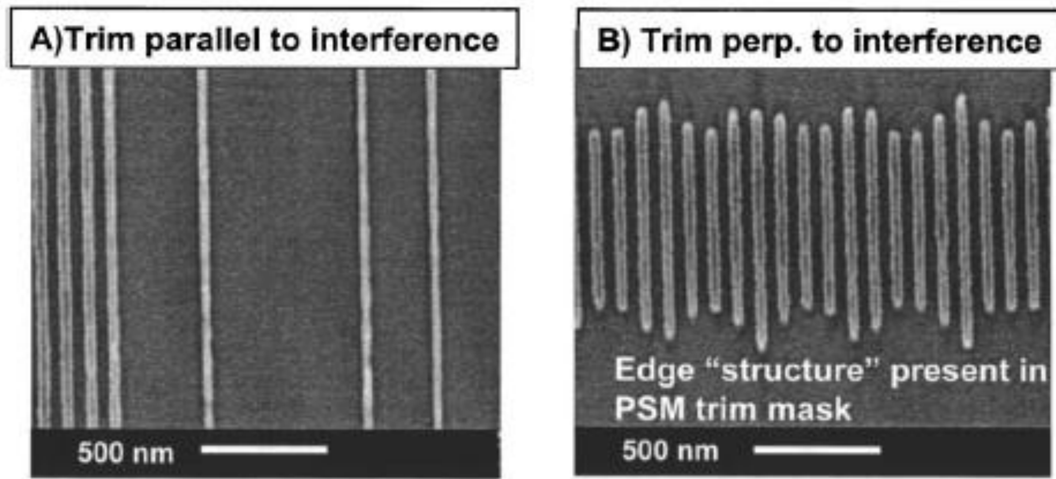

Figure 1.10: SEM images showing experimental hybrid optical maskless approach results in which IL and trim exposures were performed in the same resist [96].

1.5 Problem Statement

Line edge roughness (LER) present on the photoresist patterns is seen as one of the most important challenges for advanced technology nodes. There are many contributors to LER that can come from the aerial image or resist processing. While stochastic resist kinetics and processing remain the dominant roughness contributors, the roughness originating from the mask is gaining more attention, since its contribution in the low frequency (LF) range is particularly detrimental to the electrical device performance by causing variations in electrical device characteristics [19, 97].

In order to depict the importance of LF roughness, Fig. 1.11 shows a single line that serves as a gate to multiple transistors. The low frequency roughness present on the line will results in different gate lengths for each transistor. While the roughness with periodicities larger than the gate width can cause gate threshold voltage variations on the same chip, roughness with periodicities smaller than the gate length will affect the leakage currents [98]. Both are undesirable attributes that should be minimized.

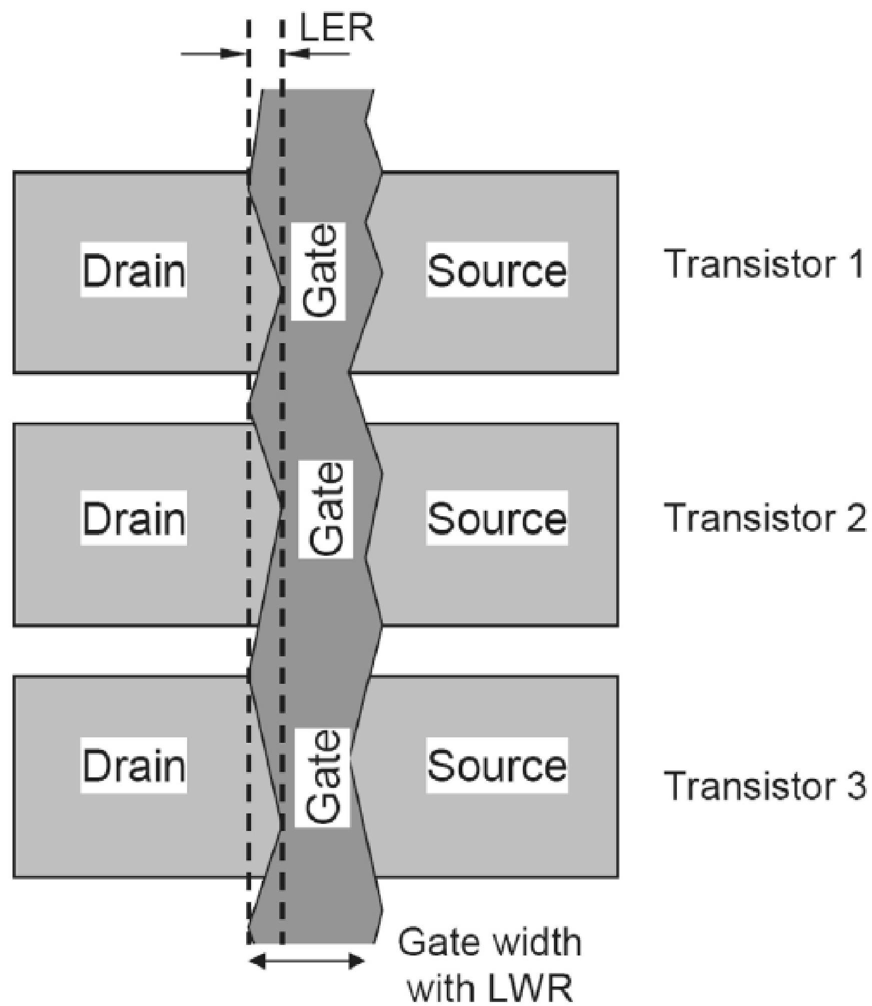

Figure 1.11: Effect of LWR and LER on gate width variations [98].

The leakage current is shown to increase exponentially with increased roughness. For the 65 nm technology node, it has been found that a 3σ LWR value of less than 10% gate CD results in up to 2% degradation in device performance [99]. The ITRS restricts the LF LWR to be less than 8% of the corresponding technology's CD [32].

Since IL set ups such as reduction Talbot design provides much higher theoretical contrast compared to conventional lithography techniques, and considering the current interest in converting 2D random designs into 1D regular layouts, it would be beneficial to scale cost effective IL for large field IC applications and thereby reduce LER. However, some challenges need to be addressed in order to accomplish this task.

In addition, because the mask roughness is one of the contributors to low frequency wafer LER [97], it would be utmost valuable to find new approaches to mitigate the mask roughness transfer in projection lithography systems, under interference-like lithography conditions. These are the goals of the research conducted herein.

2. THEORY AND BACKGROUND

2.1 Coherent Image Formation

Interference-like imaging produces periodic patterns by combining two or more coherent laser beams. In projection lithography, aberration free lens system captures maximum range of diffraction orders. However, in case of interference lithography, usually only two diffraction orders are combined, which eliminates the need for expensive projection optics. In case of reduction Talbot IL set up, the NA of the imaging system can easily be adjusted by use of a varying angle mirror system [16].

References [100, 101] give rigorous vector based calculations of two-and three-beam interference imaging. In this work, two-beam imaging was performed for the IL experiments; therefore, relevant results are included for completeness.

Fig. 2.1 shows interference of two monochromatic plane waves with the same polarization state. The intersection line is set as the x axis with origin at the center of the beams. The half angle of the interference is depicted as θ. If the light is TE polarized, electric fields are parallel to each other; therefore, vector summation of the fields actually becomes a scalar summation.

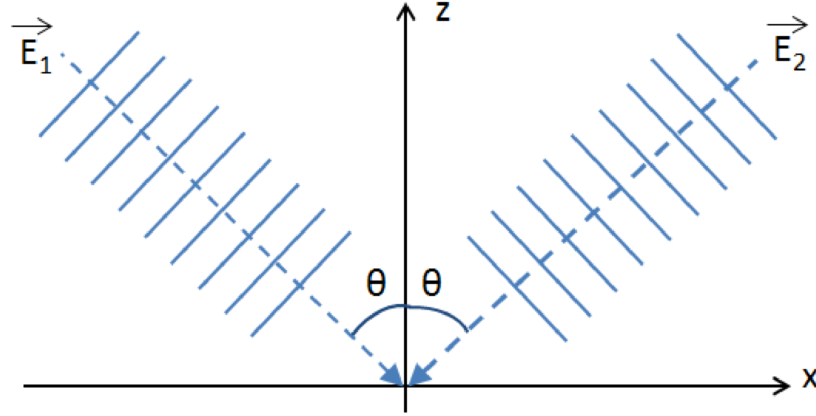

Figure 2.1: Monochromatic plane waves intersecting at the origin with half angle of θ.

Neglecting time dependence, the two electric fields (left beam $\mathbf{E_1}$, right beam $\mathbf{E_2}$) interfering at the origin can be shown as [101]

$$E_1 = |E_1|e^{-i(kxsin(\theta))} \tag{2.1}$$

$$E_2 = |E_2|e^{-i(-kxsin(\theta))} \tag{2.2}$$

where k is the propagation vector, given as 2nπ/λ. The summation of these two fields at the intersection can be calculated as [101]

$$E = E_1 + E_2 = |E_1|e^{-i(kxsin(\theta))} + |E_2|e^{-i(-kxsin(\theta))}$$

$$= [|E_1| + |E_2|]\cos\big(kxsin(\theta)\big) + i[|E_1| - |E_2|]\sin\big(kxsin(\theta)\big) \tag{2.3}$$

The resulting intensity (I) is calculated from the square of the total electric field amplitude as [101]

$$I \propto |E|^2 = |E_1 + E_2|^2 = |E_1|^2 + |E_2|^2 + 2|E_1||E_2|\cos(2kxsin(\theta)) \tag{2.4}$$

The intensity distribution along *x* direction is a sinusoidal pattern with a spatial period (p) given as [101]

$$p = \frac{\pi}{ksin(\theta)} = \frac{\lambda}{2nsin(\theta)} \tag{2.5}$$

For $|E_1| = |E_2|$, the intensity distribution is simplified to [101]

$$I_{2-Beams,TE} \propto 2|E_1|^2[1 + \cos(2kxsin(\theta)] = 4|E_1|^2 cos^2(kxsin(\theta)) \tag{2.6}$$

If the light is TM polarized, the total intensity needs to be calculated by vector summation,

$$I_{2-Beams,TM} \propto 2|E_1|^2[1 + \cos(2kxsin(\theta)cos(2\theta)] \tag{2.7}$$

Comparing equations (2.6) and (2.7), it is seen that the intensity modulation for TM case is dependent on the interfering angle between the two beams [101].

The image achieved from interference of two beams with intensity of I_0 can also be written in terms of the fringe period and contrast as [102]

$$I_x = 2I_0\left[1 + Ccos\left(\frac{2\pi x}{p}\right)\right] \tag{2.8}$$

where the contrast (C) is

$$C = \frac{I_{max} - I_{min}}{I_{max} + I_{min}} \tag{2.9}$$

I_{max} and I_{min} are the maximum and minimum intensity values [102]. The contrast metric is defined for only equal line and spaces and it is a useful metric only for patterns near the resolution limit. Another drawback of using contrast as an image quality metric is that it samples the aerial image at the wrong location. The edge of the aerial image is where the transition between the low and high intensity takes place and thereby is the most

important location [3]. Therefore, just like in any conventional lithography approach, we can utilize a more general and suitable aerial image metric known as "normalized image log slope" (NILS) for IL as

$$NILS = CD\frac{dlnI_x}{dx} \quad (2.10)$$

Taking the derivative of I_x in equation (2.8) with respect to x and selecting the intensity that gives equal line and spaces, NILS of a periodic image can be found closely related to C as [102]

$$NILS = \pi C \quad (2.11)$$

Exposure latitude (EL) is a processing metric which gives information regarding relative dose variation that leads to 10% dimensional variation from the nominal size. For periodic dense patterns near the dose to size, exposure latitude is given as [102]

$$EL = \frac{NILS}{2}\frac{\Delta CD}{CD} = 10\%\frac{NILS}{2} = 10\%\frac{\pi}{2}C \quad (2.12)$$

2.1.1 *Effect of partial coherence on imaging*

The coherency of illumination source has significant impact on imaging. The previously shown formulae are valid for coherent light, meaning the incident light on the mask (or beam splitter) is coming from one direction only. In projection lithography tools, there is usually an angular distribution to the source which is defined by the partial coherence factor, σ, given as [3, 5]

$$\sigma = \frac{Source\ Diameter}{Lens\ DIameter} = \frac{NA_S}{NA_O} = \frac{nsin(\theta_{\max})}{NA_O} \quad (2.13)$$

A result of high coherence (i.e., small σ) after impinging upon any hard edge is called "ringing". Partial coherence of the illuminating source has a detrimental effect on the extent of ringing. In Fig. 2.2, a schematic definition of partial coherence and its effect on imaging is shown for conventional illumination and an isolated line. As it is seen, the smaller the sigma (i.e., the more coherent the light), the longer the ringing progresses. Line narrowed excimer lasers have small divergence angles; hence, resulting in ringing issues at field edges and point defect printing even for IL systems [16].

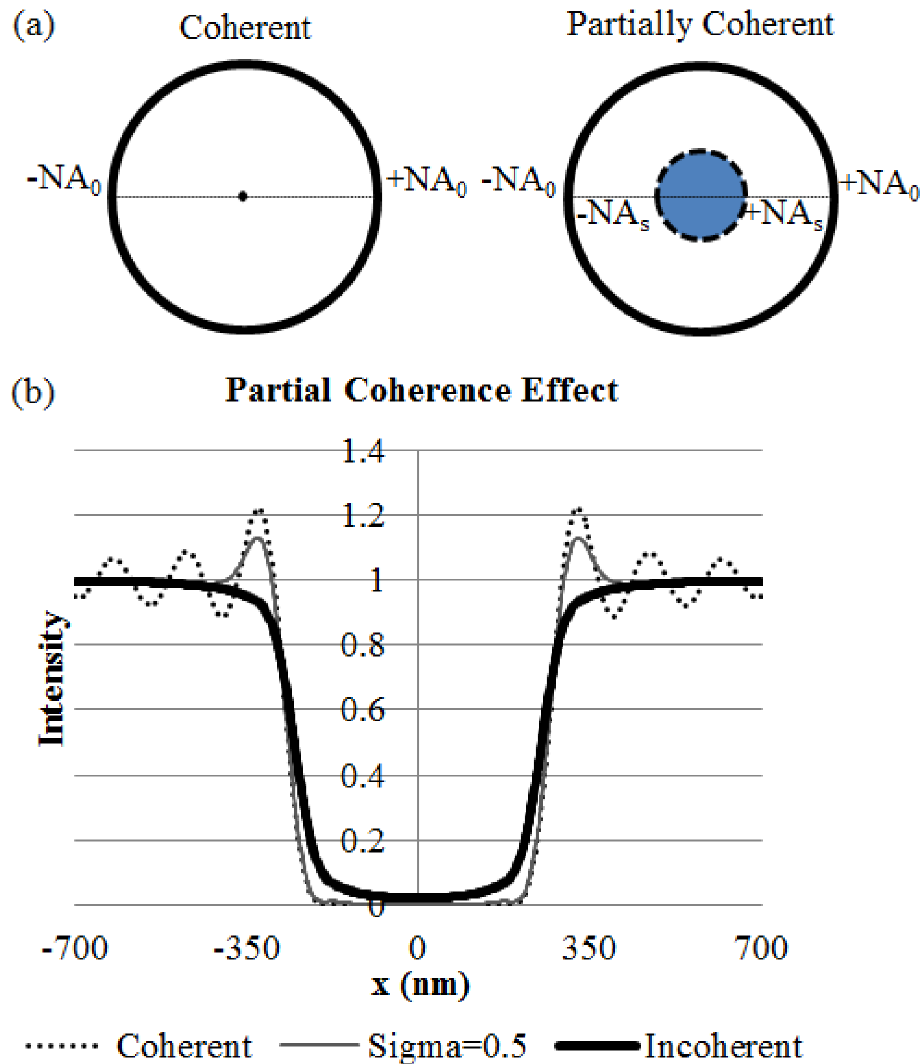

Figure 2.2: (a) Definition of partial coherence. (b) Effect of partial coherence on imaging for an isolated 500 nm wide line.

2.1.2 *Effect of aberrations on imaging*

Aberrations also impact the imaging behavior of lithography systems. Sources of aberrations can be grouped as design, construction or user originated. The aberrations of design are inherent to the imaging system and the goal of a lens designer is to reduce these aberrations as much as possible by including an optimum amount of optical elements into the system [3].

The magnitude of aberrations can be measured experimentally by interferometric tests or predicted by lens design software tools. The deviations in the paths of the rays from the ideal paths are expressed as optical path difference (OPD) and give magnitude of aberrations. Several measurements are taken across the entire image field to get enough sampling. That way, the aberrations in an optical system can be characterized through an OPD map [3].

There are many ways to mathematically express the lens aberrations. Most common method is to decompose the optical wavefront, W(r, ϕ), defining the aberration into orthogonal polynomial series called Zernike polynomials, as shown below

$$W(r,\phi) = \frac{OPD}{\lambda} = \sum_{i=0}^{\infty} a_i Z_i(r,\phi) \qquad (2.14)$$

where W represents the OPD normalized to the wavelength, and Z_i represents the Zernike term with a coefficient of a_i. Because Zernike terms are orthogonal to each other, they behave independently; hence adding or removing one polynomial term does not affect the best fit for coefficients of other Zernike terms [3].

Aberrations have unique effects on imaging. For example, tilt aberrations (Z_2, Z_3) will induce position shifts in x and y directions and astigmatism-like aberrations (Z_5, Z_6) will induce an orientation dependent focus shift. The amount of each Zernike coefficient determines the impact of each aberration [3].

In three-beam imaging, 0 and ±1 orders are used to create the aerial image. If there is defocus aberration in the system, the electric field at the image plane is given as

$$E(x) = a_0 + 2a_1 e^{i\Delta\phi} \cos(2\pi x/p) \quad (2.15)$$

Therefore the intensity of the aerial image with defocus becomes

$$I(x) = a_0^2 + 4a_0 a_1 \cos(\Delta\phi) \cos(2\pi\, x/p) + 2a_1^2[1 + \cos(4\pi\, x/p)] \quad (2.16)$$

where the defocus is denoted as ΔΦ and modulates the main cosine term in the above equation [3]. As the defocus is increased, the first diffraction orders will go out of focus relative to the zero order and the interference contrast will diminish if the defocus becomes a quarter of a wave [3].

2.1.3 *Effect of vibration on imaging*

Vibration and its effects on image have been studied extensively since the late 60s, especially for the photographic applications such as aerial imaging [103] and X-ray imaging [104]. Image vibration and relative motion between the image and photographic film results in degradation of image quality and can be included into the final image calculation in terms of an extra transfer function. This degradation can be in longitudinal

(along the optical axis) or transverse (perpendicular to the optical axis) direction and is represented with a unique transfer function depending on the type of the motion [105].

The effects of object-to-image vibration in an optical projection system were studied by [106, 107] with the purpose to quantitatively define maximum acceptable vibration level as a function of resolution and process latitude parameters. Instead of a transfer function in frequency domain, time domain histograms are used to characterize a vibration environment. It was shown to be very useful to utilize a vibration histogram to reveal the amount of dwelling at a specific location during exposure. The range of resolution studied was changing from 0.48 to 1.2 λ/NA [106, 107].

An example of measured vibration between the mask and wafer of an optical stepper is given in Fig. 2.3 (a) with its corresponding histogram (b). The histogram can be approximated to a more familiar function such as triangular shaped function in Fig. 2.3 (c), which has a peak dwelling time of $1/A_{TVH}$ and normalized to have an area of 1 [106, 107].

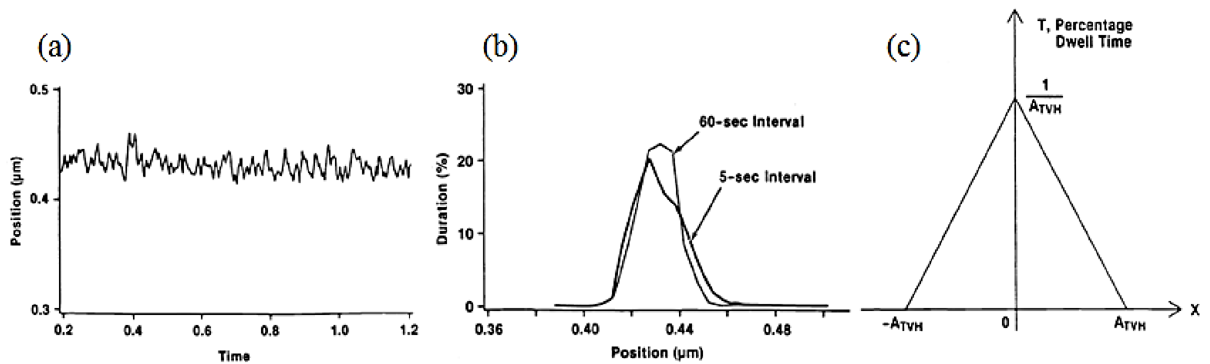

Figure 2.3: (a) Measured time vibration data for an optical stepper. (b) Corresponding histograms based on 5-s and 60-s intervals. (c) Triangular vibration histogram approximation to (b) [106, 107].

If the vibration has a dominant sinusoidal nature with single frequency component (see Fig. 2.4 (a)), the dwelling time will peak at the two extreme positions as shown in Fig. 2.4 (b). Time histograms of triangular shape and single frequency conditions are considered as the two extreme cases, where the latter represents the pessimistic case [106, 107].

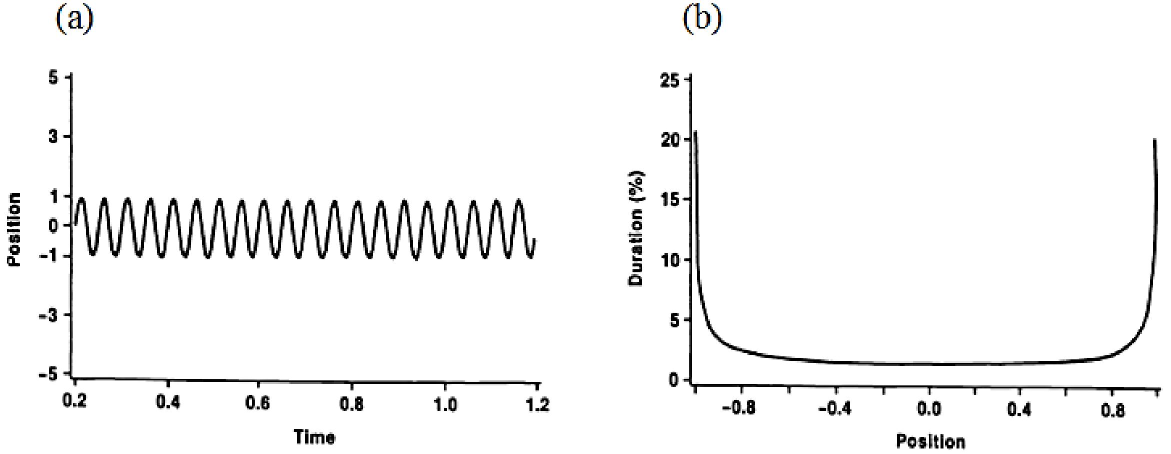

Figure 2.4: (a) Sinusoidal vibration of a single frequency. (b) Its histogram [106].

In order to mathematically model the effect of vibration (or translational image averaging) on an image, the static image needs to be evaluated initially. Vibration effect can be introduced according to the mathematical formulation below

$$I_v(x_s, y_s) = \frac{1}{(t_{max}-t_{min})}\int_{t_{min}}^{t_{max}}[I_s(x_s + x_v(t), y_s + y_v(t))]dt \tag{2.17}$$

where I_v and I_s are the vibrated and static image intensity distributions, respectively; x_s and y_s are static coordinates in the image plane and x_v and y_v are the perturbations to static coordinates caused by vibration source [106, 107]. In case of a sinusoidal vibration,

$$x_v(t) = V_x \sin(2\pi f_x t) \tag{2.18}$$

and

$$y_v(t) = V_y \sin(2\pi f_y t) \tag{2.19}$$

where V_x and V_y are the vibration amplitudes, f_x and f_y are the vibration frequencies. When the histogram method is utilized, the vibrated intensity distribution can be evaluated simply as

$$I_v(x_s, y_s) = \sum_{i=-n}^{n} I_s(x_s + x_i, y_s + y_i) T(x_i, y_i) \tag{2.20}$$

The histogram of vibration, $T(x_i, y_i)$, should be normalized such that

$$\sum_{i=-n}^{n} T(x_i, y_i) = 1 \tag{2.21}$$

Table 2.1 shows the vibration tolerances calculated by [107] in normalized and physical parameters as a function of the actinic wavelength and the lens NA, at k_1=0.64 and σ=0.8, for optimistic and pessimistic cases. The triangular vibration histogram amplitude is found to be a factor of 2 more tolerable than the sinusoidal amplitude [107].

Table 2.1: Summary of vibration tolerance at k_1=0.64 and σ=0.8 [107].

λ	NA	DOF	Resolution	Max. Vibration Amplitude	
				Pessimistic	Optimistic
Normalized	Normalized	±0.5	0.64	0.13	0.23
436nm	0.35	±1.78 μm	0.80 μm	0.16 μm	0.29 μm
"	0.45	±1.08 μm	0.62 μm	0.13 μm	0.22 μm
"	0.55	±0.72 μm	0.51 μm	0.10 μm	0.18 μm
365nm	0.35	±1.49 μm	0.67 μm	0.14 μm	0.24 μm
"	0.45	±0.90 μm	0.52 μm	0.11 μm	0.19 μm
"	0.55	±0.60 μm	0.42 μm	0.09 μm	0.15 μm
248nm	0.35	±1.01 μm	0.45 μm	0.09 μm	0.16 μm
"	0.45	±0.61 μm	0.35 μm	0.07 μm	0.13 μm
"	0.55	±0.41 μm	0.29 μm	0.06 μm	0.10 μm

2.2 Reduction Talbot Specific Derivations

Using the nomenclature shown in Fig. 2.5, important relationships between the set up parameters are derived for the reduction Talbot design such as diffraction angle, beam size, and mirror tilt angle with output parameters such as interfering angle, pattern pitch, exposure field size, and optical path differences across the field. Beam divergence is excluded in these calculations.

In Fig 2.5, the first order diffraction angle is denoted as θ, which can be calculated from illuminating wavelength (λ) and grating pitch ($p_{grating}$) as follows

$$\sin(\theta) = \frac{\lambda}{p_{grating}} \tag{2.22}$$

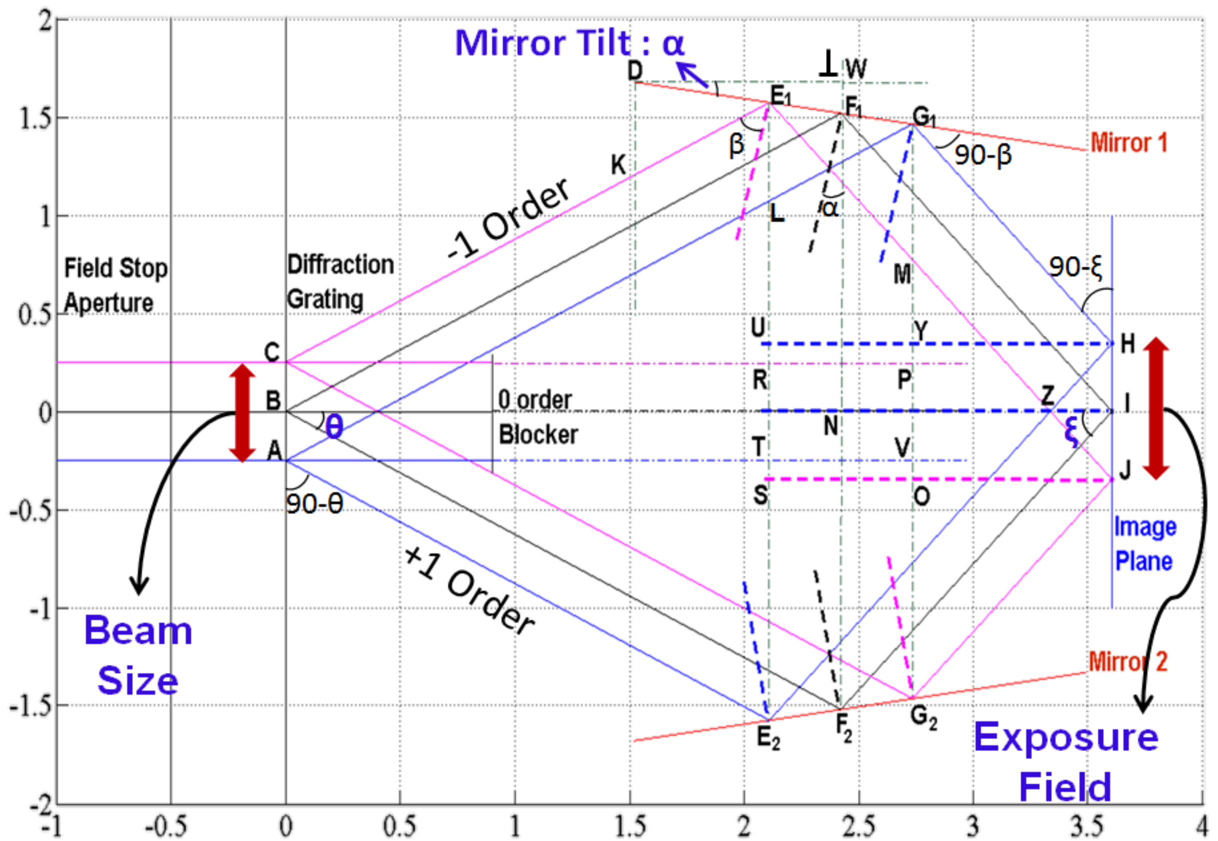

Figure 2.5: Schematic of reduction Talbot IL setup for important derivations.

The mirror tilt is denoted as α and the angle between the normal of mirror and the diffraction order impingent upon it is denoted as β. The relationship between θ, α, and β can be calculated from the triangle KDE_1 as

$$\theta + \beta + \alpha = 90^0 \tag{2.23}$$

The beam size is defined as |AC|, which is also equal to $|E_1L|$. Using the law of sines for E_1LG_1 triangle

$$\frac{|E_1G_1|}{\sin(90-\theta)} = \frac{|E_1L|}{\sin(90-\beta)} = \frac{|AC|}{\sin(90-\beta)} \tag{2.24}$$

and from (2.24), the relationship between the beam size and its projection along the tilted mirror can be defined as

$$|E_1G_1| = |E_1L| * \frac{\sin(90-\theta)}{\sin(90-\beta)} = |E_1L| * \frac{\cos(\theta)}{\cos(\beta)} = |AC| * \frac{\cos(\theta)}{\sin(\theta+\alpha)} \tag{2.25}$$

The interfering angle (ξ) can be calculated from BIF_2 triangle as

$$\xi = \theta + 2\alpha \tag{2.26}$$

By using law of sines on E_1MG_1 triangle, and noting that $|HJ| = |G_1M|$

$$\frac{|E_1G_1|}{\sin(90-\xi)} = \frac{|G_1M|}{\sin(90-\beta)} = \frac{|HJ|}{\sin(90-\beta)} \tag{2.27}$$

and from (2.27), the relationship between the exposure field size |HJ| and its projection along the tilted mirror can be defined as

$$|G_1M| = |HJ| = |E_1G_1| * \frac{\sin(90-\beta)}{\sin(90-\xi)} = |E_1G_1| * \frac{\cos(\beta)}{\cos(\xi)} = |E_1G_1| * \frac{\sin(\theta+\alpha)}{\cos(\theta+2\alpha)} \tag{2.28}$$

From (2.28), by using (2.25) for $|E_1G_1|$, we can derive the relationship between the exposure field size and beam size as given in equation (2.29). The field size defined here actually corresponds to the field length that is in perpendicular direction to the lines. The field height at the wafer plane will be the same as the input beam height impingent upon the grating,

$$|HJ| = |E_1G_1| * \frac{\sin(\theta+\alpha)}{\cos(\theta+2\alpha)} = |AC| * \frac{\cos(\theta)}{\sin(\theta+\alpha)} * \frac{\sin(\theta+\alpha)}{\cos(\theta+2\alpha)} = |AC| * \frac{\cos(\theta)}{\cos(\theta+2\alpha)} \quad (2.29)$$

From (2.29), it can be observed that if mirrors are not tilted (α=0°), exposure field is equal to the beam size. As the mirror tilt is increased, exposure field gets larger than the beam size.

The interference pattern pitch is determined by the source wavelength (λ), the refractive index of the interfering medium (n) and the interfering angle(ξ) as

$$p = \frac{\lambda}{2n\sin(\xi)} = \frac{\lambda}{2n\sin(\theta+2\alpha)} \quad (2.30)$$

The left and right handedness is preserved in the Talbot design. There exists a location at the image side where two orders completely overlap with each other, which can be interpreted as the “focal plane” of the IL system. At this location, each point in the image plane is resulted from the same point source diffracted from the grating. This alleviates the spatial coherence requirements, if operating at the focal plane [101].

On the other hand, temporal coherence plays a critical role for large field IL printing. This strongly relates to the spectral width of the excimer laser and its coherence length. The reduction in image contrast is a result of the “beating” phenomenon. The detrimental effect of having a broad band source is the gradual shift of the intensity peaks

corresponding to each wavelength away from each other; as moved away from the field center. Eventually, summation of these intensity values will wash away the fringes and contrast will reduce to zero. Some type of wavelength dispersive optical elements such etalons, diffraction gratings, or prisms can be introduced in the resonating chamber in order to narrow down the spectral line to picometer levels [101].

Even with line narrowing, the high contrast region is still on the order of few millimeters. The beating frequency, which defines useful image area, is related to the source temporal coherence length and set up parameters. Lowering the beating frequency increases the useful imaging area and increases the beating period, L. If mirrors in the Talbot design are not tilted, wavelength dependence on pattern pitch is eliminated and the system becomes achromatic [101].

For chromatic IL systems, temporal coherence length (l_c) of the laser is very important. It depends on the mean wavelength (λ) and the source bandwidth (Δλ) as [21]

$$l_c = \lambda^2/\Delta\lambda \tag{2.31}$$

A 193 nm laser source with a spectral width of 0.5 pm will have a coherence length of about 75 mm. Considering the maximum field size defined in ITRS is 26 mm by 33 mm, this coherence length might suffice for large field applications. However, there will be contrast degradation moving away from field center to field edge [101].

2.2.1 *Effect of OPD on field size*

Aside from beating, another factor that reduces the contrast in reduction Talbot design with tilted mirrors is the optical path difference (OPD) between two diffraction orders. It can easily be understood by looking at the problem in Fourier perspective [108], as shown in Fig. 2.6.

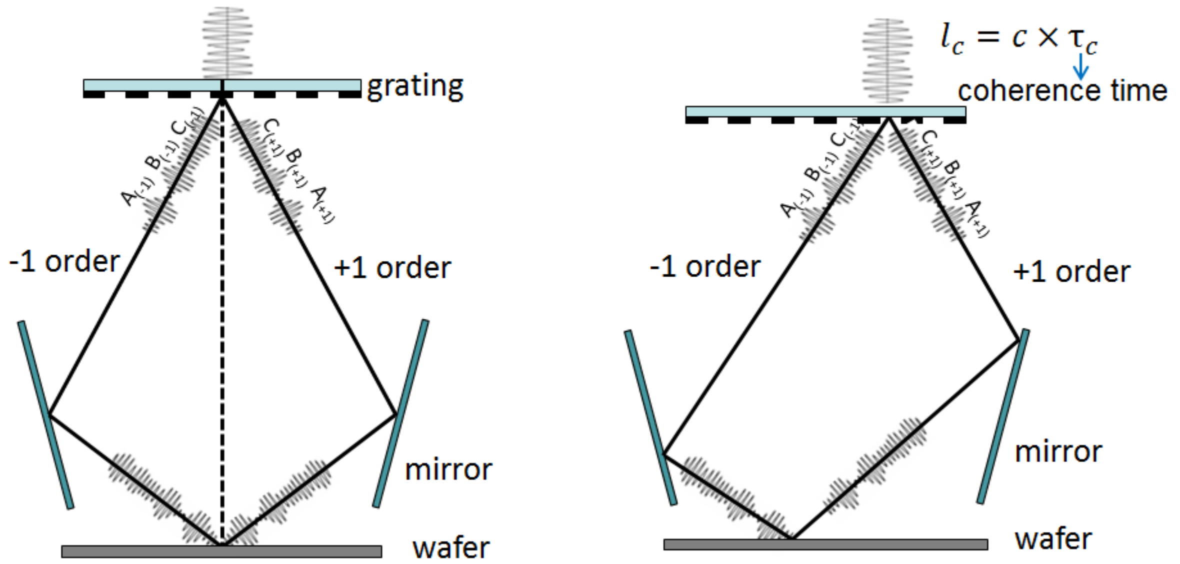

Figure 2.6: Effect of optical path difference (OPD) on interference of correlated wave groups (modified from[108]).

When the mirrors are tilted, +1 and -1 orders will travel different path lengths. The difference will increase as the distance away from the field center is increased. If a source point diffracting from the grating is assumed to be composed of several wave groups, as long as the OPD between the orders is less than the temporal coherence length, correlated wave groups will interfere with each other at the image plane. If the OPD is greater than the coherence length; then, uncorrelated wave groups will arrive at the image

plane to interfere at the same time and their ability to constructively and destructively interfere will be much reduced [108].

Fig. 2.7 shows the degradation of image contrast when moving away from field center both due to beating and OPD. For large IL fields, need for a line narrowed laser is evident from the figure. OPD increases the rate of contrast degradation in addition to the beating effect. The theoretical derivation of OPD for reduction Talbot design based on set up parameters is given in Appendix A. It should be noted that the mirror tilt has a strong effect on OPD.

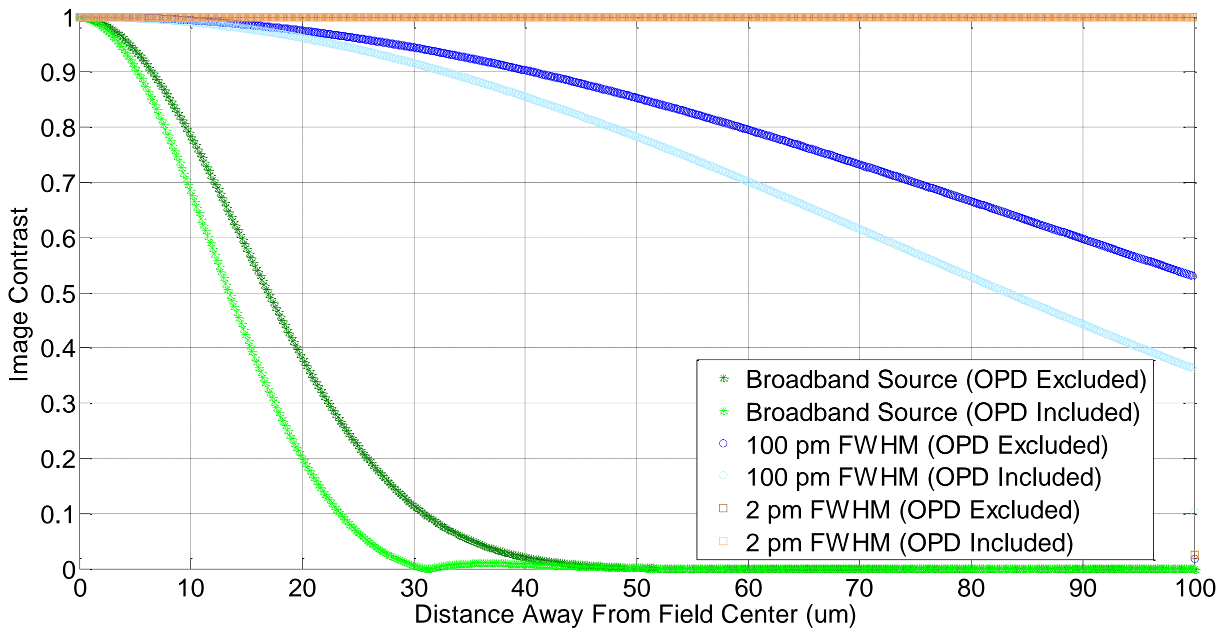

Figure 2.7: Effect of OPD and source bandwidth (i.e. beating) on image contrast degradation across the field for 193 nm ArF laser. Three different source bandwidths are considered: broadband, 100 pm FWHM, and 2 pm FWHM.

2.3 **Line Edge Roughness (LER)**

LER is defined simply as the sidewall deviations of a printed line from a straight line fit [109]. There are several contributors to LER such as chemical/optical shot noise, random nature of acid diffusion, development process, and concentration of acid generator/base quencher [18, 19, 110]; but, they can be divided into two categories as:

(1) Chemical properties and processing of the resist related, and

(2) Aerial image related (containing optical properties of the mask and stepper).

It can be measured as a single 3σ value; however, power spectral density (PSD) is a better metric to distinguish the contribution of different roughness frequencies on the overall LER [19, 98]. The specifications for LER is usually about 5% of the nominal CD value; however, LER values of 4 nm and larger are very common [111].

ITRS defines the LF LWR requirements, as shown in Table 2.2 [32]. By 2015, LF LWR of less than 1.8 nm is demanded from the process. Such low LER/LWR values are extremely difficult to achieve with state of the art resist/processing techniques.

Table 2.2: 2011 Edition ITRS LWR requirements (generated from data of [32])

Production year	**2011**	**2013**	**2015**	**2017**	**2019**	**2021**
DRAM hp (nm)	36	28	23	18	14	11
Low frequency LWR (nm, 3σ)	2.8	2.2	1.8	1.4	1.1	0.9

In reference [110] a proposed framework for LER/LWR modeling is given as in Fig. 2.8. The top group listed under sources of LER is resist material and processing

related contributors, and the bottom group consists of optical effects, mask roughness and others that do not belong to the first group [110].

As far as resist-internal LER sources are concerned, the first one is the stacking of finite size molecules, which gives a white noise spectrum. However, the amplitude can be ignored because its contribution is mainly in high frequency range which is filtered out in the processing. Random absorption of photons gives a white noise spectrum, which also gets low pass filtered during the PEB via diffusion. Acid diffusion will reduce the high frequency component of the photon noise; however, it adds new high frequency randomness due to erratic behavior of random walk and deprotection by small number of acid molecules. The smoothing function becomes dominant and gives a high frequency roll off above around 10 cycles per μm (45-65 nm hp). This is approximately the same high cut off frequency for the mask related LER in most cases [110].

There have been attempts to develop a comprehensive stochastic model for LER based on approximate expressions for variances and correlations that occur at every step of the lithographic process, starting from photon shot noise [112]. From such a study, it is concluded that there is an optimum acid diffusion length that minimizes LER and that the development step has a significant impact on it. The effect of speckle was excluded from this study; however, other groups reported their results regarding the effect of speckle on LWR.

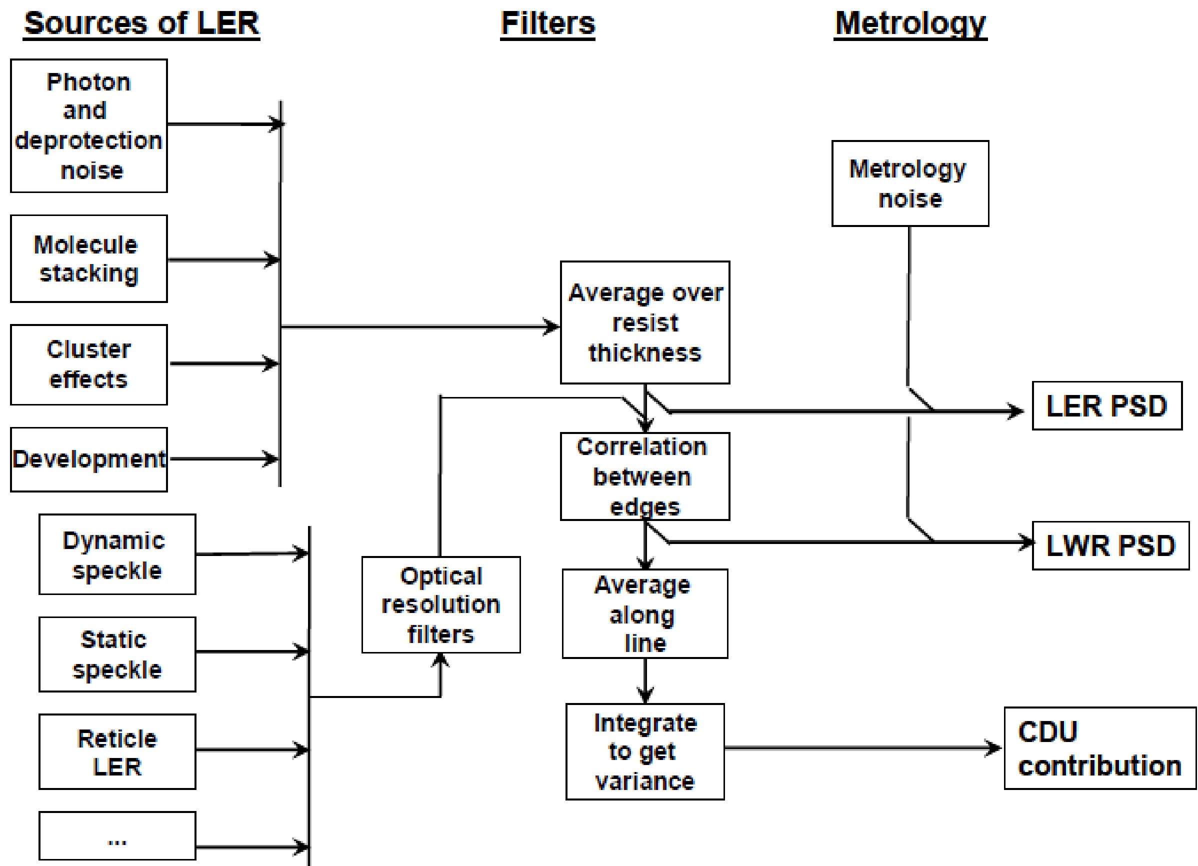

Figure 2.8: LER framework proposed by [110].

For example, Fig. 2.9 shows the contribution of speckle in the overall LWR for 5 different type of resists reported by [113]. Speckle results in non-uniform illumination of the reticle, therefore, crucial in definition of edge in transitions between high and low intensities. On the same figure, ITRS requirements for LWR throughout the years are depicted as well. By looking at the results for resist A, it can be seen that speckle-induced LWR is more than 15% of the total LWR. However, this number should not be taken as is for different conditions; since, the speckle contribution depends on the coherency of source (more on temporal coherence than the spatial), illumination wavelength, and distribution of source image on the pupil plane. Nevertheless, speckle induced LWR is

found to be observable and should not be ignored while extending ArF optical lithography toward more advanced technology nodes [110, 112, 113].

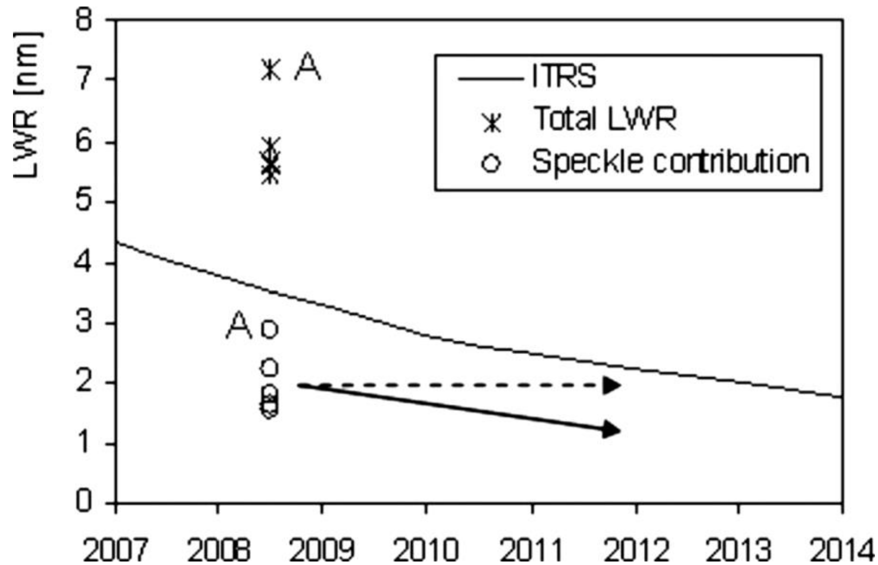

Figure 2.9: ITRS LWR roadmap, shown with total LWR (3σ) and contribution of speckle for 5 different resists. Resist A is highlighted for discussion [113].

Speckle can be divided into two groups: (1) dynamic speckle, and (2) static speckle. The former is of concern for partially coherent pulsed laser source applications. It is a result of incomplete time averaging of the instantaneous intensity over one or several pulses [110].

The variation of static speckle from pulse to pulse is very small (or nonexistent); therefore, it is usually excluded in the LER models. Static speckle can change due to thermal variations or turbulence in the environment. Scrambling or time delaying parts of the beam can be utilized to reduce the static speckle [110].

Another factor that affects LER is the thickness of the resist film. It has been showed LER significantly depends on the thickness of the photoresist material under

similar processing conditions [114, 115]. The effect of resist thickness on LER can be seen in Fig. 2.10 for two resist materials (resist B having 2.5 times more photo-acid generator than resist A) and thicknesses varying from 60 nm to 250 nm. As it seen from the figure, LER is significantly higher for thinner film thicknesses. It has also been observed by the authors that increasing photo-acid generator concentration decreased the LER for the same resist thickness, probably due to reduced chemical shot noise [114].

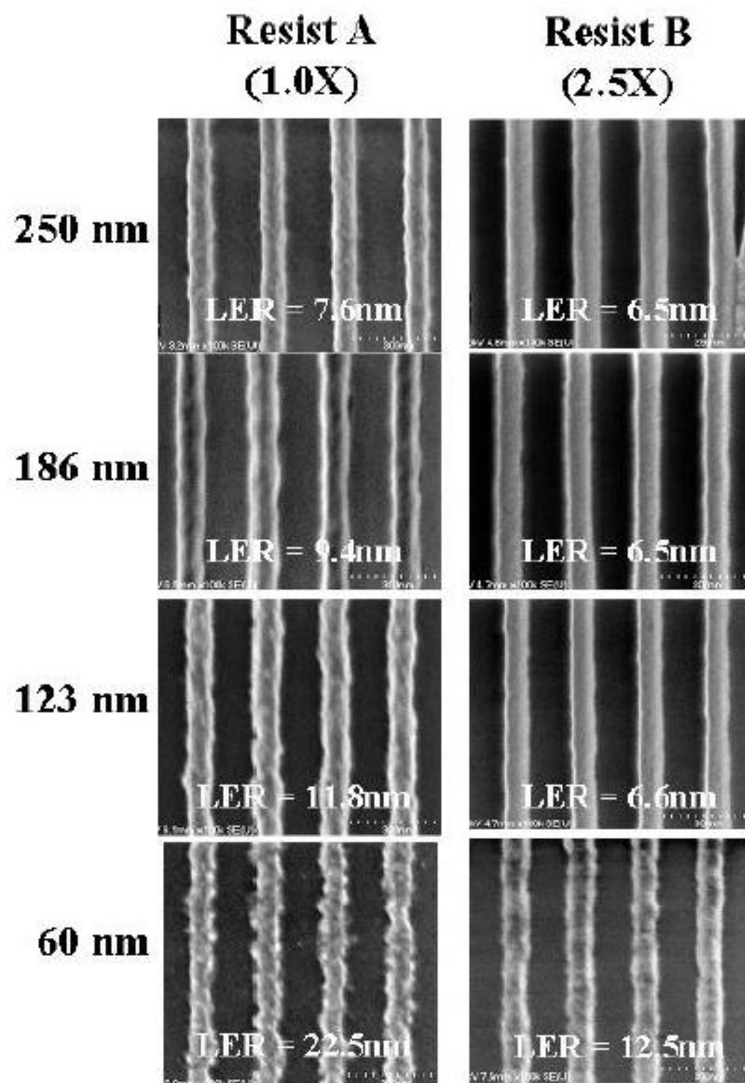

Figure 2.10: SEM images depicting LER for varying resist thicknesses and for two resists with different sensitivities. Resist B has 2.5X more photo-acid generator concentration than resist A [114].

The effect of aerial image modulation (contrast) on LER is shown in [116, 117] for a variety of resist systems including negative and positive tone resists, chemically amplified and chain scissioning resists, aqueous and solvent developable resists, and also for different lithography systems. For all materials, it was observed that as aerial image contrast is decreased, LER increases due to widening of the intermediate transition region. From these studies, it was concluded that higher contrast leads to lower LER. It was also noted that UV6 resist is more sensitive to aerial image modulation than the chain scissioning PMMA resist [116]. These results are given in Fig. 2.11.

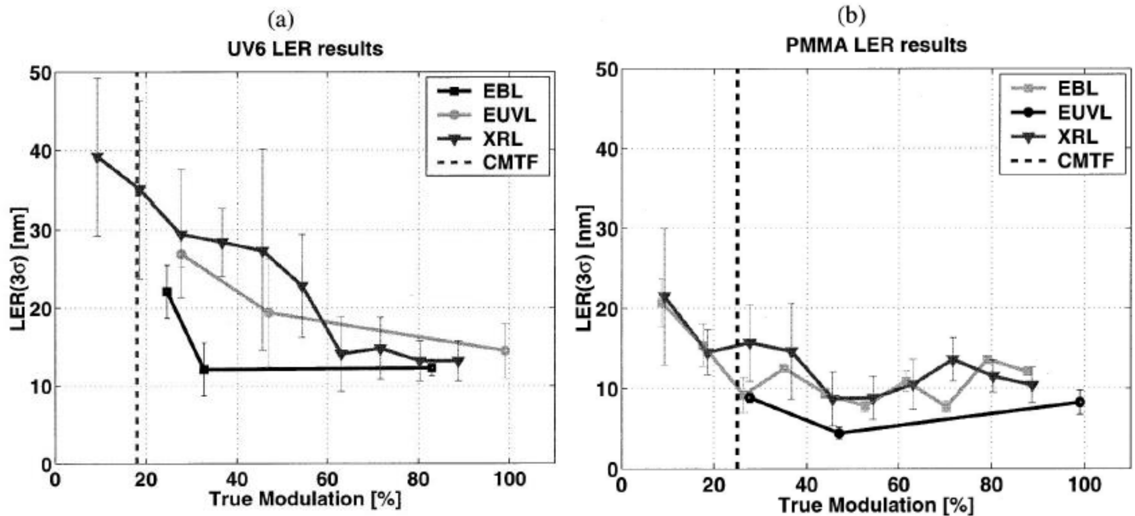

Figure 2.11: LER degradation as a function of contrast loss shown for (a) UV6 chemically amplified resist, and (b) PMMA chain scissioning resist [116].

Under same conditions, there is no lithography technique that would achieve higher theoretical image contrast than IL. Therefore, IL systems result inherently in lower LER values compared to conventional lithography techniques. A group investigated this by comparing imaging performance of an immersion scanner (ASML Twinscan / 1150i) with IL system of different modulations on 90 nm dense line/space pattern. The details of

their study can be found in [118]; however, one of their important findings is included here in Fig. 2.12. From this figure, it can be seen that IL imaging results in lower LER than the projection system, even though the former is deliberately demodulated (56% modulation) and the latter is performing at best focus [118].

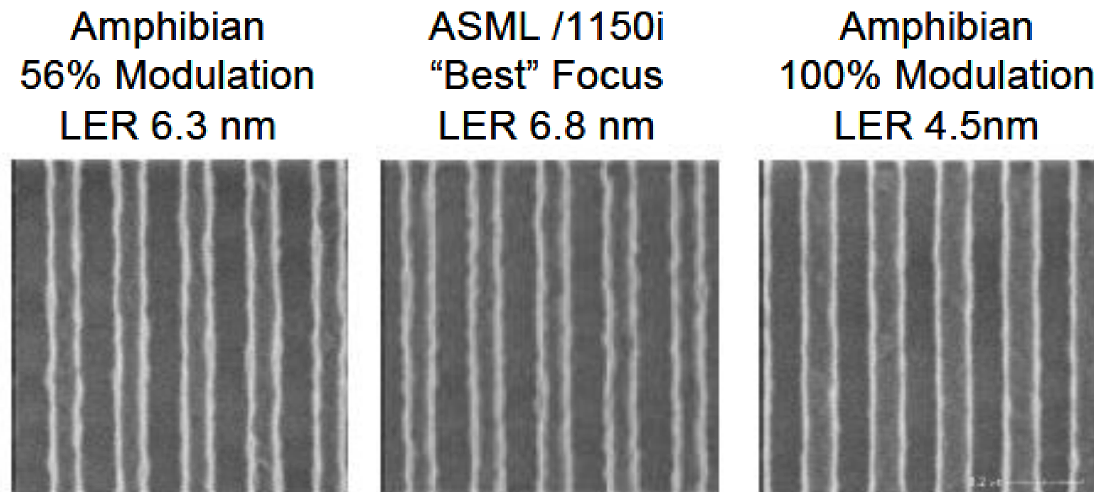

Figure 2.12: LER comparison of 90 nm dense line/space pattern for an IL system (Amphibian) and ASML /1150i [118].

LER and LWR have significant impact on device performance and reliability [98]. The effect of LWR for sub-100 nm NMOS devices for low power SRAM were investigated experimentally by fabricating 80 nm node transistors of varying gate length, width, and roughness values [119]. One of the findings of the research is that the effect of roughness becomes visible for critical dimension (CD) values less than 85 nm. Fig. 2.13 shows these results, where the variation in electrical device parameters such as threshold voltage (V_{th}) and off-state-current (Io_{ff}) are more evident for small CD values. The variation in I_{off} can be 4 orders of magnitude for CD less than 75 nm [119].

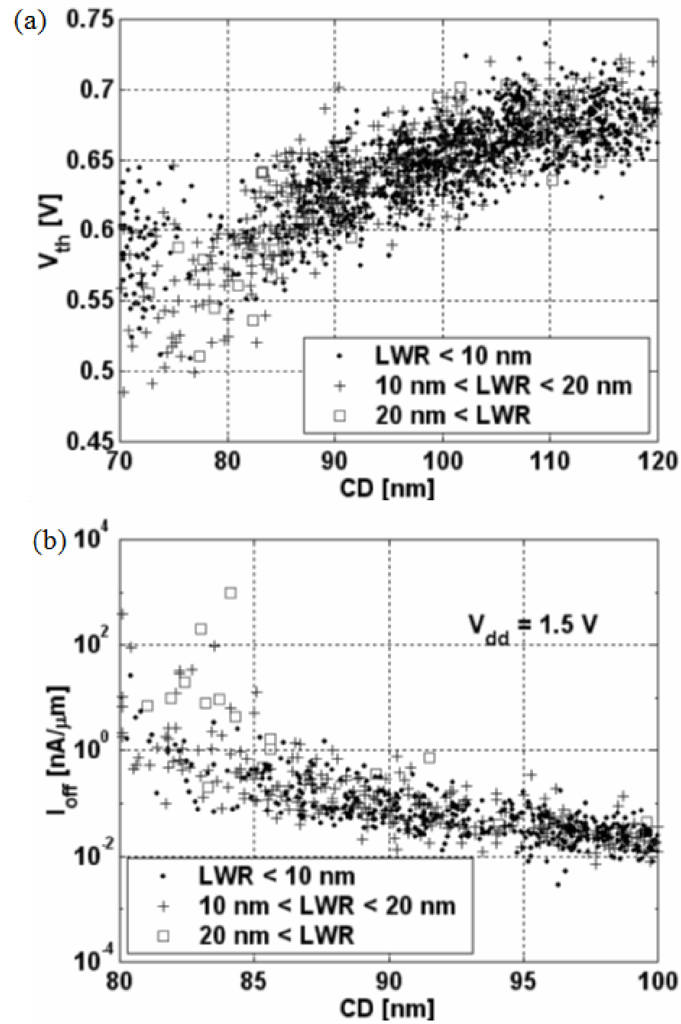

Figure 2.13: The effect of LWR on (a) V_{th}, (b) I_{off} variability [119].

A simulation study was performed by [120] on 16 nm FinFET devices and the results are given in Fig. 2.14 where each data point corresponds to device variability for a 100 member FinFET device population with a single spatial roughness period. As it is easily seen, low frequency roughness has a more dominant impact on the device electrical variability and I_{off} has a higher sensitivity than other parameters. It is also noted that the reliability requirements push the critical frequency range to include more frequencies [120].

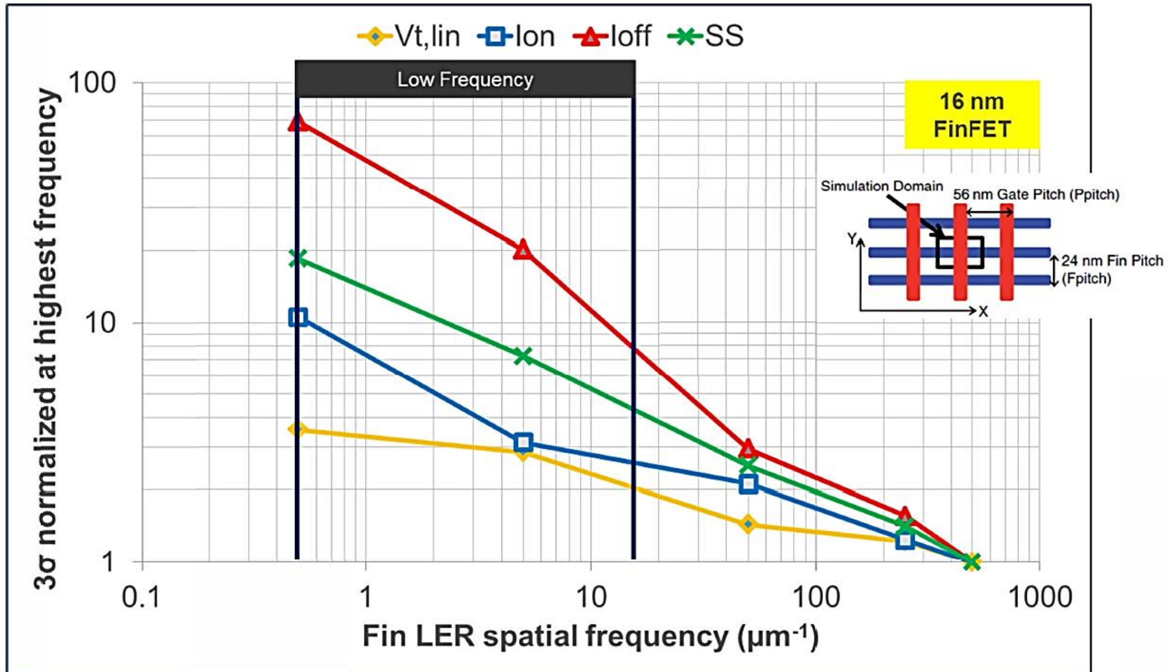

Figure 2.14: The FinFET device performance variability as a function of roughness frequency for the same amplitude [120].

Recently, mask roughness is gaining significant attention as one of the contributors to wafer LER [19, 97, 121-127]. Its influence region can be seen in Fig. 2.15 (a). In the mask making process, there are high frequency and low frequency roughness contributors. The former is a result of the stochastic nature of electron beam exposure, chemically amplified reaction-diffusion, and etching process with length scales of less than 100 nm [97].

The mask writer induces low frequency roughness, due to errors in shot placement or rotation, which can pass as long as the frequencies are below the cut-off, especially in high MEEF regions of the image [97]. In some cases, mask induced roughness might be as large as the full resist LER budget. Therefore, improved masks are a must for advanced technology nodes [128].

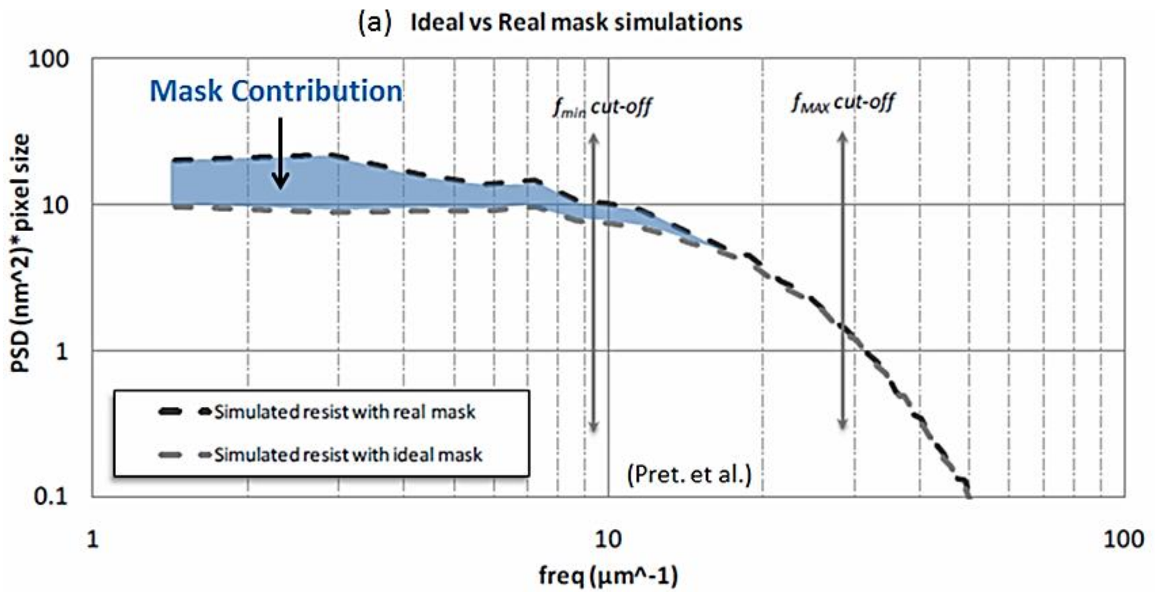

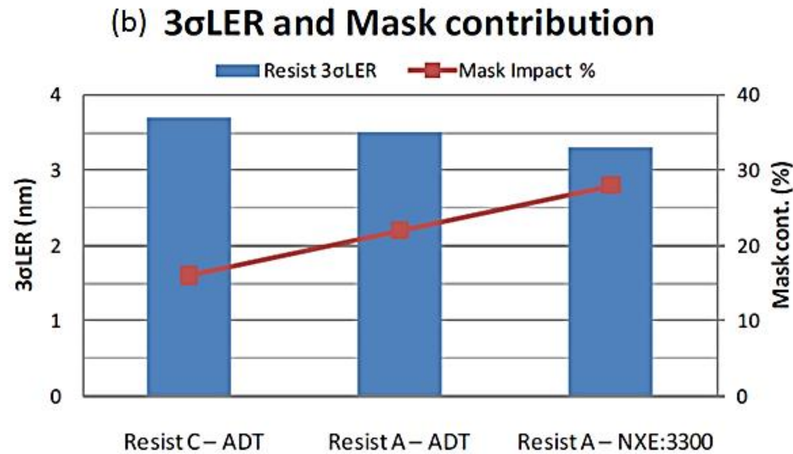

Figure 2.15: (a) The mask roughness influence region [129]. (b) Mask roughness contribution as a function of resist quality and optical system cut off frequency [126].

Fig. 2.15 (b) shows the effect of improved optical process on mask roughness contribution by comparing ASML's ADT and NXE EUV tools. By utilizing a larger NA system (NA=0.32, σ=0.5) with a tool such as NXE3300, the mask roughness contribution gets larger compared to ADT (NA=0.25, σ=0.5) [126].

2.3.1 *Mask roughness transfer*

In Fig. 1.1, a simplified version of a projection lithography set up was shown. The objective lens location corresponds to the pupil plane, where the diffraction information of the mask is present. As an example, the diffraction information from an ideal mask with vertical line space pattern is shown in Fig. 2.16 (a). The objective lens is large enough to capture the 0th and the first diffraction orders for conventional illumination with a finite partial coherence. If the mask absorber edges exhibit roughness, the roughness diffraction information from a non-ideal mask will lie perpendicular to the main diffraction information of the smooth vertical line space patterns, as shown in Fig. 2.16 (b) for the main 0th order. Depending on the roughness frequency, first order diffraction can be fully captured, partially captured or not captured at all. This frequency dependent transfer of mask roughness to the wafer plane can be best described by LER Transfer Function (LFT); a simplified LTF function is shown in Fig. 2.16 (c) [19, 123, 125].

Assuming a mask layout with a line edge on the x axis, mask LER can be defined by the fluctuation function in the x axis as $h_{mask}(x)$. When the mask is exposed, this roughness will be transferred to the wafer side as $h_{wafer}(x)$. Since it is conventional to define transfer function in frequency domain, LTF can be defined as the ratio of Fourier transforms of $h_{wafer}(x)$ and $h_{mask}(x)$ as [125]

$$LTF(f_x) \equiv H_{wafer}(f_x)/H_{mask}(f_x) \quad (2.32)$$

where $H_{wafer}(f_x)$ and $H_{mask}(f_x)$ corresponds to the Fourier transforms of wafer and mask roughness. Assuming a reduction ratio of 4, both x axis and h(x) are normalized by 4λ/NA for mask and λ/NA for wafer.

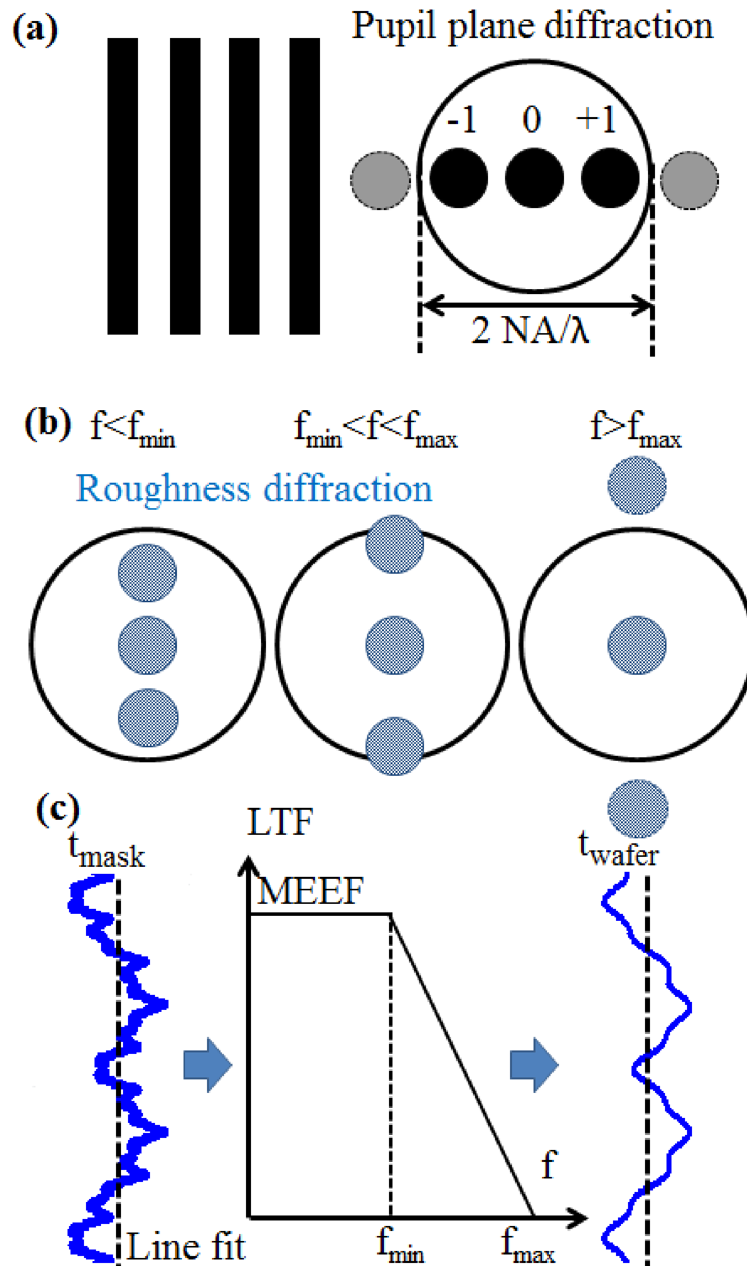

Figure 2.16: (a) Ideal mask diffraction information at the pupil plane. (b) Roughness diffraction order filtering by the optical system. (c) Simplified LTF definition.

The maximum frequency that can be passed by the NA limit of the system is NA(1+σ)/λ, where σ defined the partial coherence of the conventional illumination. The lowest frequency is shown as zero, and the LTF amplitude for that case is equal to the mask error enhancement factor, MEEF. Therefore, high frequency part of the mask roughness is filtered out by objective lens NA and the low frequency part is amplified by the MEEF of the system [19, 97, 125]. These two extreme conditions are shown as

$$LTF(f_x) = 0 \text{ for } f_x \geq NA(1+\sigma)/\lambda \tag{2.33}$$

$$LTF(0) = \frac{H_{wafer}(0)}{H_{mask}(0)} \equiv MEEF \tag{2.34}$$

NILS is an important parameter since to the first order; wafer LER will be inversely proportional to the NILS of that feature. High NILS makes a feature less sensitive to the random variation that induces LER. Due to the NA limit, roughness with frequencies above cut off will not be transferred to the wafer. However, they can cause a reduction in NILS and indirectly cause an increase in LER of the printed image. The high frequency roughness around the mask edge can be treated as a gray boundary covering that edge with a width of w_r. NILS can be easily calculated for the case of dense line space pattern with nominal width, w, and imaging with coherent illumination as [97]

$$NILS = NILS_0 \cos\left(\frac{\pi w_r}{2w}\right) \tag{2.35}$$

where $NILS_0$ is the NILS when roughness is excluded (w_r=0), and pattern is assumed to be formed by 0 and ±1 orders. If $w_r \ll w$, cosine term can be expanded by using Taylor series and keeping the first terms as [97]

$$NILS \approx NILS_0 \left[1 - \left(\frac{w_r}{0.9w}\right)^2\right] = NILS_0 \left[1 - \left(\frac{w_r}{aw}\right)^2\right] \text{ where a=0.9} \quad (2.36)$$

Above equation shows that NILS will reduce quadratically as the amplitude of high frequency roughness is increased. This formula is derived for coherent illumination; however, quadratic fall of NILS for annular, dipole, and quadruple were verified by simulations for $0.9 < a < 1$. It is noted in [97] that as long as $w_r<0.1w$ (where w_r is $3\sigma_{rms}$ of mask roughness), NILS will reduce only 1%. So, if the high frequency mask roughness is low enough, its degrading effect on NILS can be ignored [97].

For EUV lithography, mask roughness induced LER is a result of two sources: (1) mask absorber roughness, and (2) multilayer replicated surface roughness (RSR). Fig. 2.17 shows schematic depiction of these two sources [130].

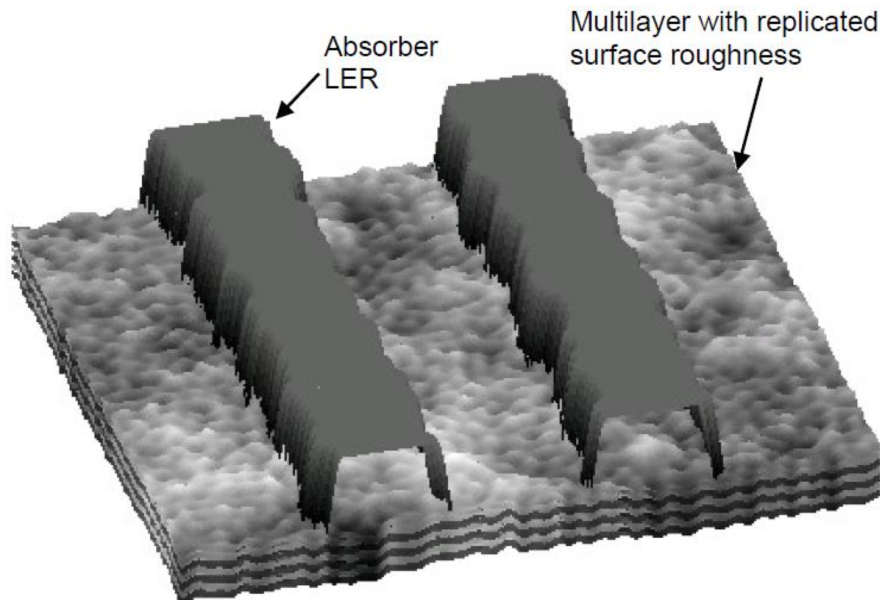

Figure 2.17: Schematic of two main sources of mask induced roughness for EUV: absorber roughness and replicated surface roughness [130].

The first contributor is easily understood by use of LTF, in a similar sense to the conventional optical lithography. However, the latter contributor is EUV specific and less obvious at first. It comes from the phase roughness in the clear regions of EUV mask, and due to the extremely short wavelength of EUV light, might have a significant effect. This roughness will couple with the intensity dependent variations through speckle and be more dominant than the absorber roughness [130].

Replicated surface roughness (RSR) fundamentally originates from the substrate and propagates to the surface during conformal deposition of multilayers. There is inherent low pass filtering during this process. The phase roughness due to RSR can be calculated as follows [130]

$$RSR_{Phase\ Roughness} = RSR\,\frac{2\pi}{\lambda_{EUV}} \tag{2.37}$$

2.3.2 *Previous LER mitigation attempts*

Many techniques have been utilized to mitigate wafer level pattern sidewall roughness such as hard-bake [131], plasma treatment [132], special rinses and ion beam sputtering [133]. Such techniques can be performed during or after the lithography process and have unique advantages and disadvantages. Post-lithographic rinses and solvent vapor smoothening have been shown to be useful for mitigating MF and HF roughness to some degree [133]. However, in order to reduce device parameter variations, mitigation of the LF roughness is much more desired. Fig. 2.18 (a) shows the effect of surfactinated rinse (SR) followed by a hard bake on LER PSD, when a SR is used instead of deionized water (DIW) rinse [134]. The ITRS specification is also shown

on the plot. Both UV-vapor and plasma treatments showed significant improvements in the LF/MF region, at the expense of CD loss in nanometers [133, 134].

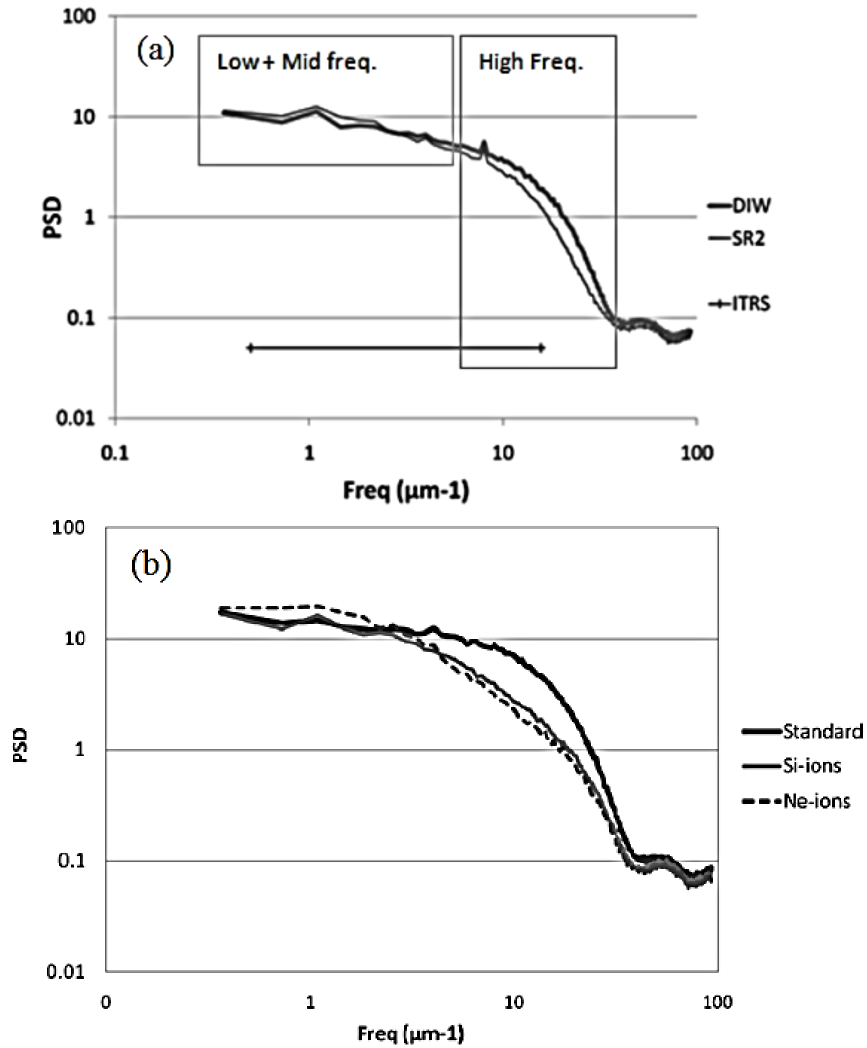

Figure 2.18: Effect of (a) special rinse, and (b) ion beam smoothing techniques on LER PSD [134].

The ion beam smoothing technique is usually performed at the implanter under grazing incidence for one directional features. Fig. 2.18 (b) shows its effect on 40 nm LS patterns defined by EUV process. Even though some reduction in roughness is observed, the drawback is 10 nm CD shrink due to the ion induced shave off [134].

2.4 **Speckle Theory in Imaging**

The speckle theory in optical lithography has been studied previously [135, 136]. Excimer lasers used in optical lithography have limited source bandwidths and finite pulse lengths, resulting in stochastic illumination fields [135]. This is one of the reasons for dose non-uniformity issues at the wafer plane, ultimately contributing to LER [135, 136]. Increasing the pulse duration with respect to the laser coherency time (τ_c) will result in a smoother intensity distribution as shown in Fig. 2.19, due to accumulation of several speckle fields. When the pulse duration is extended to 10 (Fig. 2.19 (b)) or 100 (Fig. 2.19 (c)) times the laser coherency time, the intensity fluctuations (W/<W>) are significantly reduced compared to the short pulse duration case (Fig. 2.19 (a)) [135].

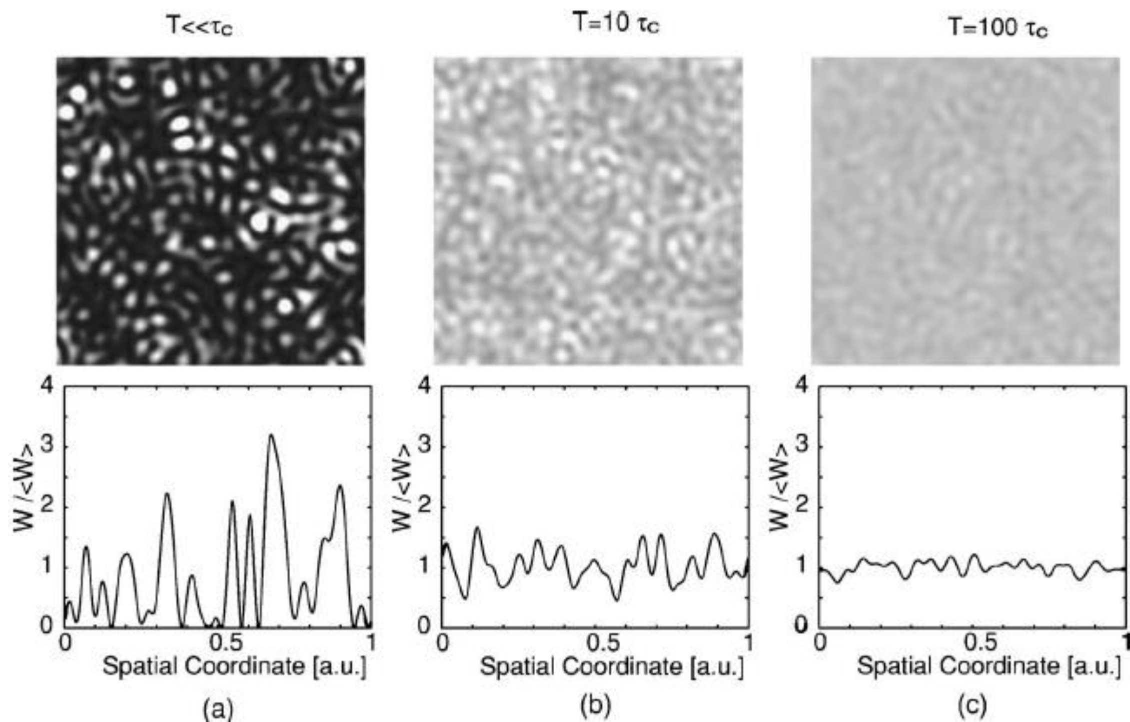

Figure 2.19: Effect of increasing pulse duration with respect to the coherence time. Integrated dose (W) has less of a variation for longer pulses. $T \ll \tau_c$ corresponds to the conventional (static) pattern [135].

In [113], the speckle effect (non-uniform dose delivery on reticle) for ArF lithography and its influence on line width roughness was investigated in details. The laser bandwidth, i.e. temporal part, and the laser pulse duration were found to be the dominant factors for speckle seen in ArF optical lithography. The spatial distribution of the speckle pattern was shown to be dependent on the source distribution at the pupil plane. They also reported the strong dependency of speckle induced LWR spatial frequency content on the experimental illumination conditions. Following a very similar approach to the previous method, speckle contrast resulting from N_{pulses} with temporal coherency time of τ_c was calculated as [113]

$$C_{speckle} = \sqrt{\frac{\lambda^2}{A_{field}\Omega_{divergence}} + \frac{1}{N_{pulses}}\frac{\tau_c}{TIS}\frac{1}{\sqrt{N_{polarization\,states}}}} \qquad (2.38)$$

where $\Omega_{\text{divergence}}$ is the effective solid angle of the angular intensity distribution of the laser, and A_{field} is the ratio of the square of intensity integration over the field to the integration of squared field intensity. Its equivalent in time domain is “TIS”, which is the ratio of square of time integration of intensity to the integration of intensity square [113].

Eqn. (2.38) was derived for a static imaging system; however, in reality, exposures are done in a scanning fashion. Therefore, for each laser pulse, different parts of the speckle pattern will deliver light to the same location on the reticle, resulting in an averaging effect. In order to account for this, calculated speckle contrast ($C_{speckle}$) should be multiplied by the following term

$$\frac{1}{\sqrt{N_{scanning}}} = \sqrt{\frac{v_{scan}}{w_{effective\,slit}f_{laser}}} \qquad (2.39)$$

where repetition rate is f_{laser}, effective slit width is $w_{effective\ slit}$ and scanning speed is ν_{scan} [113].

For translating the contrast of the speckle pattern at reticle level to the line width variation at the resist plane, we need to multiply the speckle contrast with the sensitivity on dose (reflecting amount of linewidth change in nm when changing the exposure dose, with same amount across the entire field), and $K_{speckle}$ (a parameter that defines the correlation between the edges, it varies between 1 and $1/\sqrt{2}$, depending on the edge correlation). The unit of dose sensitivity is nm CD change per percent dose change and can be determined by either simulations or experimentally from the focus exposure matrix (FEM). The conversion formula is given as follows [113]

$$LWR\ (1\sigma) = K_{speckle}(Dose\ Sensitivity)C_{speckle} \qquad (2.40)$$

From comparison of measured LWR to the theoretical speckle calculations, it is concluded that about 10% of LWR fluctuation can come from speckle for normal scanner operations [113]. The contribution depends on actual experimental conditions.

From these discussions, it can be concluded that lower dose sensitivity and smaller coherency time would result in less speckle effects. The latter case calls for wider source bandwidth, which is usually not desired. The reduction in speckle contrast can be achieved by increasing the repetition rate and accordingly reducing energy of each pulse, or by using passive pulse stretchers [137]. However, reducing LWR through changes in the exposure equipment will probably sacrifice throughput, since exposing field is attenuated and the required exposure time is expanded to span across a larger number of coherency times (τ_c).

2.5 **Pupil Filtering Applications**

The effect of pupil filtering on mask roughness transfer is a big part of this research. Pupil plane filtering (either in amplitude or in phase) has historically been used for other applications such as increasing DOF [138], enhancing minimum resolution [139] and more recently for compensating mask 3D effects [140]. For each application, an optimized filter design was generated that enables an additional plane for optimizing the lithography performance, in addition to mask and source planes.

Fig. 2.20 and 2.21 show examples of increasing the DOF and increasing the resolution. As shown in Fig. 2.21, pattern half pitch of 22 nm was resolvable only by use of a transmission pupil plane filter for resist A [139].

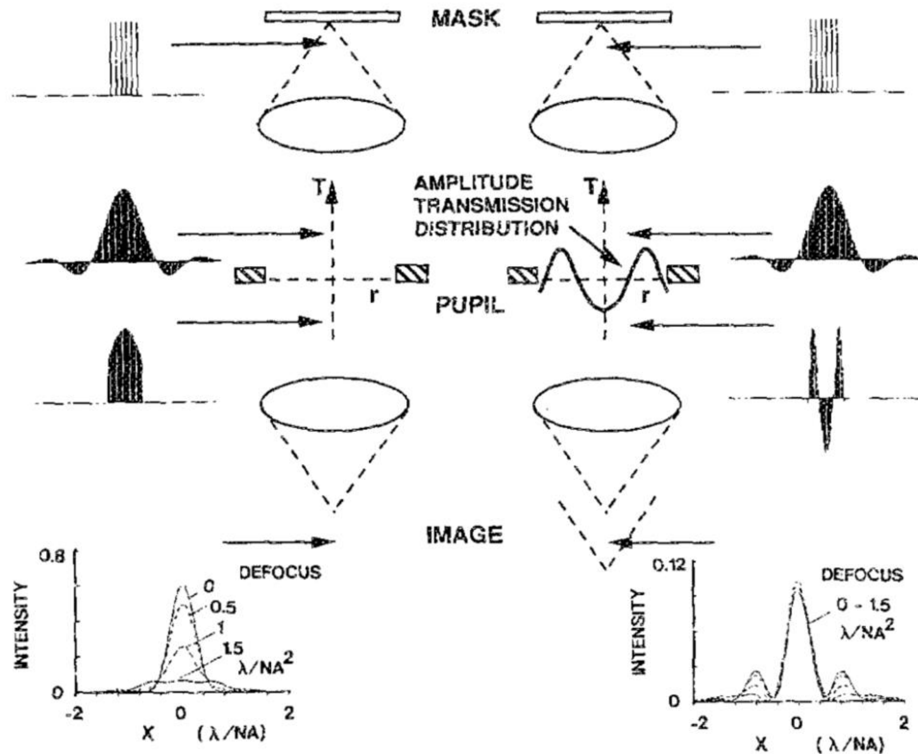

Figure 2.20: Pupil filtering idea. Left: No filter case, right: with filter case [138].

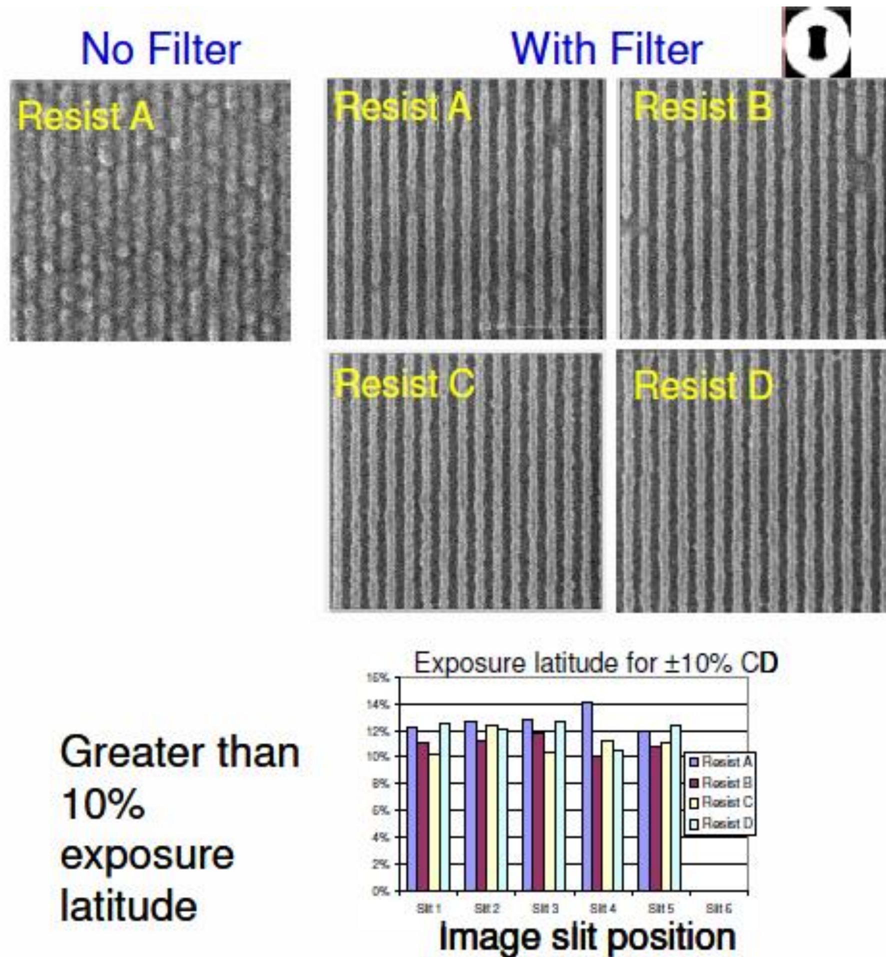

Figure 2.21: Enhancing resolution of EUV ADT tool by using a pupil plane amplitude filter at 22 nm half image pitch for resist A [139].

2.6 Previous Large Field IL Attempts

There have been many attempts to generate large fields with IL. For instance, stitching of periodic submicron fringes by utilizing step-and-align interference has been investigated, where an exposure system was developed to fabricate large area periodic submicron structures by stitching unit exposure area step by step [141].

The quasi-flat-top region of the expanded beam was impingent upon a metal mask with transparent window in the center. The two dimensional dual actuator is capable of

2 nm precision in movement for the stitching. Gratings with 700 nm period were successfully stitched along two directions. However, the linewidths at the overlapping regions have shrunk due to multiple exposures they receive; micrographs of the stitched regions are shown in Fig. 2.22 [141].

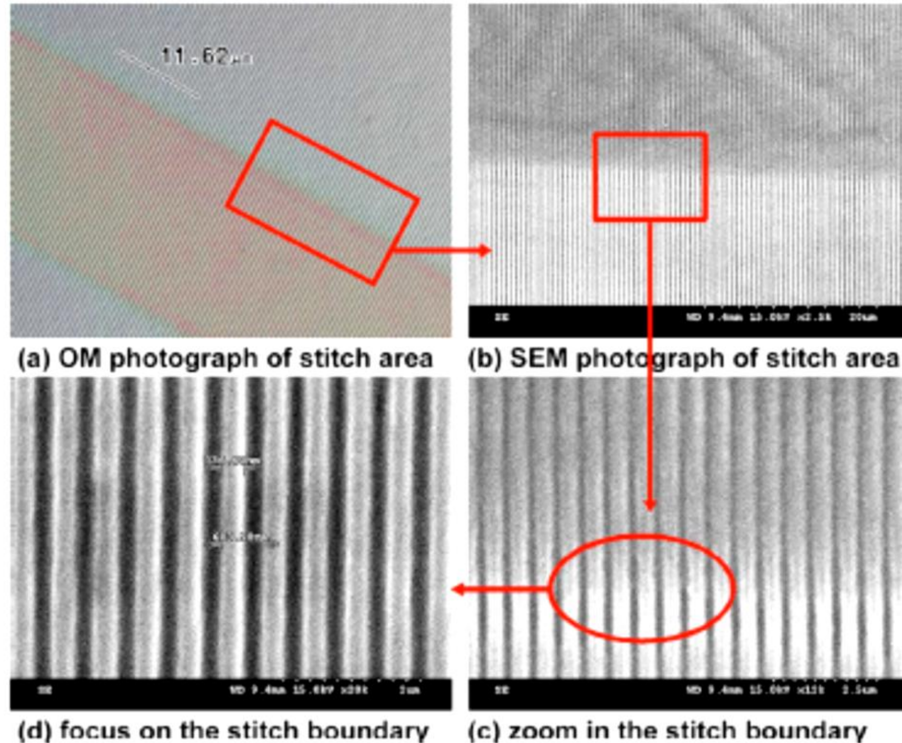

Figure 2.22: Micrographs of stitched areas by optical and scanning electron microscope [141].

Another approach generating large fields using IL is called" "Scanning Beam Interference Lithography (SBIL)", which produces large area periodic patterns by use of phase locked scanning beams [142-144]. Small, mutually coherent breams are phase locked by high-bandwidth electro-optic components and forced to overlap and interfere, generating a small fringe pattern. The image pattern is raster-scanned (either parallel scanning or Doppler scanning) over the substrate by use of a high precision

interferometer-controlled air bearing stage as shown in Fig. 2.23. With SBIL, they were able to achieve resolution down to 200 nm period over large areas [142].

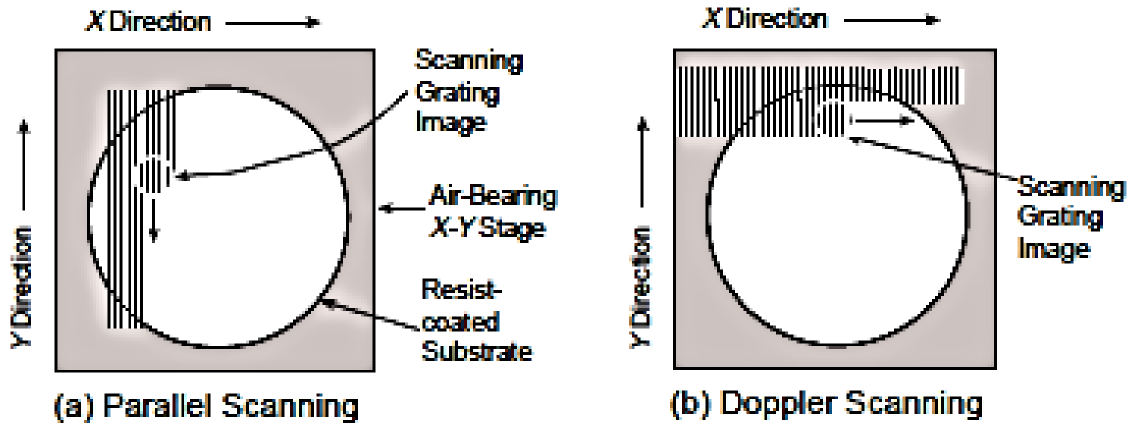

Figure 2.23: (a) Parallel SBIL, (b) Doppler SBIL [142].

Just as for any other scanning lithography system, SBIL requires tightly controlled environmental conditions to minimize disturbant effects coming from vibration, thermal expansion, and air turbulence [142-144].

Some groups worked on achromatic approaches to create large IL defined image fields [88, 145-147]. The need for small bandwith no longer holds true for achiving high resolution with such methods. An example set up is shown in Fig. 2.24. Using this set up, 100 nm period gratings were printed over exposure areas of ≈ 10 cm^2, at the expense of fixed pitch and need for precise gap control [145].

Even though, there have been many attempts to increase the field size defined by interference lithography, it is still unclear how large should the IL field size be. In addition, there haven’t been many attempts to limit the field size based on practical constraints. It is one of the goals of this work to give insight to such considerations.

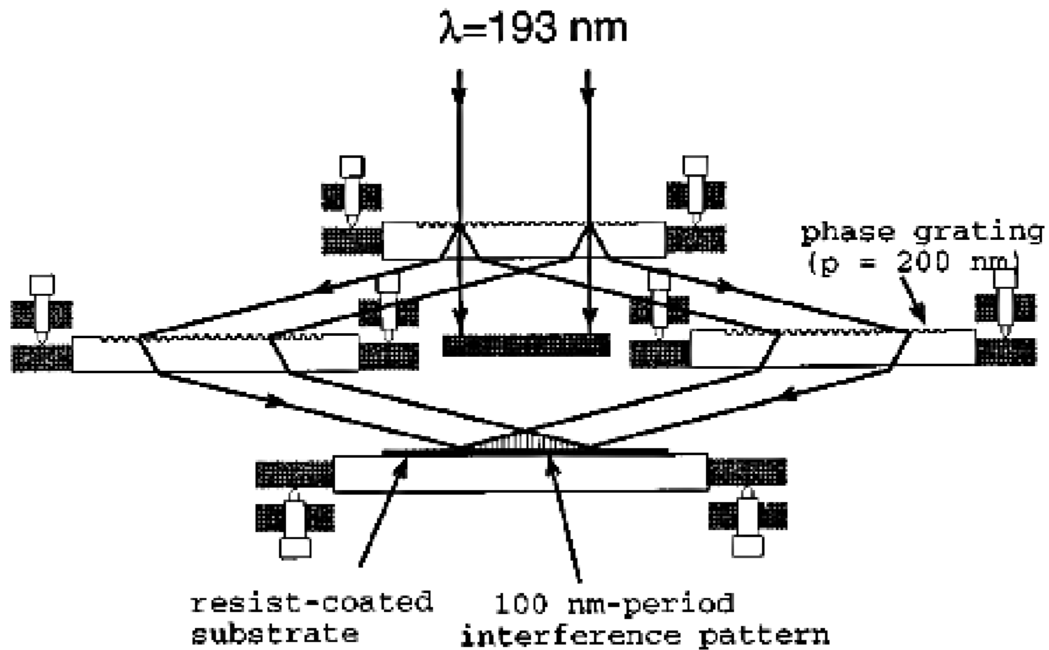

Figure 2.24: Schematic of achromatic IL set up for 100 nm period image pattern [145].

2.7 Translational Image Averaging: Characterization and Measurement

Translational image averaging, which may occur dynamically during imaging, is generally regarded as detrimental. Vibration during patterning is a prime example of such averaging, which is simply the result of dynamic processes that excite structures in an environment and ranges from low to high frequency levels. Relative motion along a beam path can deviate electron beams from their intended projection or cause blurring in imaging, therefore poses a problem [148].

Vibration can be measured by converting translational motion into an electric signal by use of a transducer, such as piezoelectric accelerometer [149, 150]. Its units can be of displacement, velocity or acceleration. Table 2.3 shows comparison of three different techniques to measure vibration and their advantages and drawbacks [150].

Table 2.3: Acceleration measurement methods and properties [150].

Sensor Type	Advantage	Drawback
Piezo-resistive	Measures acceleration	Resistive noise causes limited resolution Good for low and mid frequency bands Supply voltage needed
Electro-dynamic	-	Good for low frequency measurements
Capacitive	Measures acceleration Low cost manufacturing	Fragile Limited resolution

The idea of standardization of vibration criteria for industries such as microelectronics manufacturing and pharmaceutical was presented at SPIE in 1991 by Gordon through use of Vibration Criteria Curves (VCC). They are now widely accepted as a basis to design and continuously monitor the performance of microelectronics manufacturing facilities to ensure minimization of the vibration effects on the operation of most sensitive equipment per each category [151].

The rms velocities of VC curves from A to E are overlaid in Fig. 2.25 for a typical toolset used to fabricate device dimensions between 250 nm and 700 nm. These curves are usually very conservative, meaning that facilities designed for a certain technology node following the VCC approach might still satisfy the requirements for the next technology node. Table 2.4 shows the explanation and applications of the VCC shown in Fig. 2.25. Also shown in that table is the International Standards Organization (ISO) guideline for the effects of vibration on people in different buildings [151].

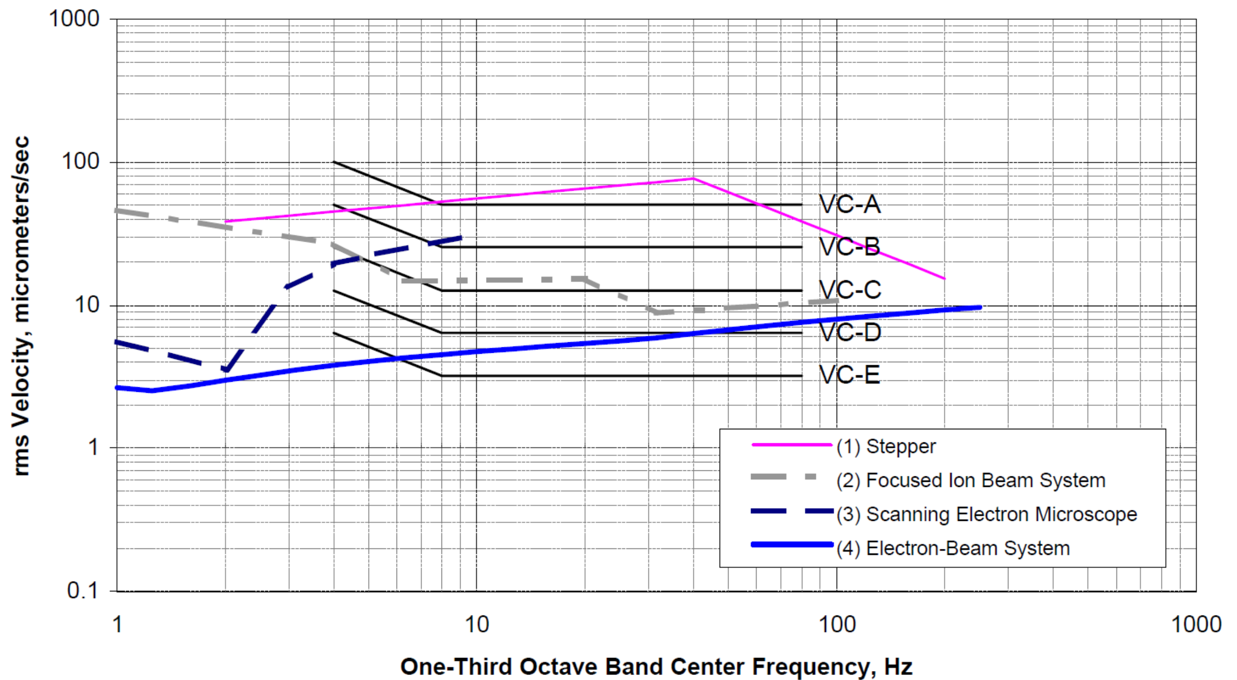

Figure 2.25: Examples of vendor specifications of a typical toolset used in 250 nm to 700 nm fabrication and VC curves from A to E [151].

As it can be seen in Fig. 2.25, vibration criteria curves extend from 4 Hz to 80 Hz, since the equipment at the time the work was published exhibited negligible sensitivity to the lower frequency contributions. However, pneumatic isolation systems such as air springs are being widely used nowadays and they can exhibit resonance frequencies less than 4 Hz. Therefore, there might be a possibility that the operation can be affected from the low frequency range as well. Concerns about frequencies above 80 Hz are assumed to be less significant [151]. Nevertheless, depending on the applications and demands from processes, these requirements need to be updated over time.

Table 2.4: Application and interpretation of the generic VCC as shown in Fig. 2.25 [151].

Criterion Curve	Max Level (1) micrometers per sec, rms	Detail Size (2) microns	Description of Use
Workshop (ISO)	800	N/A	Distinctly feelable vibration. Appropriate to workshops and non-sensitive areas
Office (ISO)	400	N/A	Feelable vibration. Appropriate to offices and non-sensitive areas
Residential Day (ISO)	200	75	Barely feelable vibration. Appropriate to sleep areas in most instances. Probably adequate for computer equipment, probe test equipment, and low power (to 20X) microscopes.
Operating Theatre (ISO)	100	25	Vibration not feelable. Suitable for sensitive sleep areas. Suitable in most instances for microscopes to 100X and for other equipment of low sensitivity.
VC-A	50	8	Adequate in most instances for optical microscopes to 400X, microbalances, optical balances, proximity and projection aligners, etc.
VC-B	25	3	An appropriate standard for optical microscopes to 1000X, inspection and lithography equipment (including steppers) to 3 micron line widths.
VC-C	12.5	1	A good standard for most lithography and inspection equipment to 1 micron detail size.
VC-D	6	0.3	Suitable in most instances for the most demanding equipment including electron microscopes (TEMs and SEMs) and E-Beam systems, operating at their limits.
VC-E	3	0.1	A difficult criterion to achieve in most instances. Assumed to be adequate for the most demanding of sensitive systems including long path, laser-based, small target systems and other systems requiring extraordinary dynamic stability.

Notes for Table 2.4: (1) As measured in one third octave bands of frequency over frequency range 8 to 100 Hz. (2) The detail size refers to the line widths for microelectronics fabrication, the particle (cell) size for medical and pharmaceutical research, etc. The values given take into account the observation that the vibration requirements of many items depend upon the detail size of the process [151].

Adding new tools to a manufacturing site will generally result in increased vibration amplitudes, depending on the quality of noise isolation for the added tools and their accompanying components. Fig. 2.26 shows the example of “before” and “after” environment for both “narrow band” (bandwidth is 0.375 Hz) and one-third octave band spectra (bandwidth is 23 percent of center frequency) [151].

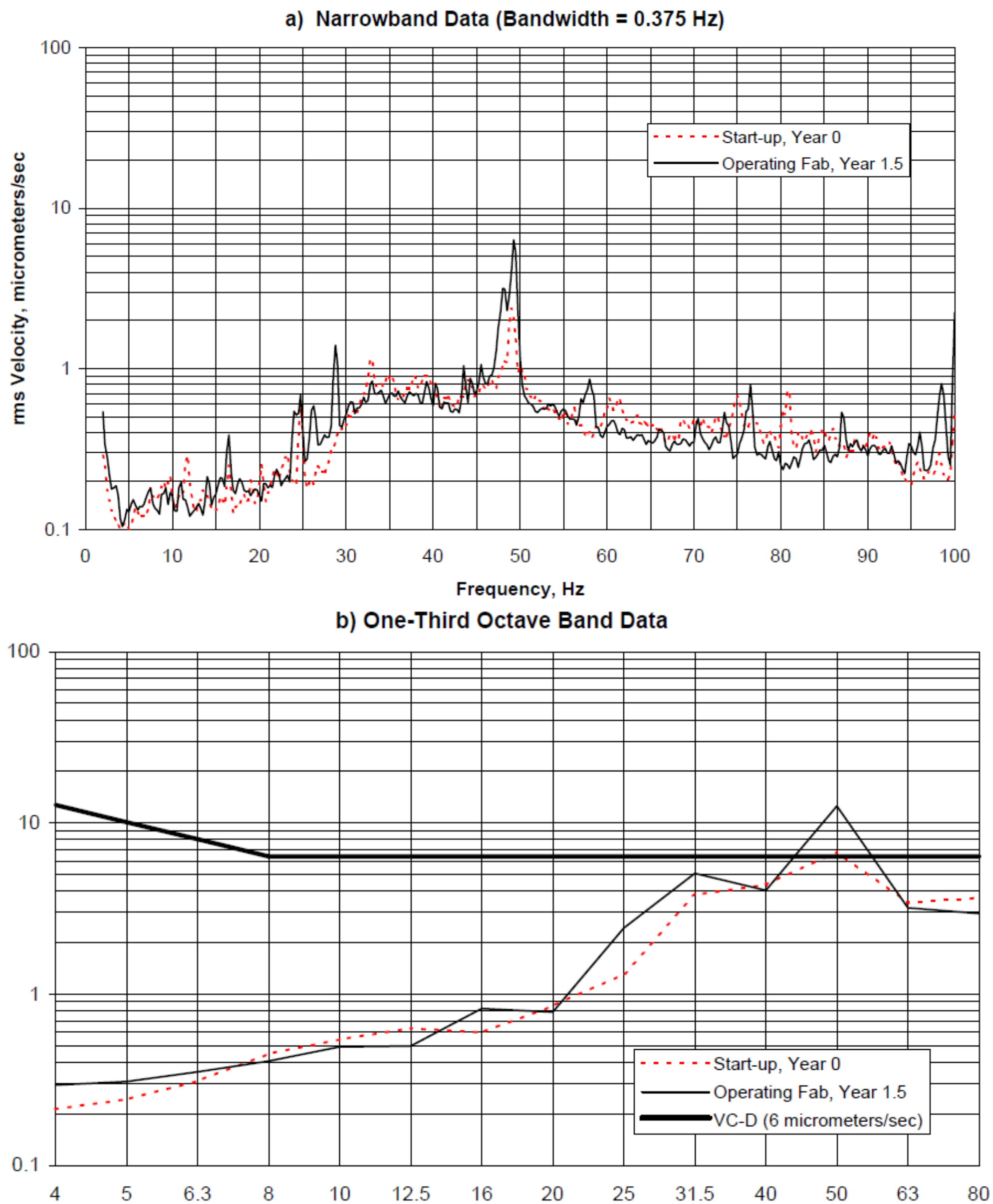

Figure 2.26: Comparison of pre- and post- startup vertical vibration for (a) narrow band data, (b) one third octave data [151].

3. APPROACH AND EXPERIMENTAL PROCEDURE

3.1 IL Specific LER Mitigation Studies

As pointed out in the previous sections, mask roughness is one of the contributors for LER. The roughness of the mask will be translated to the aerial image that will subsequently expose the photoresist. Because interference-like lithography is used to define one directional periodic patterns, mitigation approaches specific to interference-like lithography conditions can be investigated. Two methods are explored in this work. The first one is aerial image averaging via directional translation, and the second one is pupil plane filtering [18].

3.1.1 *Translational image averaging for LER smoothing*

3.1.1.1 Approach

It has been shown that the effect of vibration or any kind of motion results in a shift between the aerial image and the recording plane (i.e. photoresist). The resulting "translated" or "image averaged" profile can easily be calculated as a convolution of the static image (i.e., image in the absence of any vibration) and "time dwelling" histogram function of the translation or vibration [106, 107].

It is important to note that the translation should be applied longitudinally along the lines. Any transverse shift will result in widening of the transition region from low to

high intensity; thereby degrade the contrast and NILS of the image [152], as shown in Fig. 3.1 for a sinusoidal type and uniform type image motion with respect to the resist.

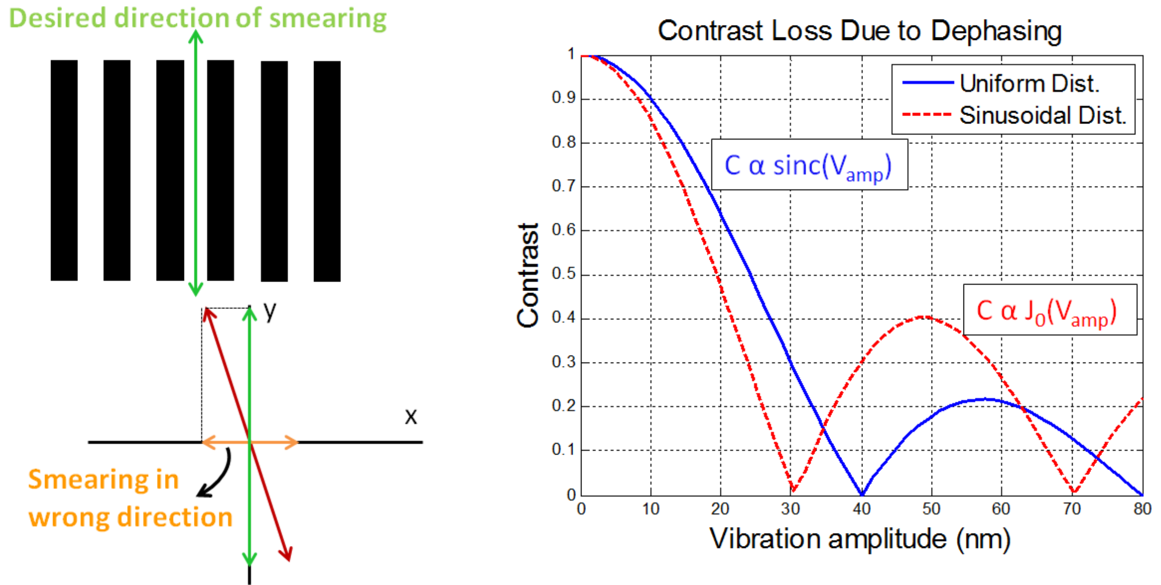

Figure 3.1: Contrast loss due to transverse shift error for uniform and sinusoidal type motions.

Fig. 3.2 (a) shows a rough mask used in the simulations to verify the idea. The roughness period for $Line_1$ and $Line_3$ is 500 nm and the roughness is random for $Line_2$. The corresponding single pass exposure top-down aerial image calculated with KLA-Tencor PROLITH™ [153] (in vector image mode) is shown in Fig. 3.2 (b). Significant non-uniformity in the intensity distribution of the lines is evident. If the exposure is split into two passes and a translational shift of 250 nm was applied along the lines, the resulting aerial image intensity is much more uniform as shown in Fig. 3.2 (c). Therefore, even though the ideal situation would be a continuous translation between the aerial image and the recording medium during exposure; image averaging can also be applied

by splitting a single pass in to multi-pass exposures and apply a directional shift along the lines between the passes.

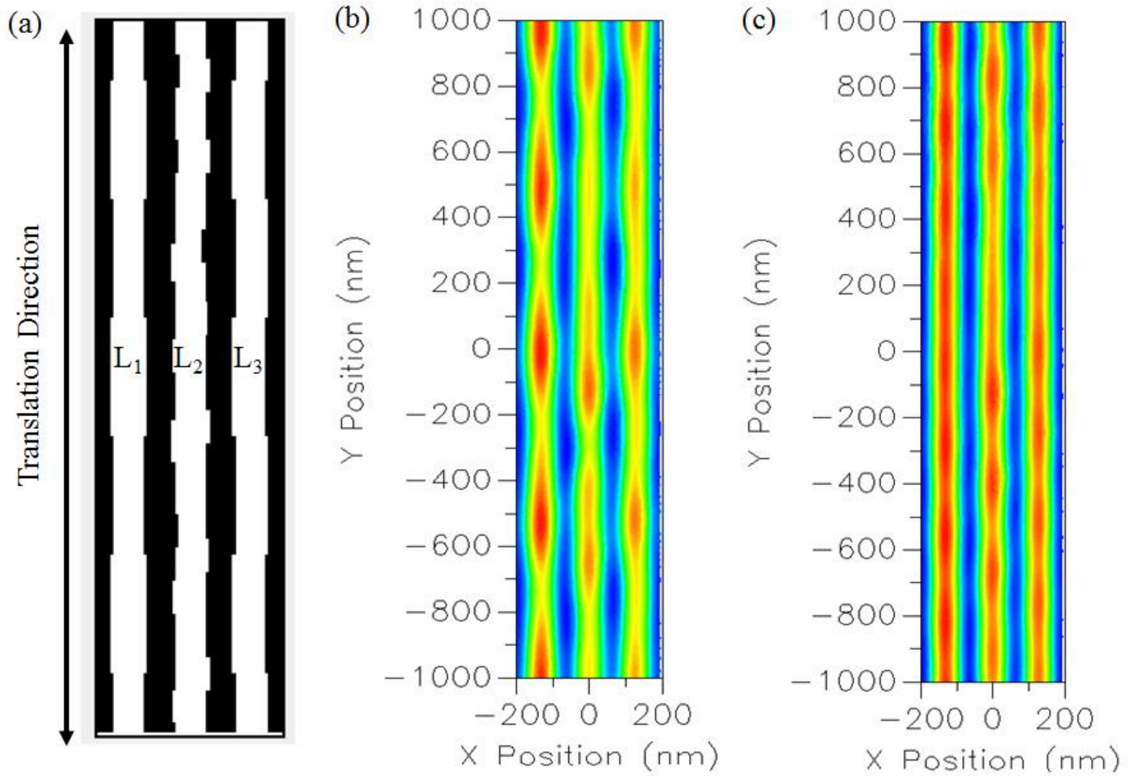

Figure 3.2: (a) Mask with anti-correlated (L_1), random (L_2), and perfectly correlated (L_3) rough lines. (b) Aerial image from single pass exposure. (c) Aerial image from double pass exposure. Simulations performed with KLA-Tencor PROLITH^{TM}.

3.1.1.2 Experimental procedure

The experiments for this part of the work were done on both a KrF (248 nm) interference lithography set up and on a commercial ArF (193 nm) scanner. In the interference imaging set up, the aerial image averaging via directional translation along the lines was achieved by use of fused silica wedges. The apex angle of the wedge prisms was 1.05°, resulting in a deviation of 0.55° for a normally incident 248 nm beam [18].

Fig. 3.3 (a) shows the basic interference lithography set up used for image averaging experiments. The KrF laser utilized in the experiments was a line narrowed ELS 4600 laser with a bandwidth of 0.7 pm. In order to reduce the damaging effect of the high laser beam power on optical components, the beam was bounced back and forth between a couple of silicon mirrors. Beam homogenization was performed by spatial filtering just before the phase shifting mask (with 600 nm pitch) that was used as a beam splitter. The beam splitter diffracted the homogenized beam into many orders. The zero order was blocked in the system and the first diffraction orders were collected by use of high quality aluminum enhanced UV mirrors to be directed towards the wafer plane to interfere. The wedges were placed between the wafer plane and the mirrors, and shifted at mid exposure in x direction to achieve image translation in y direction (i.e., along the lines) as shown in Fig. 3.3 (b) [18]. The applied shifts were 250 nm, 500 nm and 750 nm.

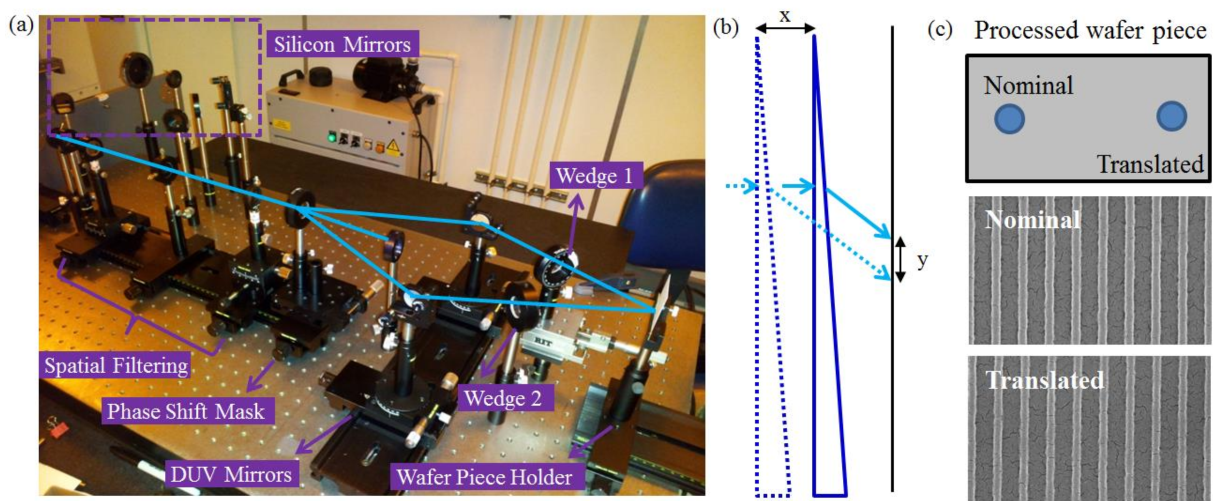

Figure 3.3: (a) Interference lithography set up for the aerial image averaging experiments [18]. (b) Translation approach: the wedge is moved in x direction at mid exposure, resulting in shift of the image in y direction (along the lines). (c) Co-processed nominal and translated dies on the same wafer piece to minimize processing related variations.

The set up shown in Fig. 3.3 is widely known as the reduction Talbot IL configuration. Unlike achromatic approaches, it has the capability of NA adjustment by rotating the two mirrors used to collect the first order diffractions. In order to alleviate the alignment difficulties the mirrors were not tilted, resulting in 300 nm pattern pitch at the wafer plane. Furthermore, the nominal and image averaged dies were processed on same wafer piece as shown in Fig. 3.3 (c) to minimize processing related variability [18].

The silicon wafers were initially dehydration baked at 200°C for 2 minutes. After cooling, AZ KrF 17B-100 BARC was coated at 3000 rpm, resulting in less than 2% reflectivity at the photoresist/BARC interface. The BARC was baked at 200°C for 90 seconds. Subsequently, JSR ARX 2928 JN-7 photoresist was spin coated at 2500 rpm resulting in 70-75 nm thick film and baked at 110°C for 90 seconds. Post exposure bake was performed at 110°C for 60 seconds. The development was performed in CD26 TMAH developer solution for 30 seconds followed by 30 seconds deionized water rinse. Finally a hard bake was performed at 120°C for 60 seconds.

Following the resist processing, SEM images of nominal and image averaged cases were taken at 42kX magnification by the SEM/FIB Zeiss-Auriga located at University of Rochester. This magnification ensured capturing of lines longer than 2μm with a wide field of view. LER analysis was done on the SEM images through SuMMIT software [154] (an SEM image analysis tool from EUV Technology Corporation). The results were averaged over 24 lines at around the die field center. Appendix B gives a sample LER processing routine created in MATLAB [155] that can be customized and used to calculate the roughness of a single edge. This routine was validated by comparing

the calculated 3σ LER values to the SuMMIT outputs. The results will have some variations depending on the selected parameters to smoothen the line on the SEM images, quality of the images and also on the line segment length [18].

A commercial 193 nm scanner was utilized in the projection lithography version of the aerial image averaging experiments. To apply the image averaging, exposures were divided into two or three passes and some amount of shift was applied along the line space direction. The NA of the objective lens was 0.93 NA, which resulted in 9.3/µm cut off frequency for the mask roughness transfer, under these experimental illumination conditions. The mask used in the experiments had dense line space features at 130 nm and 150 nm pitch, and semi-dense periodic features at 140 nm pitch. The film stack was 120 nm thick photoresist coated on 85 nm ArF bottom anti-reflective coating (BARC). Under these conditions an exposure module of 8 dies (shown in Fig. 3.4) was exposed with 6 repetitions across the wafer [18].

The first die corresponds to the single pass, nominal case. The second die has two passes, with no shift between them. Its purpose was to serve as an indicator of the alignment error between the superimposed passes. Dies 3, 4, 5 and 6 all have 2 passes; where the second pass was shifted 600 nm, 500 nm, 400 nm, and 300 nm with respect to the first pass. Dies 7 and 8 have 3 passes, where the second pass was shifted 300 nm with respect to the first one for both, however the shifts between the third and the first passes were 100 nm and 200 nm, respectively. It should be noted here that, a large amount of shift divided into many passes (with no alignment error) would be a more ideal case [18].

After the exposure and processing, CD-SEM was utilized to capture SEM images with 3 μm long resist lines. SEM images were processed using SuMMIT in batch mode with a calibrated recipe for the process [18].

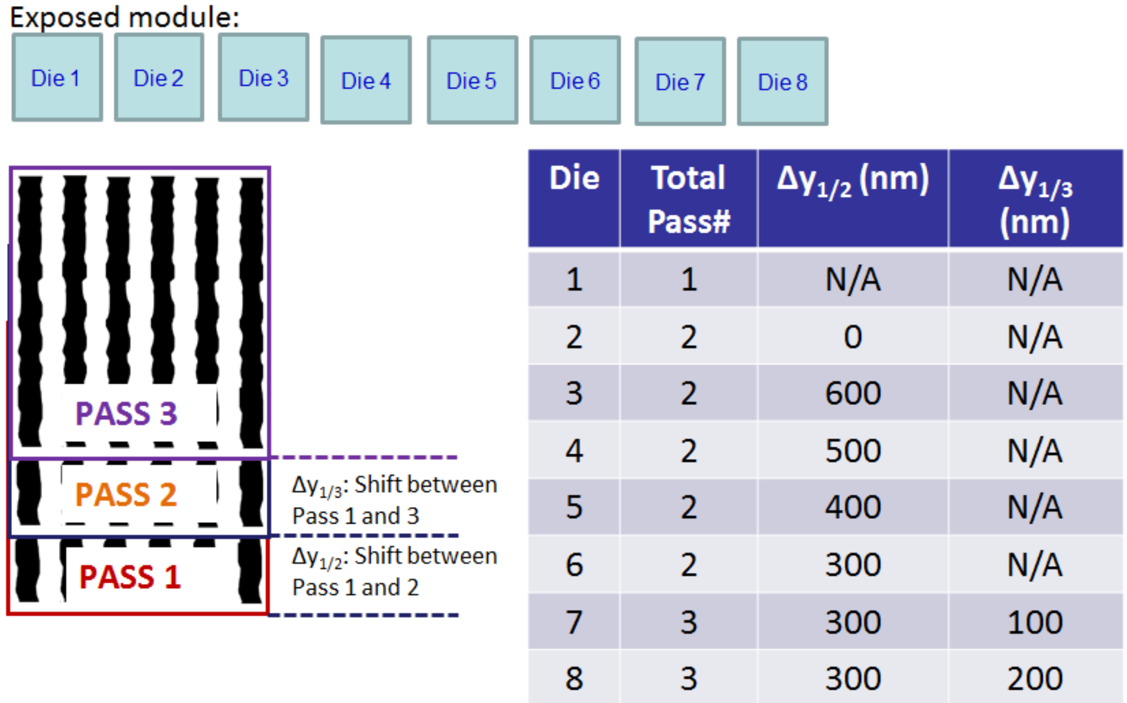

Die	Total Pass#	$\Delta y_{1/2}$ (nm)	$\Delta y_{1/3}$ (nm)
1	1	N/A	N/A
2	2	0	N/A
3	2	600	N/A
4	2	500	N/A
5	2	400	N/A
6	2	300	N/A
7	3	300	100
8	3	300	200

Figure 3.4: Exposed module on the scanner and imaging conditions for each die [18].

3.1.2 *Pupil plane filtering*

3.1.2.1 Approach

An ideal 1D mask with vertical line space features illuminated with coherent light will have diffraction orders lying along the x-axis of the pupil plane, as shown in Fig. 3.5 (a). For the sake of discussion, the objective lens is large enough to collect the zeroth and the first order diffractions to create the aerial image. However, the mask absorber is not perfect and exhibits sidewall roughness. This roughness will result in additional diffraction orders in perpendicular direction to the main diffraction orders

coming from the ideal pattern, as shown in Fig. 3.5 (b). As mentioned in the theory section, these roughness orders will be collected by the objective lens in addition to the main diffraction orders, as long as their frequency is less than a cut off frequency dependent on the experimental factors such as the illumination source shape, the wavelength, and the numerical aperture of the system. Fig. 3.6 (a) shows the nominal case photoresist profile resulting from a constant threshold resist model and using the rough mask shown in Fig. 3.5 (b). The roughness present on the pattern is correlated to the mask roughness. For the interference-like lithography conditions, the small partial coherence of the illumination source allows some seperation between the main and roughness diffraction orders. Using this property, a transmission filter can be inserted at the pupil plane to block unwanted diffraction orders. The resulting photoresist profile exhibits much less roughness, as shown in Fig. 3.6 (b) [19].

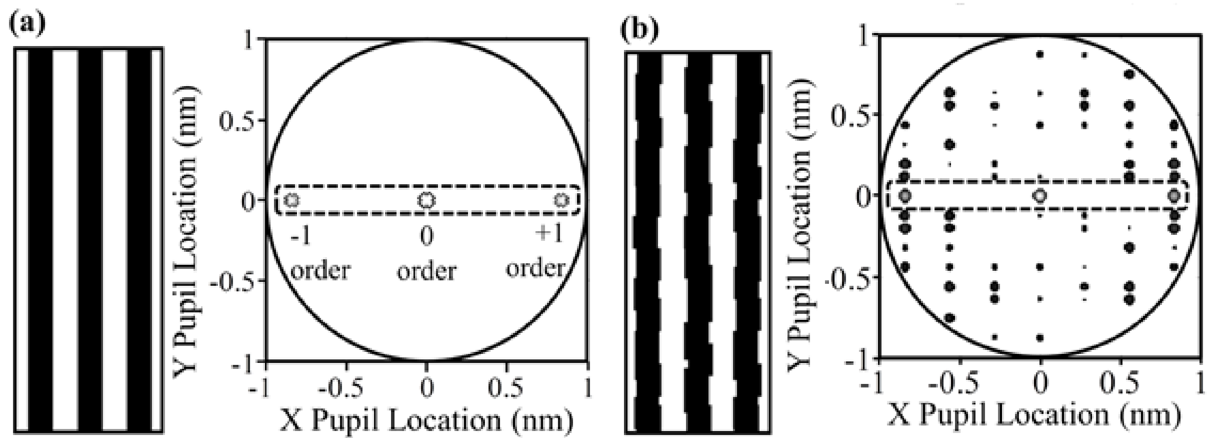

Figure 3.5: (a) 1D mask with smooth vertical line space features and corresponding diffraction information. (b) Mask with absorber roughness and corresponding diffraction information. Dashed regions: main diffraction orders coming from smooth vertical features [19].

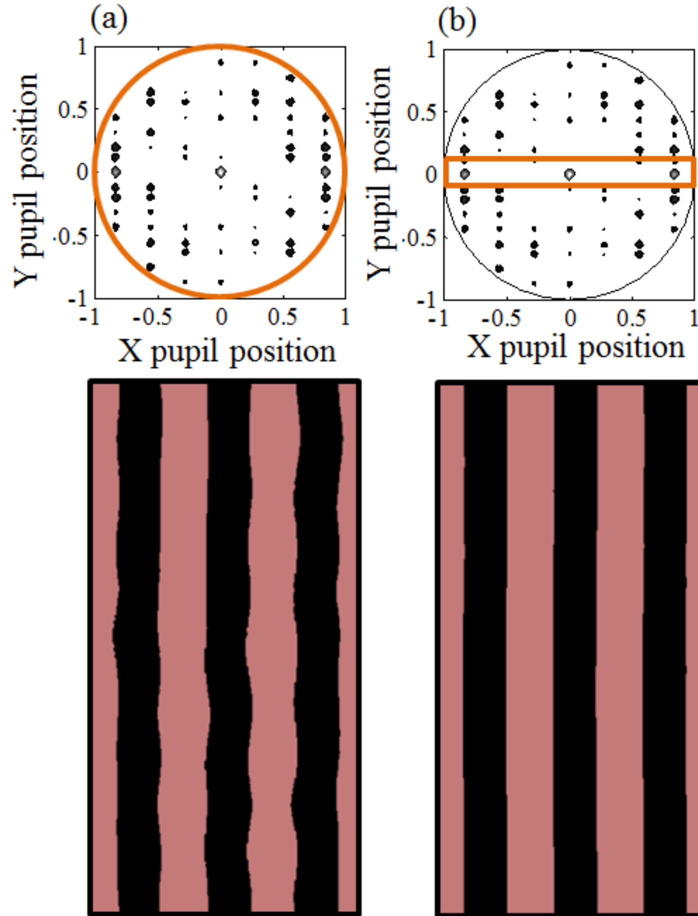

Figure 3.6: Collection of (a) many diffraction orders or (b) just the main diffraction orders at the pupil plane. Top down views of photoresist profiles generated with a constant threshold resist model are shown for each case [19].

Historically, photolithographic tools do not posses the amplitude (i.e., transmission) filtering capability due to the fact that it decreases the available intensity that would otherwise be utilized in exposing the photoresist. But, phase filtering capability is already avaible on some commercial scanners, such as ASML's high resolution wavefront manipulator called "FlexWAVE" [156], shown in Fig. 3.7. Because of this, the experiments in this work were performed by using phase filtering approach instead of transmission filtering.

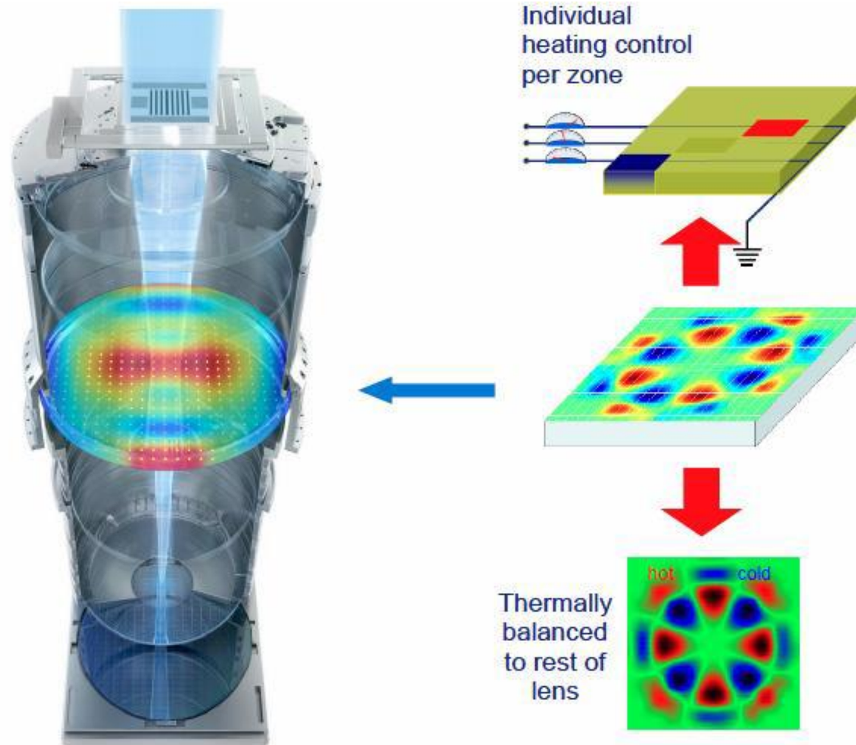

Figure 3.7: ASML's FexWave wavefront manipulator [156].

In order to come up with an optimum wavefront shape for the phase filter, an aerial image simulation study was performed using a programmed roughness mask in PROLITH™ (in vector imaging mode). Fig. 3.8 (a) shows the programmed defect on one directional line/space pattern and the two cutline locations where the CD was measured on the aerial image. The illumination source was the optimized dipole shown in Fig. 3.8 (b) and the CD difference (i.e., ΔCD) between CL_1 and CL_2 was used as the roughness transfer indicator. The effect of different types of aberrations on ΔCD was shown in Fig. 3.8 (c). The coefficient of Z_5 and Z_6 were selected as 0.2 waves and the phase difference between the orange and blue sections of the "step" wavefront signature was 0.2 waves. It is easily seen that the "step" wavefront shape results in minimum ΔCD (i.e., 3.2 nm compared to 8.9 nm). Even though astigmatism-x (Z_5) results in some

reduction of ΔCD, there is also degradation in NILS due to the overlap between the main diffraction orders and the aberrations [18, 19].

Therefore, the selected phase filter wavefront should have astigmatism-like shape and introduce some amount of phase difference between the roughness orders and main diffraction orders at the pupil plane. That way, at the best focus of the main diffraction orders, the roughness information will be defocused and the mask roughness transfer will be degraded [19].

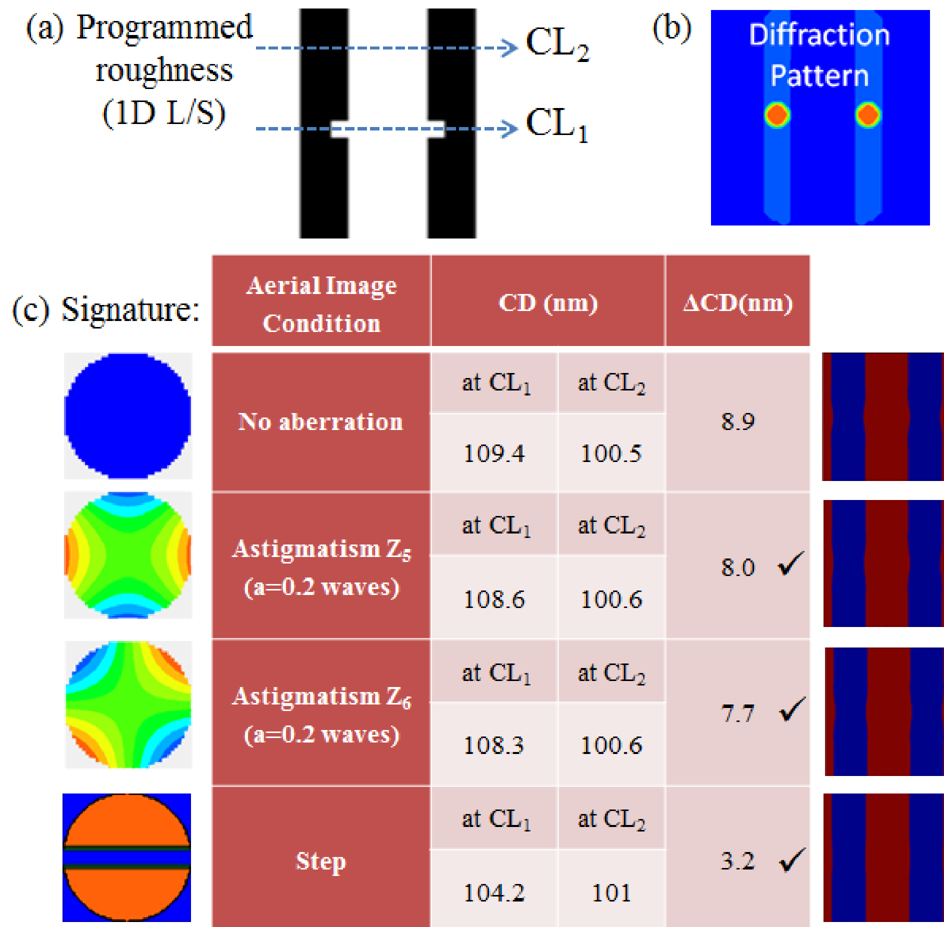

Aerial Image Condition	CD (nm)		ΔCD(nm)
	at CL_1	at CL_2	
No aberration	109.4	100.5	8.9
Astigmatism Z_5 (a=0.2 waves)	108.6	100.6	8.0 ✓
Astigmatism Z_6 (a=0.2 waves)	108.3	100.6	7.7 ✓
Step	104.2	101	3.2 ✓

Figure 3.8: (a) Programmed defect mask and the measurement locations along two cutlines. (b) Diffraction pattern of the mask with optimized dipole. (c) Effect of different aberrations on the aerial image profile and ΔCD along two cut locations.

In order to find the optimum amount of phase shift between the main and the roughness diffraction orders, a simulation study was performed using the anti-correlated roughness mask shown in Fig. 3.9 (b). The corresponding smooth mask and roughness mask programmed in correlated fashion are also given in Figures 3.9 (a) and (c) for comparison. The period and amplitude of the roughness are denoted as “P” and “A”. For the simulations, main feature (i.e., vertical) pitch was fixed at 128 nm and the roughness amplitude was fixed at 2 nm per edge. The roughness period was changed from 200 nm up to 700 nm, and the inserted phase difference between roughness and main orders were varied from 0 waves (nominal case) up to 0.3 waves. The ArF illumination source shape was an optimized dipole-X with σ=0.1. The roughness transfer at the programmed roughness period (i.e., ΔCD) was plotted against the phase difference in Fig. 3.10 (a). At 0.25 waves, the transfer of the programmed roughness was eliminated.

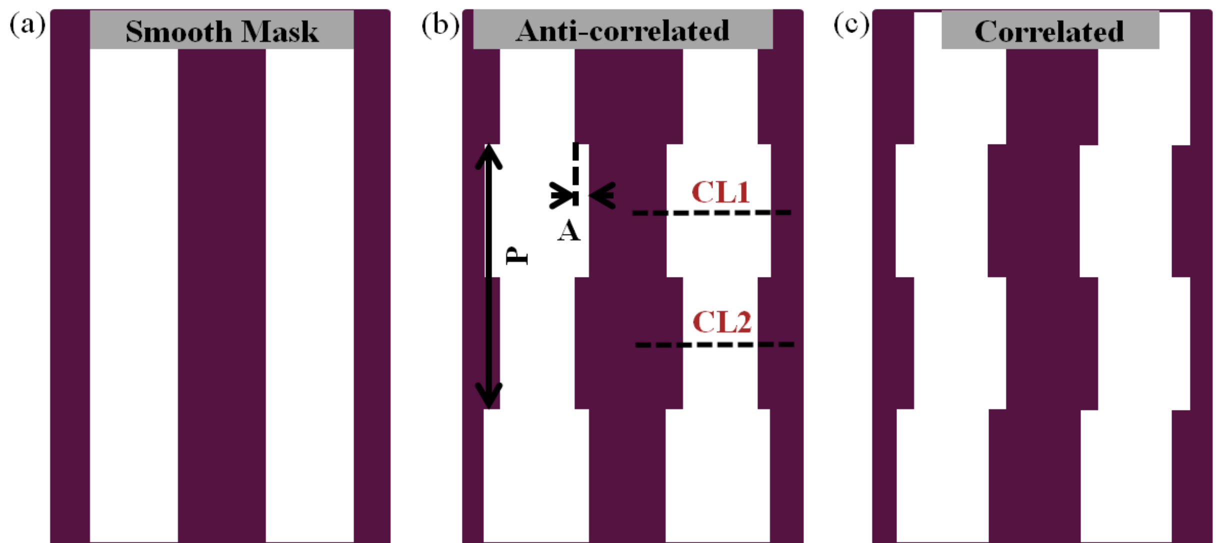

Figure 3.9: (a) Definition of an ideal (smooth) mask with vertical line space pattern, and corresponding (b) anti-correlated and (c) correlated programmed roughness masks [19].

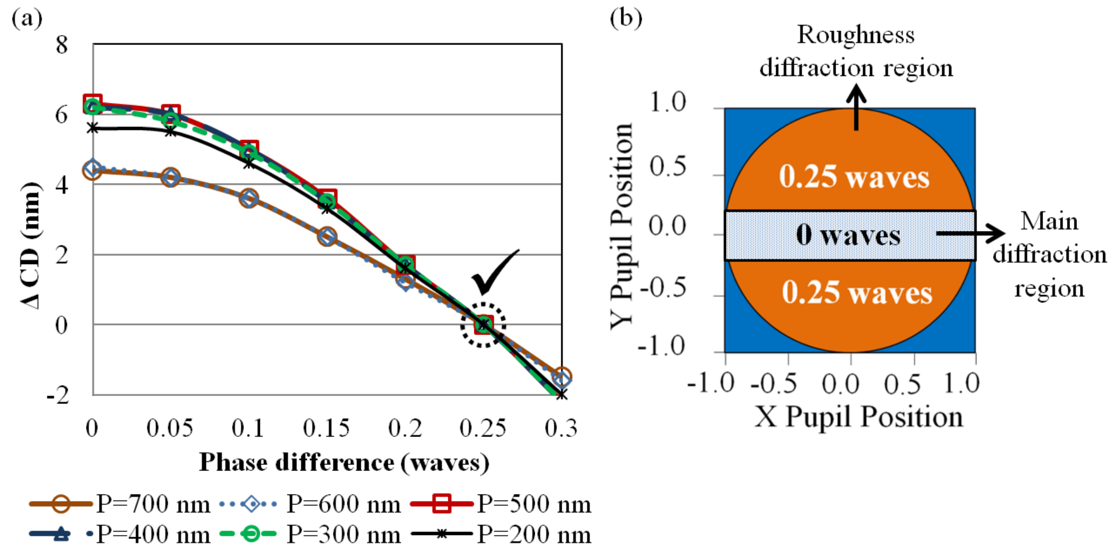

Figure 3.10: (a) Roughness transfer as a function of introduced defocus. (b) Optimized pupil plane phase filter for vertical line space patterns.

Therefore, the ideal phase filter for one directional vertical periodic features will look like in Fig. 3.10 (b), which will introduce a quarter wave phase difference between the main and roughness diffraction orders to force the latter be defocused at the best focus of main vertical features [19].

The transferred roughness from the mask can come from a broadband of frequencies. Therefore, it is beneficial to observe the effect of ideal phase filter on a white noise mask. Fig. 3.11 (a) and (b) show a white noise mask generated using SuMMIT and its corresponding diffraction information at the pupil plane for an optimized dipole. The mask roughness frequencies interacting with the orange sections of the phase filter (shown in Fig. 3.10 (b)) are out of focus at the aerial image. When the nominal and phase filtered aerial images shown in Fig. 3.11 (c) and (d) are compared, the

latter has more uniform intensity distribution. The 3σ LER for the nominal and phase filtered cases are 2.47 nm and 0.64 nm, respectively.

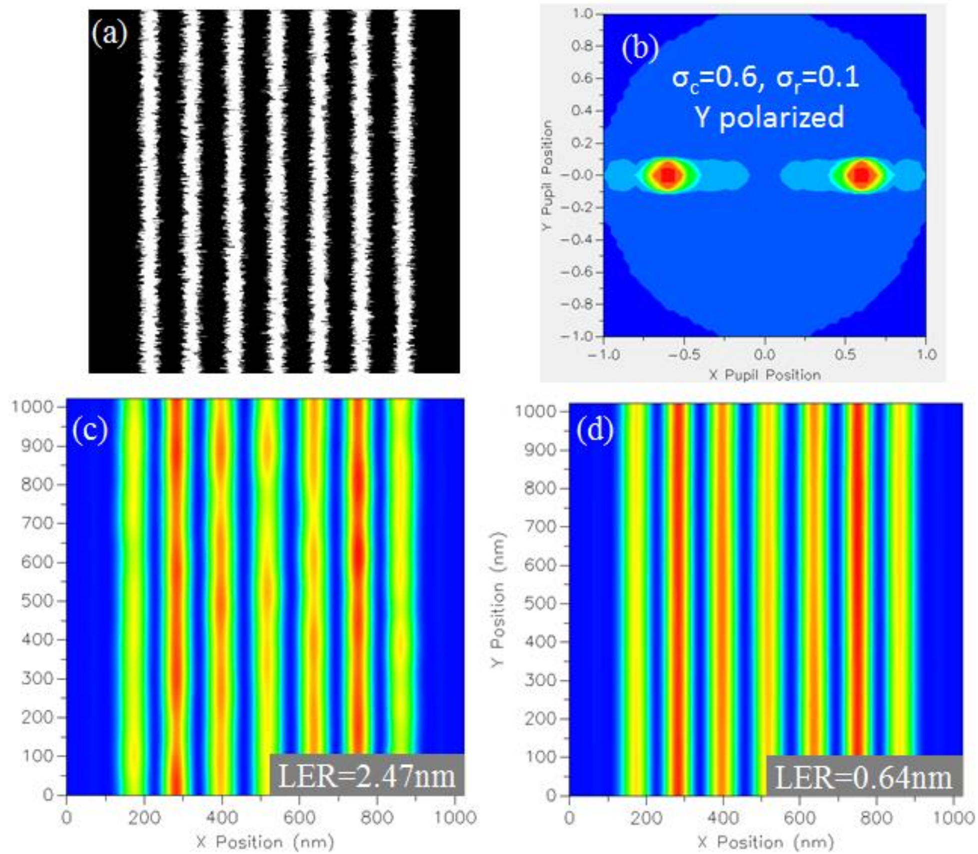

Figure 3.11: (a) White noise mask. (b) Diffraction information at the pupil plane with optimized dipole illumination. Resulting aerial images for the (c) nominal case, (d) phase filtered case.

The top-down views of nominal aerial image intensity distributions for the anti-correlated and correlated masks with roughness period of 250 nm programmed on 128 nm vertical pattern pitch are shown in Fig. 3.12 (a). Fig. 3.12 (b) shows the top-down view of the common filtered aerial image distribution when the optimized phase filter is inserted at the pupil plane. The comparison of aerial image intensities along

CL1 and CL2 are given in Fig. 3.12 (c). The CL1 and CL2 distributions for phase filtered cases are identical, thereby on top of each other.

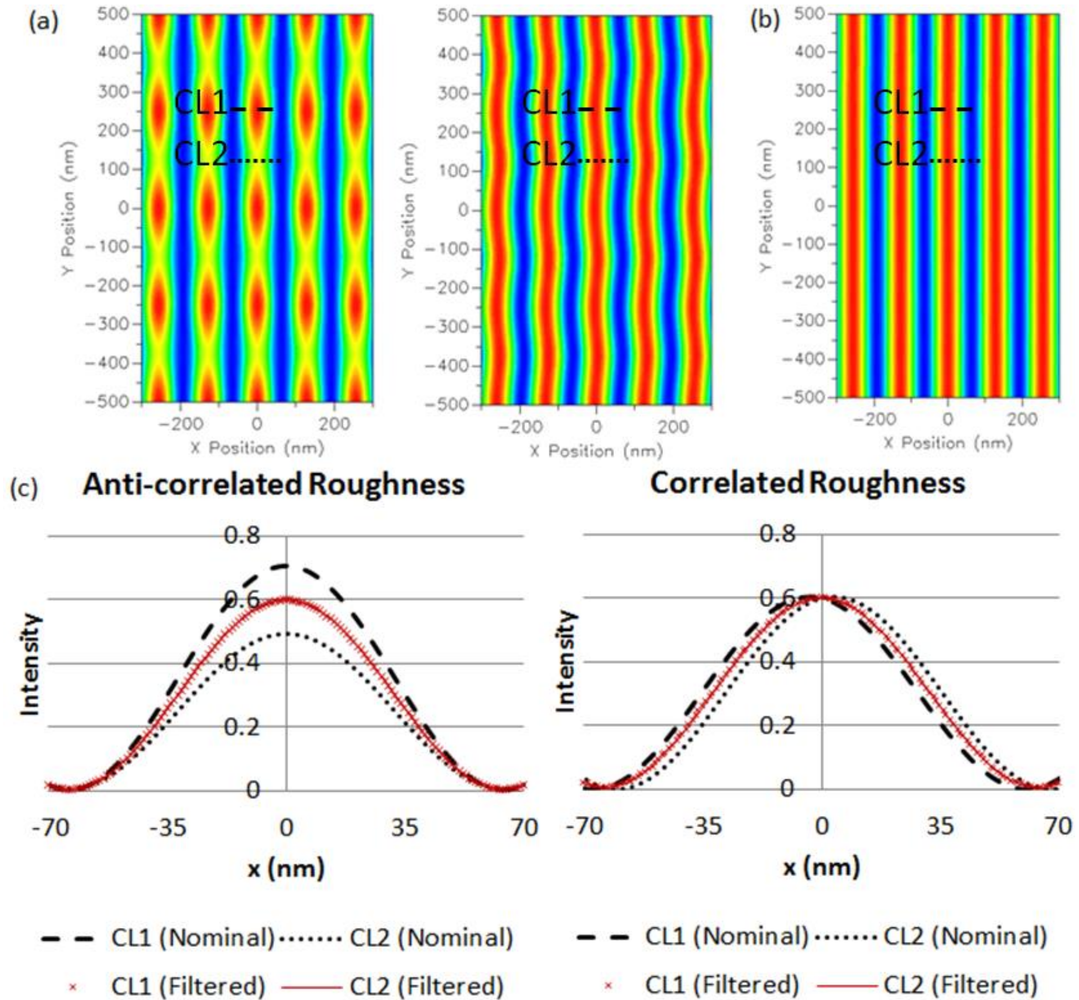

Figure 3.12: (a) Top-down aerial image intensity distribution for nominal anti-correlated and correlated masks. (b) Corresponding phase filtered distribution. (c) Comparison of intensity distributions along the cutlines.

A final set of simulations were performed on the anti-correlated roughness mask and the smooth mask to observe the through focus and exposure dose behavior with and without the phase filtering for 250 nm roughness period. The focus was varied

from -0.3 μm to 0.3 μm and three aerial image thresholds were used (0.25, 0.30 and 0.35). Bossung curves were evaluated for both smooth mask and roughness mask at CL1 and CL2. Fig. 3.13 (a) shows these Bossung curves with and without the phase filter. For the nominal case, the CD values at vertical feature best focus is different between the smooth and rough masks. However, at the presence of the phase filter, the CD values are identical. As a side effect due to phase filtering, there is also a tilt to the curves. The filter induced roughness mitigation is more evident in Fig. 3.13 (b), where ΔCD goes to 0 nm at the vertical feature best focus for the phase filtered case, independent of the exposure dose.

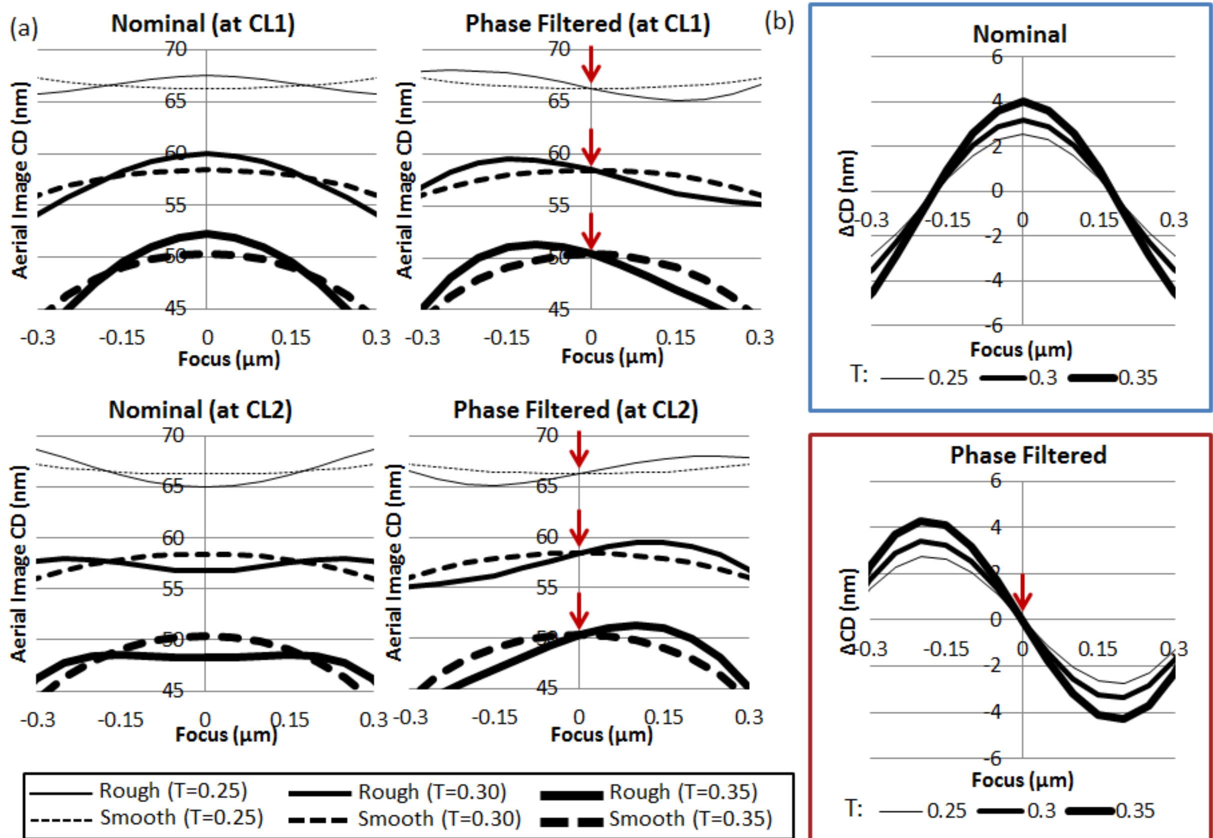

Figure 3.13: (a) Aerial image Bossung curves for nominal and phase filtered cases at two cutlines, (b) ΔCD between the two cutlines for nominal and phase filtered cases. "Nominal" refers to without the filter case.

This focus dependence behavior was validated by performing simulations at various roughness frequencies, yielding similar results. Experimental results were expected to follow these simulated trends, therefore, further experiments with a large focus range were not pursued in this study.

3.1.2.2 Experimental procedure

For the experiments, a 6% attenuated phase shift mask with dense (i.e., 1:1 duty ratio) vertical line space patterns was utilized. On the mask, the roughness features were programmed on the edges of 64 nm line/space features in both correlated and anti-correlated fashions. The scanner was ASML:NXT1950i equipped with FlexWAVE wavefront manipulator located at Imec, in Leuven, Belgium. The objective lens NA was 1.35 and the 193 nm illumination source was dipole-X with σ_{in}/σ_{out} of 0.55/0.65. The roughness periods that were investigated are 200 nm and 500 nm, and the amplitudes were changing from 0 nm up to 9 nm per edge. The diffraction information for these roughness periods with the optimized dipole are shown in Fig. 3.14 [19].

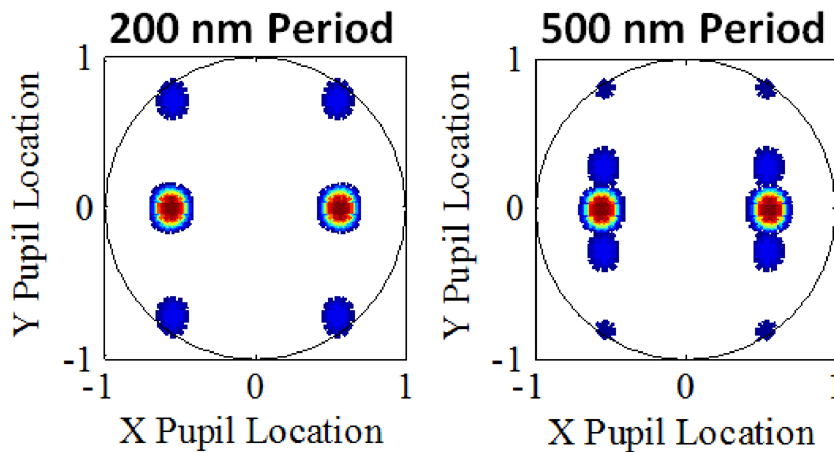

Figure 3.14: Diffraction information for 200 nm and 500 nm roughness periods.

Initially, the phase filter wavefronts for the two roughness frequencies were created using a MATLAB and PROLITH™ co-optimization routine (a modified version from [157]) that minimized the ΔCD at two extreme cutline locations on the aerial image. In the optimization routine, only astigmatism-y aberrations were utilized to save the computation time. The resulting optimized wavefronts for 200 nm and 500 nm roughness periods are shown in Fig. 3.15 as W1 and W2 with corresponding Zernike combinations to create them. However, some combinations of Zernike coefficients (such as W1 and W2) each in the order of 0.2 waves did not pass the safety thresholds of the scanner. Therefore, the following approach was utilized instead.

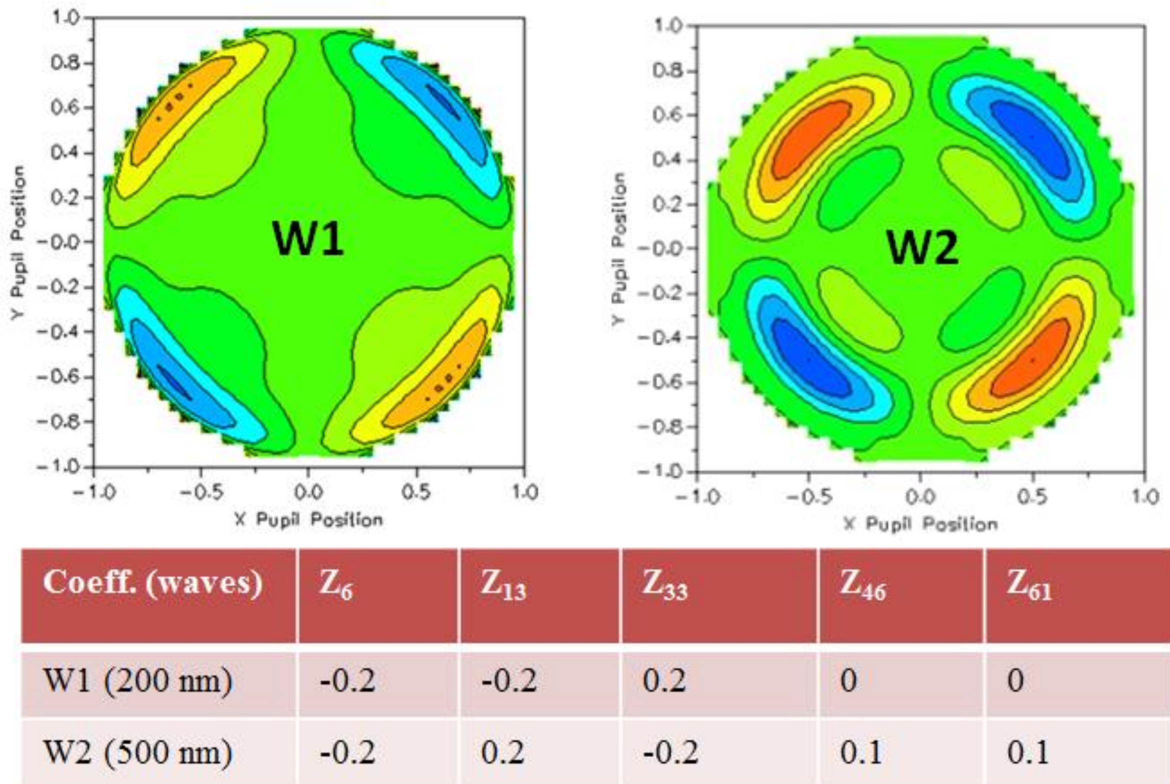

Coeff. (waves)	Z_6	Z_{13}	Z_{33}	Z_{46}	Z_{61}
W1 (200 nm)	-0.2	-0.2	0.2	0	0
W2 (500 nm)	-0.2	0.2	-0.2	0.1	0.1

Figure 3.15: Optimization of phase filters for 200 nm (W1) and 500 nm (W2) roughness periods and corresponding Zernike combinations to create them.

As explained in Fig. 3. 10, the ideal phase filter should introduce a quarter wave phase difference at the pupil plane between the main feature and roughness diffraction orders. Therefore, for a given illumination condition and a programmed roughness mask, the ideal phase filter can easily be created. Once the wavefront filter shape is known, a surface fitting routine can be programmed in MATLAB to calculate the coefficients of Zernike terms to generate the desired phase filter. The schematic flow of such a routine created for this work is given in Fig. 3.16 (a), and the detailed flow is included in Appendix C. As an example, a known target filter was realized in PROLITH^{TM} with more than 10 Zernike coefficients. The program successfully calculated the Zernike combination that was input to PROLITH^{TM} and outputted the wavefront shape created using that "best-fit" combination.

(a) MATLAB Fitting Routine:

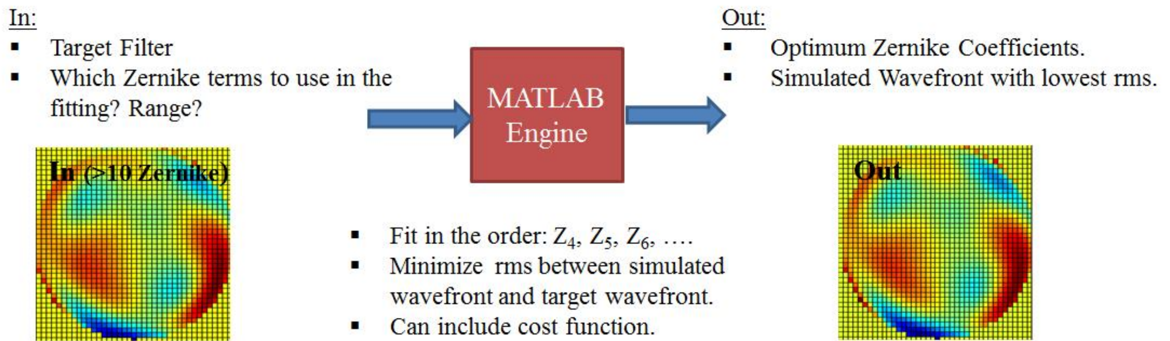

(b) Effect of including cost function:

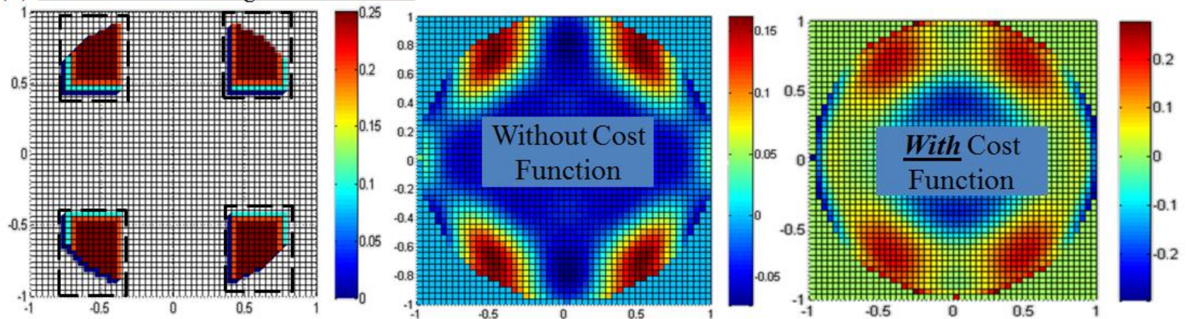

Figure 3.16: (a) MATLAB surface fitting routine. (b) Effect of cost function inclusion on the fit efficiency.

The user can define the Zernikes to be included in the surface fitting optimization. The code generates a synthetic wavefront using the user selected Zernike combination and compares it to the target wavefront which is input to the program. The Zernike coefficient combination that gives the minimum root mean square (rms) error and the best surface fit are outputted. User can also include a cost function to improve the fit at certain parts of the pupil plane. For example, in Fig. 3.16 (b), the four dashed boxes are defining the pupil locations where the rms error is desired to be minimized. Looking at the plot scales, it is easily seen that using the cost function significantly improves the fit at the desired locations.

For this study, the target roughness period for mitigation was selected as 200 nm. The optimum Zernike combination to create that wavefront was found by the custom surface fitting code described above. Fig. 3.17 (a) shows the target phase filter and the experimentally generated FlexWAVE filter. The coefficients of Z_4 through Z_{37} used to create the target filter and the experimental filter are shown in Fig. 3.17 (b). This approach required combinations of Zernike coefficients each less than 0.2 milliwaves.

In the ASML scanner, a focus-exposure-matrix (FEM) was created where the exposure dose was varied between 18.5 and 25.5 mJ/cm^2 with increments of 0.5 mJ/cm^2 and the focus was varied between -40 nm and +40 nm with increments of 10 nm. Two wafers were exposed with this FEM, one with the FlexWAVE generated phase filter and one without it. The film stack was 105 nm JSR AIM5484 photoresist coated over 95 nm ArF BARC (Brewer Nissan ARC29). Following exposures and processing, SEM images were captured by Hitachi CG5000 with pixel sizes of 0.879 nm by 5.38 nm in X and Y directions, at a field of view of 0.450 μm by 2.755 μm. The LER analysis was done by

EUV Technology Corporation's SuMMIT and results were averaged from four dies in best focus and best dose conditions [19].

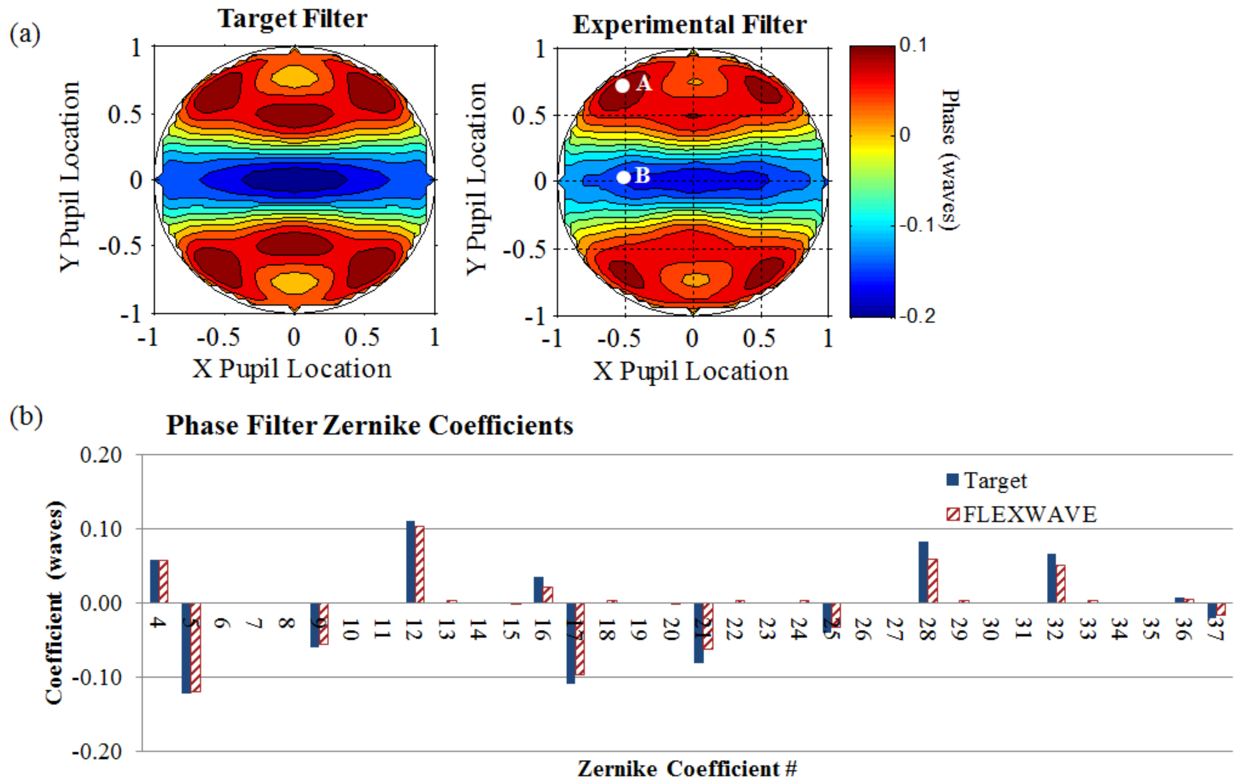

Figure 3.17: (a) Target and experimental filters ($\Delta\Phi_{AB} \approx 0.25$ waves). (b) Zernike coefficients for the target and experimental filters.

3.2 Magnification Correction Studies for Machine Mix and Match

Since IL provides the highest theoretical contrast compared to other lithography techniques, it would be beneficial to scale it for large field IC applications and reduce edge roughness. However, one of the challenges to achieve this goal is lack of pitch fine tuning for exposed image pattern. In the Talbot set up at RIT's Nanolithography labs; image pitch can be coarsely adjusted by using the rotational stages that have the mirrors on them. However, ability in achieving finer pitch adjustment needs to be implemented.

Because, as shown in Fig. 3.18, even modest pitch errors in picometer levels at the field center will accumulate to large image placement errors in nanometer levels at the field edge when thousands of lines are placed next to each other. This will impose a problem, especially for machine mix and match when interference lithography is a part of the layer definition. The image placement error between IL and subsequent trim exposure is to be kept as small as possible.

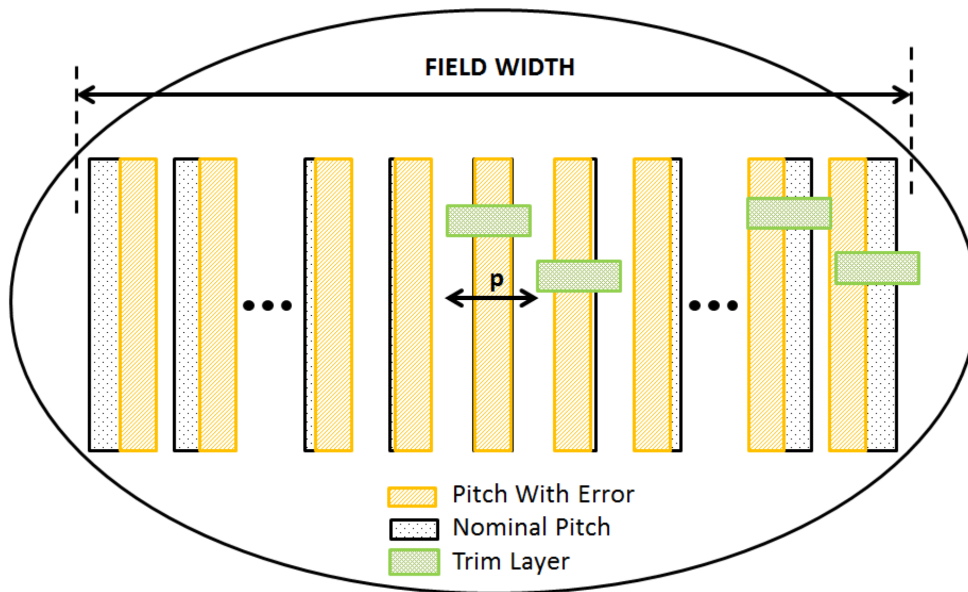

Figure 3.18: Effect of pitch error in overlay of subsequent exposures.

3.2.1 *Approach*

In the reduction Talbot design, the pitch of image at the wafer plane is dependent on both the diffraction angle from the mask and the mirror tilt. Initial experiments on tilting the mask revealed asymmetric change in diffraction angle of the first diffraction orders, with respect to the 0th order; therefore it was not acceptable.

The pitch fine tuning was achieved via fused silica wedges that have been placed on rotational stages between the mirrors and the wafer plane, as shown in Fig. 3.19 (a). This way, the interference angle becomes a function of the deviation angle from the prism and additional degrees of freedom are inserted into the system. The relationship between the deviation angle (δ), the refractive index of the prism material (n) and the incident angle (θ_i) can be given as follows [108]

$$\delta = \theta_i - \alpha + sin^{-1}\left[(\sin(\alpha)\sqrt{(n^2 - sin^2(\theta_i))} - \sin(\theta_i)\cos(\alpha)\right] \quad (3.3)$$

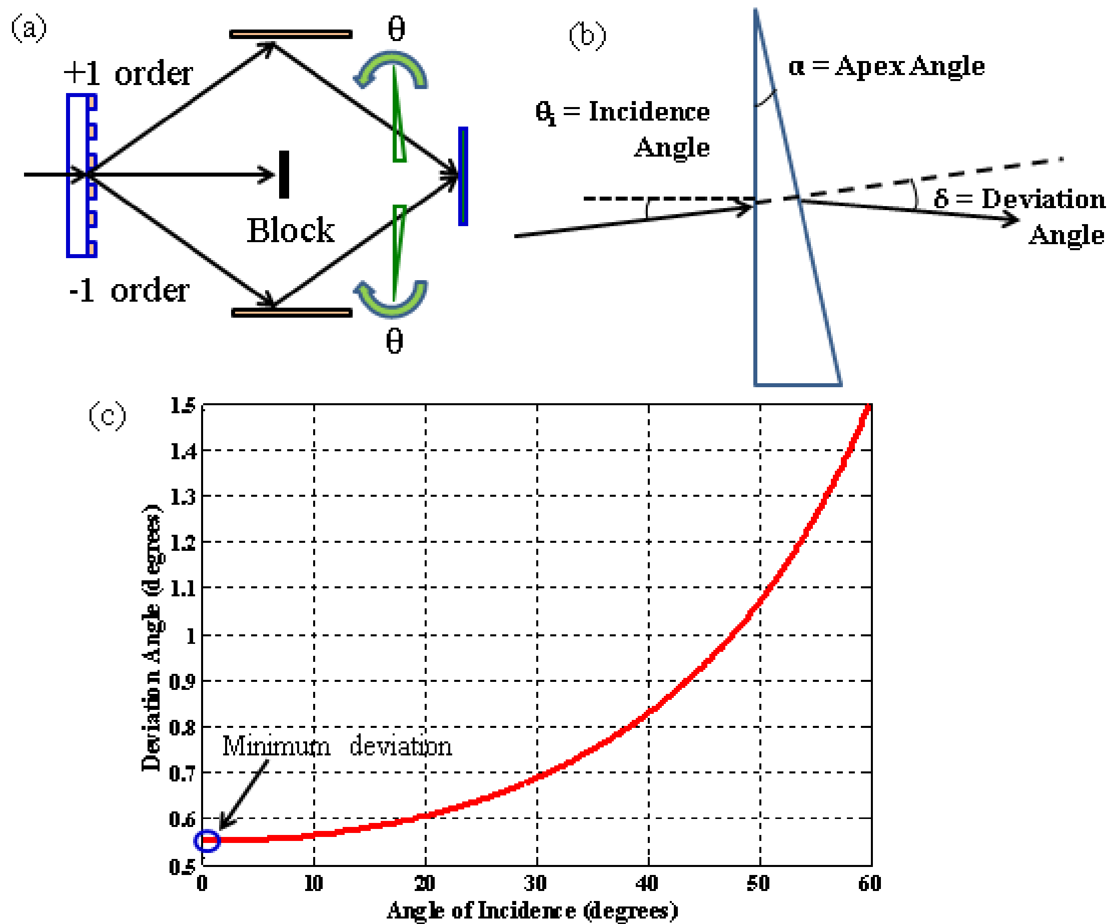

Figure 3.19: (a) Talbot set up with wedges for pitch fine tuning. (b) The definition of deviation angle from the wedge prism. (c) Deviation angle as a function of incident angle for the wedge prism with apex angle of 1.05°.

The schematic of this relationship is shown in Fig. 3.19 (b). The relationship between the deviation angle and the incidence angle for the actual prism ($n_{248\ nm}$=1.55) used in the experiments is plotted in Fig. 3.19 (c). As the wedges are rotated, the incidence angle changes; however, even a large change of incidence angle will result in a small change in the deviation angle, especially at around the minimum deviation point in Fig. 3.19 (c).

3.2.2 *Experimental procedure*

For the experiments, the modified reduction Talbot set up shown in Fig. 3.19 (a) was utilized. The rotation angles (θ) of the stages housing the wedges were simultaneously changed from -10° to +50° with respect to the plane parallel to the wafer plane. Using the IL experimental conditions described in section 3.1.1.2, 9 dies were exposed over various rotation angles, hence through various deviation angles.

SEM images with more than 10 line space pairs in field of view were captured at 32kX magnification as shown in Fig. 3.20 (a). The intensity along the perpendicular direction to the lines were calculated for each case to find the extent of 10 line/space pairs as shown in Fig. 3.20 (b). The pattern pitch was extracted by dividing that number by 10.

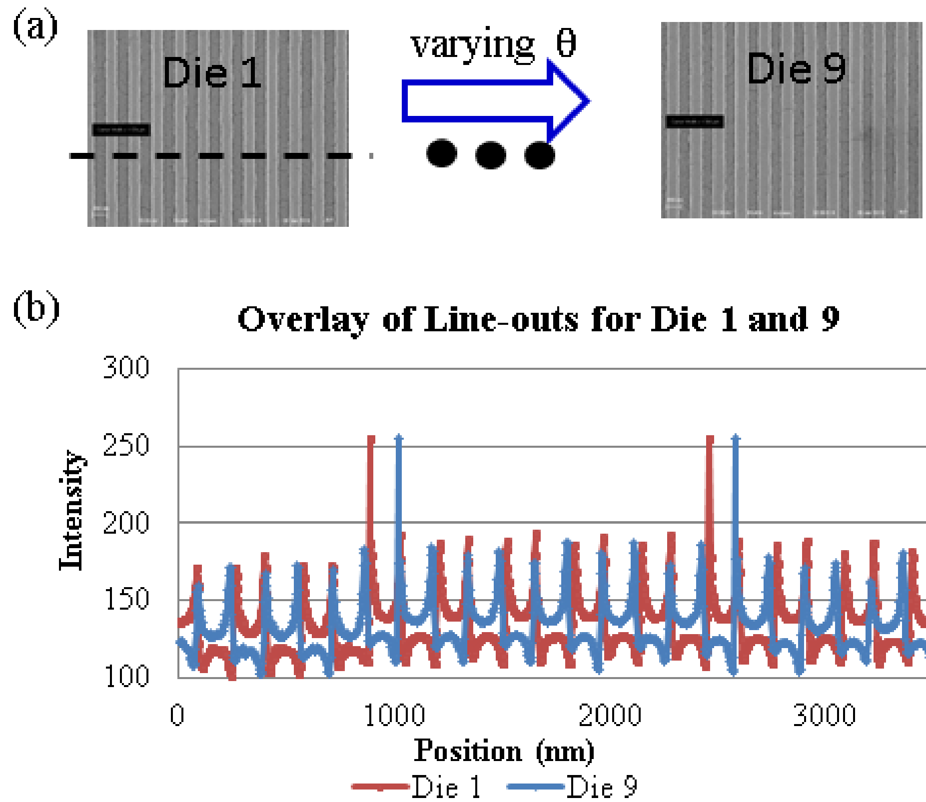

Figure 3.20: (a) Dies exposed over various θ, (b) Line-outs measured over 10 line/space pairs across the SEM field to calculate the pitch.

3.3 **Effect of OPD on Field Size**

In the reduction Talbot design, the OPD is dependent on the field size. It increases linearly as one moved away from the field center. This linear relationship was calculated theoretically in Appendix A, as shown in equation (A8). The comparison of theoretical values to the simulation results calculated at the field edge of increasing beam size is given in Fig. 3.21. For the simulations, free ray tracing software programmed in MATLAB called “Optical_bench” [158] was utilized.

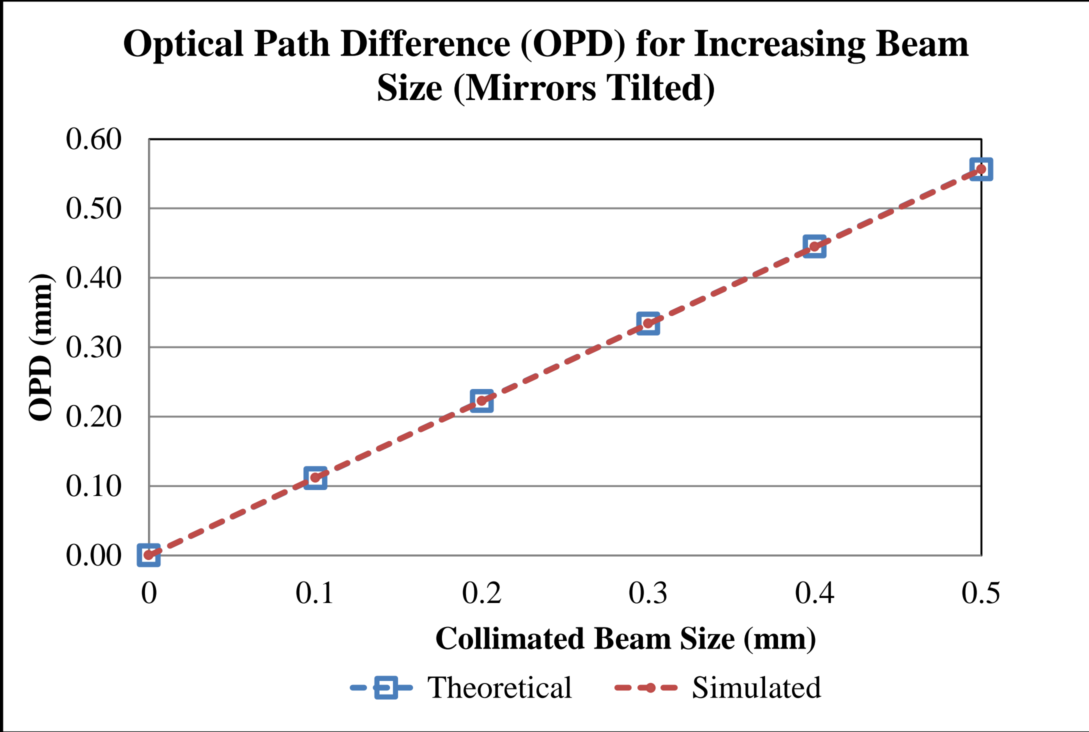

Figure 3.21: Comparison of theoretical OPD calculations with simulated results.

Aside from OPD between the interfering arms, practical limitations should also be considered on the field size when IL is a part of a machine mix and match process to define a critical device layer. Image placement error (IPE) criterion can be utilized for this purpose.

The image placement error, defined as the maximum deviation (X or Y) of the image array relative to a predefined grid, is roughly about 11 % of the half pitch for a node [159]. Table 3.1 shows the tolerable IPE values for various DRAM nodes and the maximum field sizes calculated for 100μ° (1.745μrad) and 50μ° (0.873μrad) residual uncorrectable errors in the interfering angles of an IL set up. For the conservative case (i.e., assuming larger residual error), the usable field size changes between 4 and 8 mm.

Therefore, trying to print fields greater than 10 mm would not be practical for the imaging conditions studied herein.

Table 3.1: IPE tolerances for DRAM nodes (adapted from 2007 edition of ITRS [159])

Year	**2004**	**2006**	**2008**	**2010**	**2012**		**2014**
DRAM (hp, nm)	90	70	57	45	36		28
Image Placement Error (nm)	9.9 (Estim.)	7.7 (Estim.)	6.5	5.2	4.1		3.3
IL defined pitch	180	140	104	90	72		56
Max field length (mm), (res. error=100μ^{o})	7.2	8.3	6.3*	6.7*	6.5^{+}	4.7^{γ}	8.2^{γ}
Max field length (mm), (res. error=50μ^{o})	14.3	16.6	12.5	13.5	13.1^{+}	9.4^{γ}	16.1^{γ}

*Immersion medium water ($n_{193} = 1.44$)

$^{+}$ High index fluid ($n_{193} \geq 1.65$)

$^{\gamma}$ Evanescent wave imaging (sapphire prism)

3.3.1 *Approach*

In order to systematically introduce OPD between the interfering orders, a maskless IL set up similar to the one shown in Fig. 1.8 (b) was utilized. The actual schematic is shown in Fig. 3.22 (modified from [160]). Such maskless IL configurations have been previously utilized in literature [147].

The incoming beam from ELS 4600 laser was split by a polarization independent ~50% beam splitter. After that, the two interfering beams follow different paths. With reference to the figure, optical path length (OPL) taken by one of the beams is given as (a+b), and the other is given as (c+d+e). Therefore, the OPD between the two is given as

$$OPD = (a + b) - (c + d + e) \tag{3.4}$$

The interfering angles on both arms are equal to ζ with respect to wafer plane normal, and the beam paths "a" and "d" are parallel to each other. Under these circumstances, the law of sines can be invoked to come up with following relationships

$$\frac{d}{\sin(\zeta)} = \frac{y}{\cos(\zeta)} = e \tag{3.5}$$

$$\frac{a}{\sin(\zeta)} = \frac{c+y}{\cos(\zeta)} = b \tag{3.6}$$

where, y is the distance from M_1 to the wafer plane. Putting the relationships in (3.5) and (3.6) into OPD definition in (3.4)

$$OPD = (a + b) - (c + d + e) = (c + y) * \left[\frac{\sin(\zeta)}{\cos(\zeta)} + \frac{1}{\cos(\zeta)}\right] - \left[c + y\left(\frac{\sin(\zeta)}{\cos(\zeta)} + \frac{1}{\cos(\zeta)}\right)\right] = c\left[\frac{\sin(\zeta)}{\cos(\zeta)} + \frac{1}{\cos(\zeta)} - 1\right] \tag{3.7}$$

From (3.7), it is seen that the OPD is dependent on the interfering angle and the distance c. If c was equal to 0, the OPD between the arms would also be equal to 0. OPL matching can be done by moving the beam splitter and mirror together left to right, as highlighted with the dashed red box.

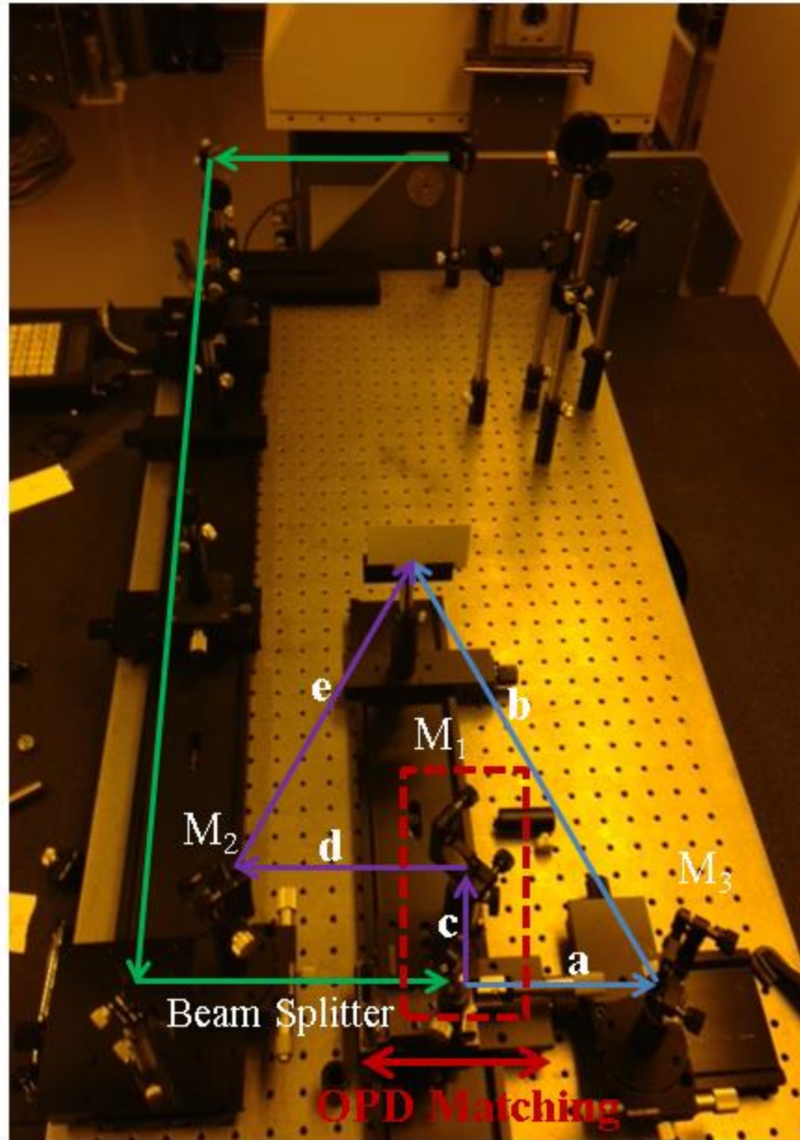

Figure 3.22: Maskless IL set up for studying OPD effect on contrast loss.

3.3.2 *Experimental procedure*

The experiments were performed on the maskless IL set up by using the same processing conditions as previous IL experiments. The image pitch was 300 nm; therefore, the interfering angle was about 24°. From equation (3.7), the OPD at the initial point is equal to 0.55c, where c is between 4 and 5 cm approximately. By using the

micrometer translational stage housing the beam splitter and mirror 1, OPD was changed between the two interfering beams and the SEM images were taken at the field center.

The initial plan was to correlate the CD changes with the contrast loss due to OPD; however, the intensity instability of the ELS4600 laser prohibited any quantitative discussions. Therefore, only qualitative discussions were included in the results.

4. RESULTS AND DISCUSSIONS

4.1 IL Specific LER Mitigation Studies

4.1.1 *Aerial image averaging via directional translation*

4.1.1.1 Interference lithography results

Initial problems observed with the image averaging IL experiments were edge ringing and pattern collapse as shown in Fig. 4.1 (a) and (b), respectively. The former is a result of the large coherence length of the ELS 4600 laser (Δλ=0.7 pm) and was fixed by inserting a spatial filter after the field aperture as shown in Fig. 4.1 (c). The pattern collapse issue was resolved by optimizing the BARC/photoresist thickness.

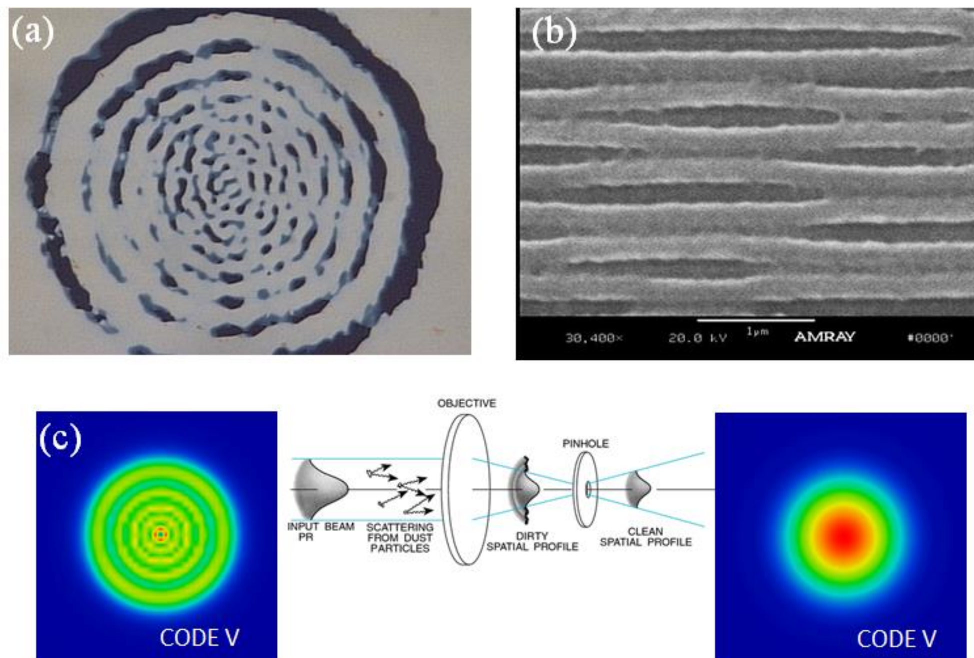

Figure 4.1: Initial problems associated with the interference lithography experiments: (a) ringing issue and (b) pattern collapse issue. (c) Spatial filtering.

In order to get enough data population, LER values were averaged from SEM images taken at 3 locations around the field center. The exposed IL field is very small (diameter less than 3 mm), therefore locating the field center was proven to be very difficult. The process related variability between the image averaged and nominal cases was minimized by consecutive exposures, and co-processing on the same wafer piece as shown in Fig. 4.2 (a). Figures 4.2 (b), (c), and (d) show the comparison of nominal and image averaged LER PSD for 250 nm, 500 nm, and 750 nm shifts respectively.

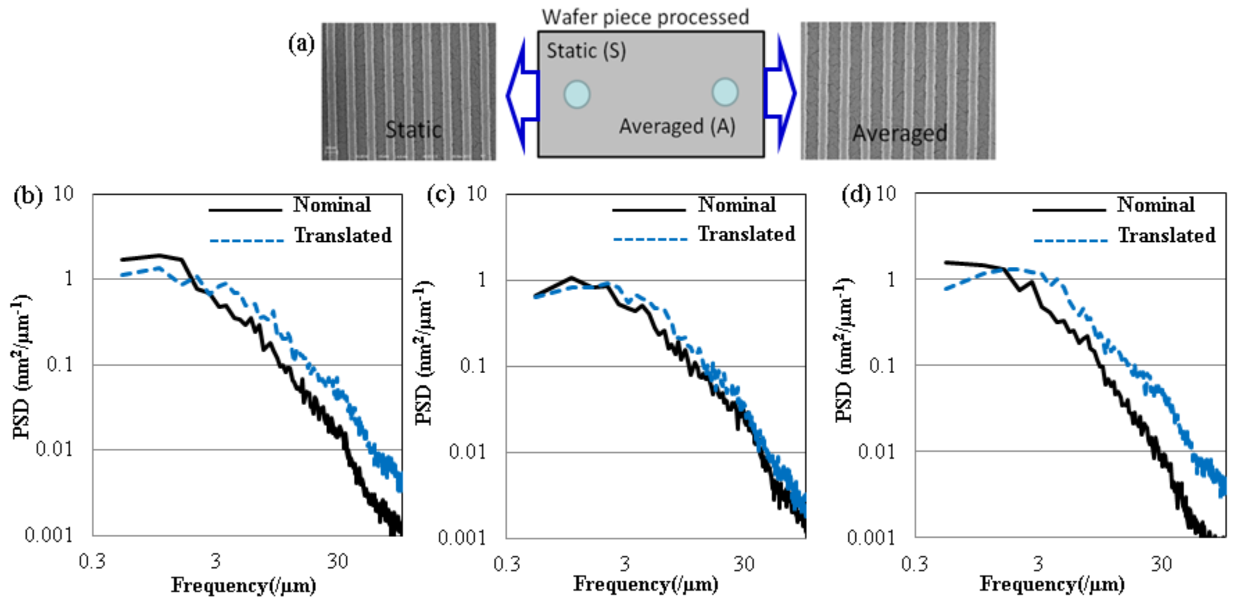

Figure 4.2: (a) Co-processing of static (nominal) and image averaged (translated) dies. Comparison of nominal case LER to image averaged case LER with translation amounts of (a) 250 nm, (b) 500 nm, and (c) 750 nm.

Significant fluctuations in the laser dose were observed during use, attributed to the heating/cooling cycles of the laser. The chiller attached to the laser was not the original chiller for the ELS 4600. Therefore, it was difficult to select a consistent dose to size during the exposures.

From post-lithography SEM image analysis, 5.1 nm CD difference was observed between the nominal die (i.e., no aerial image averaging) and the corresponding shifted die processed on the same wafer piece. In addition, significant amount of increase in roughness with frequencies greater than 2/μm was observed as it can be seen in Fig. 4.2. As a result, the image averaged 3σ LER was 1.9 nm higher than the nominal case on average. These were attributed to the undesired shift in transverse direction, hence, reduction in overall image contrast [18].

The effect of contrast loss on wafer LER was investigated by introducing DC through flood exposure following the 2-beam imaging. The DC values were changed from 0% (no flood exposure, only 2-beam imaging with highest contrast), up to 10% (highest contrast loss case) by keeping the total accumulated dose delivered to the photoresist constant. The results of this study, given in Fig. 4.3 for 139 nm and 75 nm resist thicknesses, show that the LER is strongly dependent on the image contrast [18].

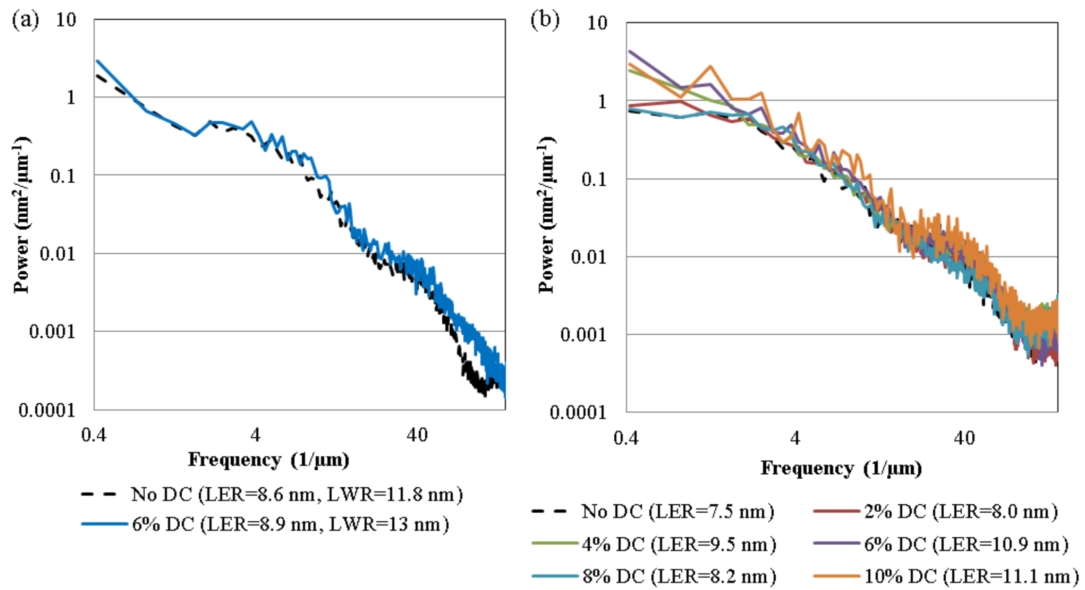

Figure 4.3: Effect of contrast loss through flood exposure on LER PSD (a) for 139 nm thick resist, (b) for 75 nm thick resist [18].

Since there are no alignment marks in the IL defined image field, it is impossible to locate the same location for SEM measurements across different dies. This prevents the ability to compare the roughness values calculated for the same line and along the same segment. Hence, there is going to be some amount of variation between the inter- and intra-field LER values calculated from different SEM images. This can be better understood through Fig. 4.4 (a), where the SEM images taken from 3 different locations around the field center of a nominal die are shown. There is a systematic error present in only Location 1 SEM image. In Fig. 4.4 (b), the problematic locations of the beam splitting mask utilized in the IL experiments are shown as well. Such imperfections will cause inconsistent data due to coherency artifacts. The LER values of 8 central lines from these three locations are given in Fig. 4.4 (c). The location dependency of LER measurements is evident when comparing the LER values calculated from the SEM images taken from three locations on the same die, as shown in Fig. 4.4 (c).

The most crucial conclusion for this part of the study is that LER experiments by utilizing an IL set up is proven to be very risky due to the factors mentioned above. One should refrain from using IL set ups as much as possible while comparing LER values of different materials, or processing conditions. In order to eliminate the location dependency of results, further image averaging experiments were performed on a 193 nm scanner [18].

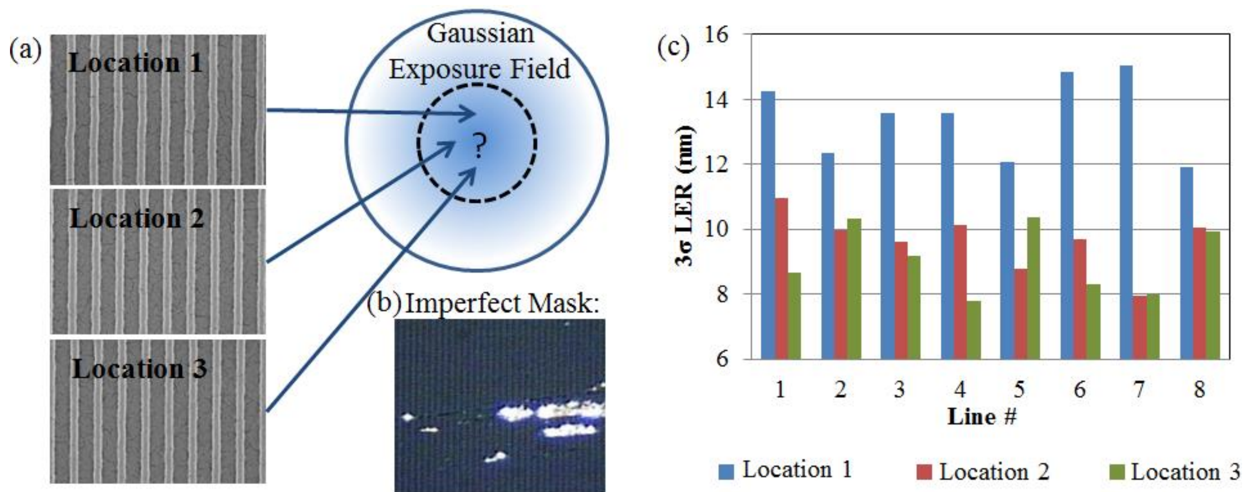

Figure 4.4: (a) Location dependency is observed for IL experiments. (b) Imperfect mask is one of the sources of variations. (c) Intra-field LER values [18].

4.1.1.2 Scanner results

As mentioned before, die 2 in the scanner experiments was included as an alignment error indicator between the superimposed passes; therefore, the aerial image averaged case results were compared to both the die 1 (nominal die) and die 2 results in this section. Even though expected to be very small, there will always be some amount of misalignment error between overlaid passes.

The 3 µm long SEM images taken from die 1 at pitches of 130 nm, and 140 nm are shown in Fig. 4.5 (a), and (b). The 150 nm pitch SEM images of die 1, die 2, and die 8 are shown in Fig. 4.15 (c), (d), and (e), respectively. Such long images were required to capture as much of the LF roughness as possible.

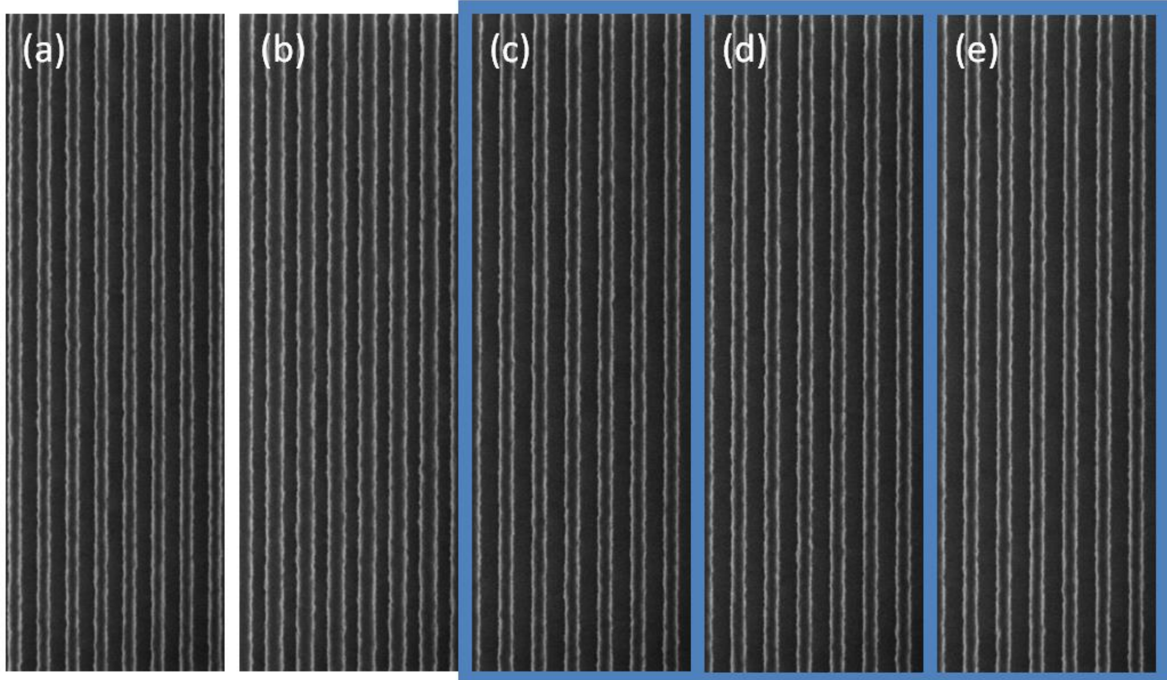

Figure 4.5: SEM pictures of 3 μm long patterns for the pitches of (a) 130 nm (Die 1), (b) 140 nm (Die 1), (c) 150 nm (Die 1), (d) 150 nm (Die 2), and (e) 150 nm (Die 8).

The 3σ LER values of all 8 dies are shown in Table 4.1, for all frequencies and also for just the low frequency range. The inter-field LER variation was less than 0.1 nm (1σ) for the same die. Because the mask roughness contributes to the low frequency region more dominantly, LER mitigation was expected in the low frequency range. However, the differences between the LER values were not significant especially when compared to the 1σ inter-field LER variation of 0.1 nm, possibly due to small mask LER contribution to the overall wafer LER, and the non-ideal way of the applying the image translation. For almost all image averaged dies, the LER value was between the nominal die (die 1) and die 2 [18].

Table 4.1: LER (3σ) values for all frequencies and low frequencies (S: static, P: pass). The amount of shift between passes is given in Fig. 3.4. The inter-field LER variation is 0.1 nm (1σ) [18].

All frequency	**130 nm**	**140 nm**	**150 nm**
Die 1 (S, 1P)	**5.52**	**6.07**	**5.44**
Die 2 (S, 2P)	**5.63**	**6.33**	**5.54**
Die 3 (2P)	*5.65*	6.11	5.42
Die 4 (2P)	5.61	6.18	*5.57*
Die 5 (2P)	5.62	6.23	5.48
Die 6 (2P)	5.58	6.15	5.44
Die 7 (3P)	*5.69*	6.11	5.50
Die 8 (3P)	5.60	6.13	5.37

Low frequency	**130 nm**	**140 nm**	**150 nm**
Die 1 (S, 1P)	**3.51**	**3.54**	**3.36**
Die 2 (S, 2P)	**3.57**	**3.74**	**3.36**
Die 3 (2P)	3.57	3.52	3.31
Die 4 (2P)	3.56	3.54	*3.39*
Die 5 (2P)	3.51	3.62	3.36
Die 6 (2P)	3.57	3.56	3.31
Die 7 (3P)	3.56	3.59	3.31
Die 8 (3P)	3.55	3.58	3.21*

The best case low frequency LER mitigation was 0.15 nm, observed for die 8 compared to the nominal die at 150 nm pitch. Comparing the aerial image averaged dies to die 2, the best case low frequency mitigation corresponds to 0.22 nm, achieved for die 3 at 140 nm pitch [18].

Fig. 4.6 shows the LER PSD of dies 3 and 8, compared to dies 1 (solid black line) and 2 (green dashed line), for the three pattern pitches. The best case mitigation for die 8 is highlighted with a dashed box around it. As it can be seen from this figure, there isn’t significant difference between the LER PSDs between the nominal and image averaged cases. To conclude this study, aerial image averaging did not significantly change LER. In order to draw more conclusive discussions, a mask with known roughness frequencies and amplitudes would be needed [18].

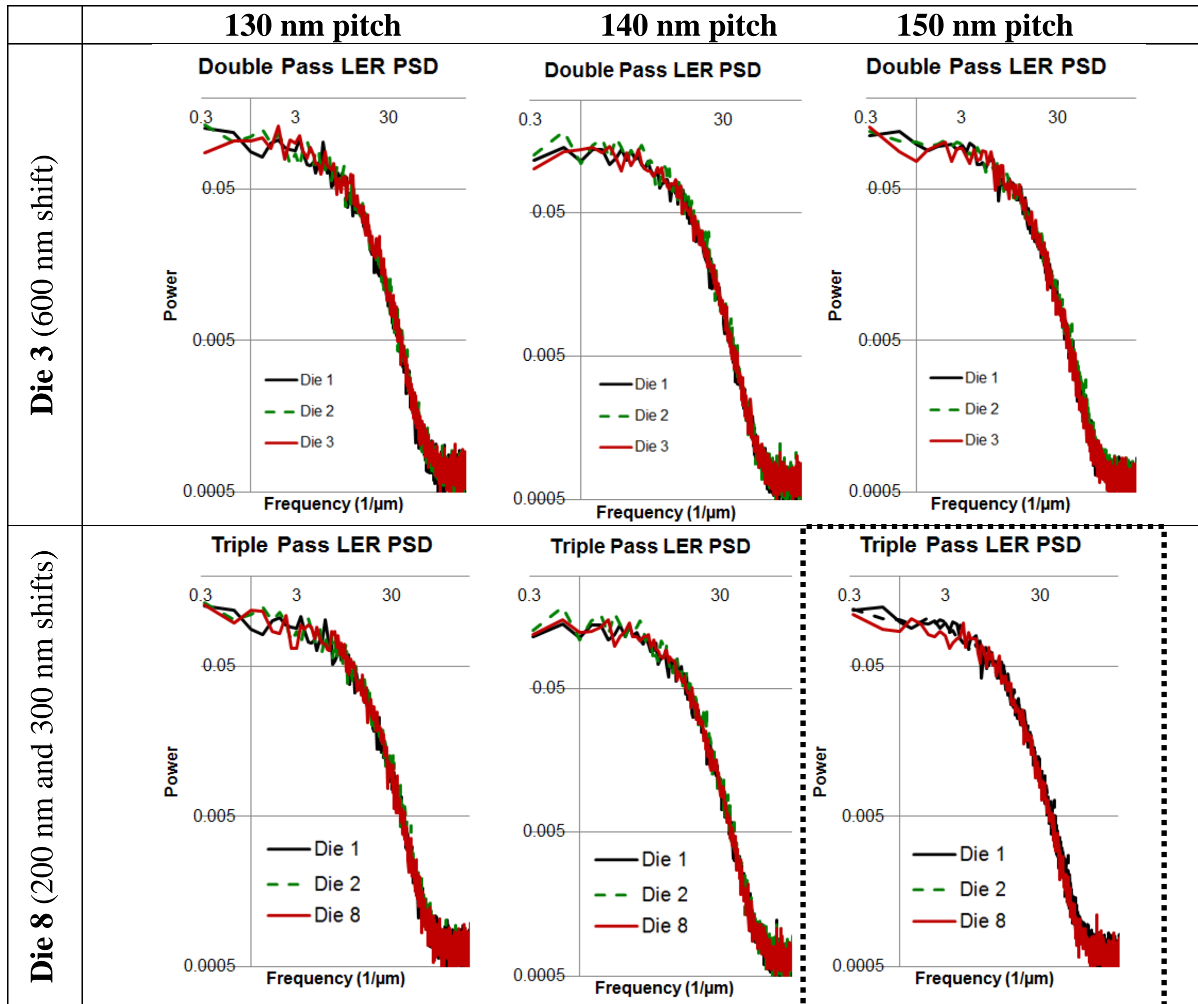

Figure 4.6: Effect of aerial image averaging on LER PSD for die 3 and die 8. Best case mitigation was for die 8 and highlighted with dashed box [18].

4.1.2 *Pupil plane filtering*

Fig. 4.7 shows the roughness transfer of the nominal and phase filtered wafers through aerial image simulations for three different aerial image thresholds (T). The actual experimentally generated FlexWAVE filter was utilized for the latter case. Even though the filter targets 200 nm period, it also reduces the roughness transfer for 500 nm period at the best focus of vertical features.

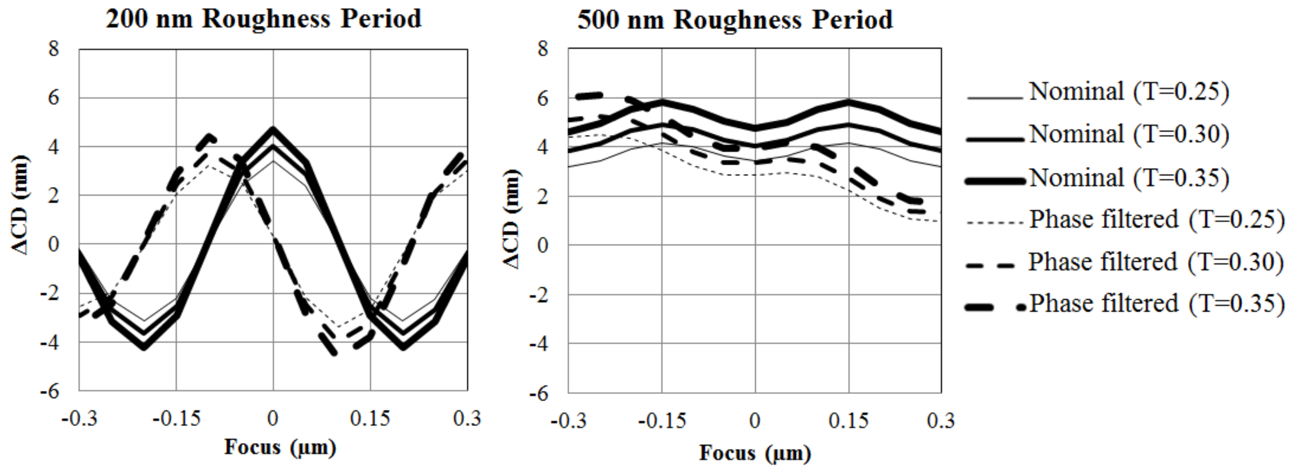

Figure 4.7: Comparison of roughness transfer for nominal and filtered cases through focus for 200 nm and 500 nm roughness periods.

The best fit of the experimental filter to the target filter was achieved at the slit center; therefore, the highest mitigation effect was expected to be around the slit center. In order to observe the dependency of mitigation effect on the accuracy of the fit between the desired and experimental filters, the roughness modules were repeated several times across the scanner slit.

Figures 4.8 (a) and (b) depict the slit center SEM images obtained from the nominal and phase filtered wafers for 200 nm roughness periods in anti-correlated and correlated fashions, respectively. The roughness amplitude (A) was changed from 1nm/edge up to 9nm/edge. The comparison of SEM images clearly shows the mitigation, even at large amplitude of 9nm/edge. The mitigation was found to be independent of the correlation type between the edges, verifying the simulation results. The corresponding SEM images for 500 nm period are shown in Fig. 4.9. The mitigation for 500 nm period was less obvious from the SEM images, compared to 200 nm period images.

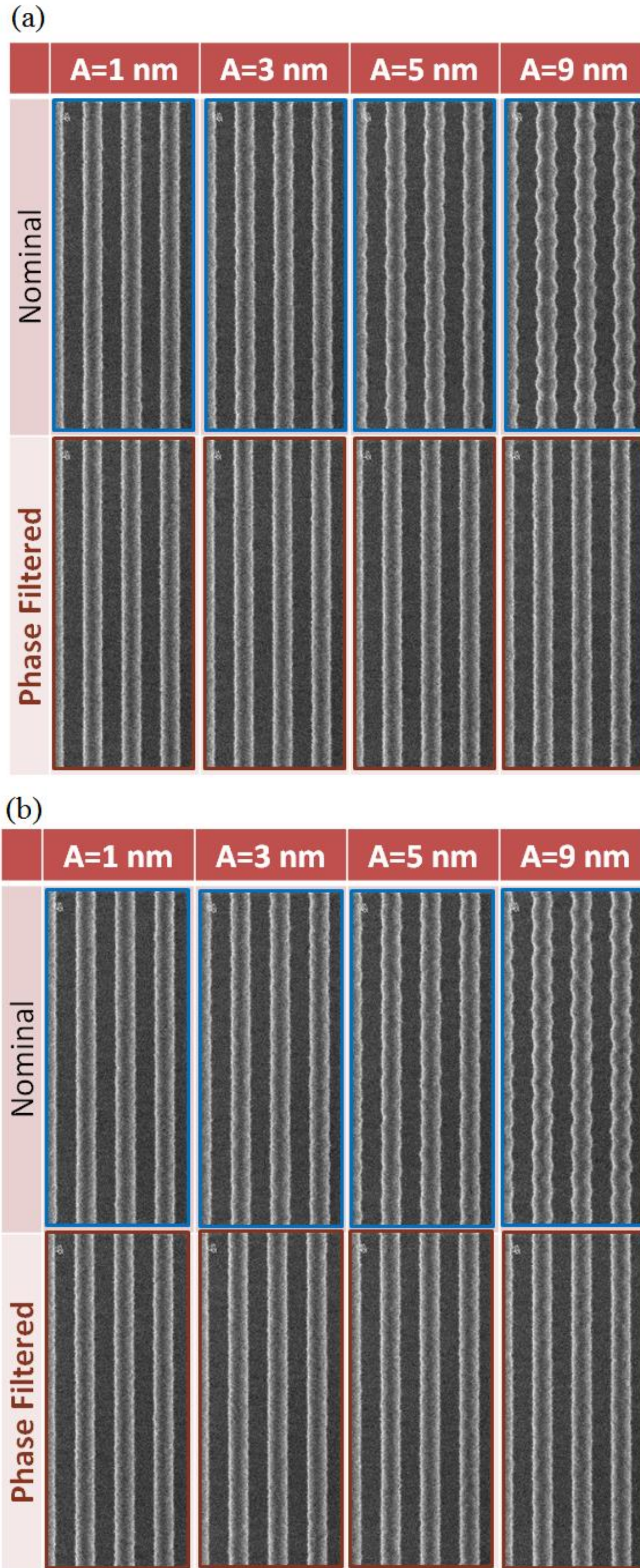

Figure 4.8: Nominal and phase filtered SEM images for 200 nm roughness period in (a) anti-correlated and (b) correlated fashions.

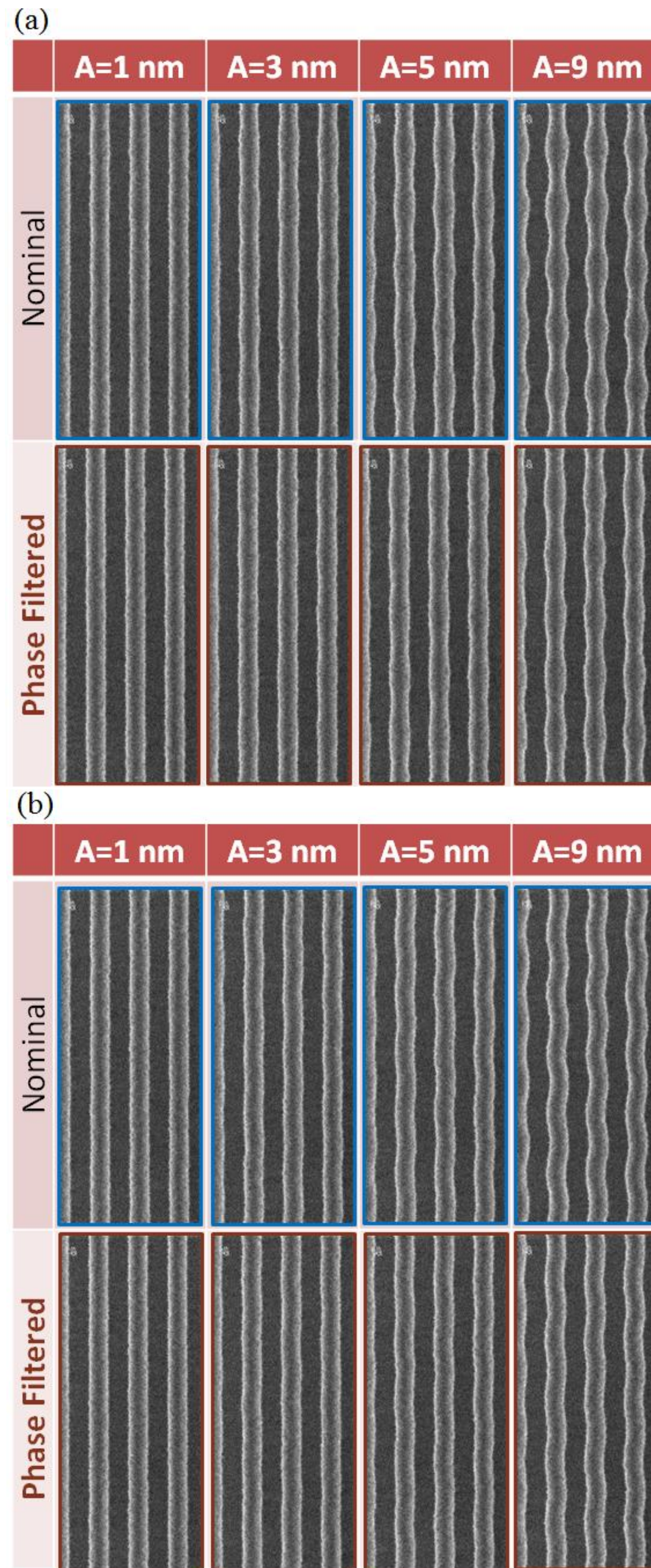

Figure 4.9: Nominal and phase filtered SEM images for 500 nm roughness period in (a) anti-correlated and (b) correlated fashions.

Figures 4.10 (a) and (b) show the through slit 3σ LWR values for nominal and phase filtered cases for 200 nm and 500 nm roughness periods, respectively. As expected, the mitigation was at maximum around the field center.

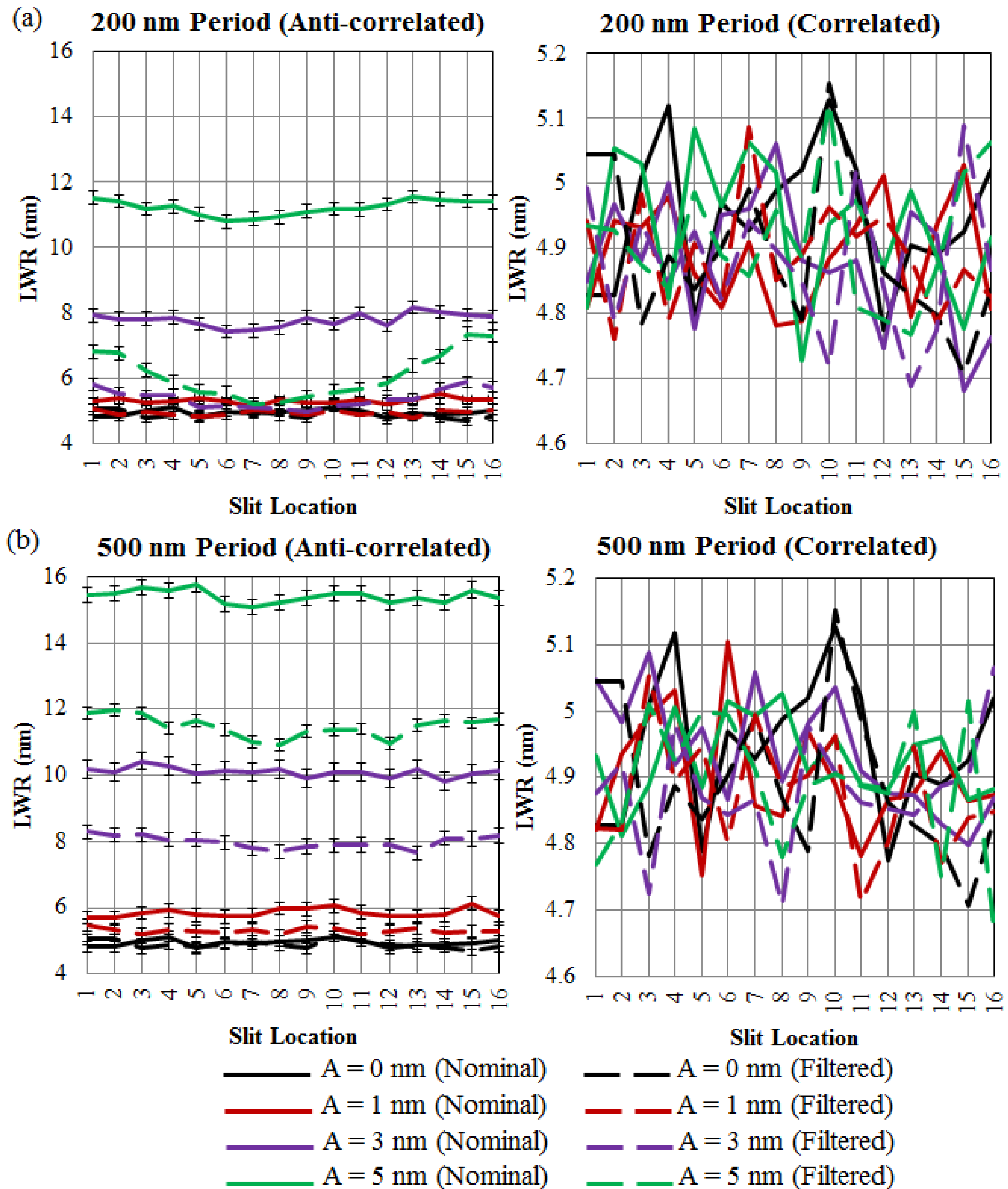

Figure 4.10: Through slit LWR values for the nominal and wavefront cases programmed with periods of (a) 200 nm and (b) 500 nm, in both correlation types. Error bars correspond to average 1σ LWR variations.

When roughness is correlated, its amplitude will not have significant effect on LWR. But, the effect will be visible in LER plots, as shown in Figures 4.11 and 4.12 for two different frequency ranges. The latter includes only the LF roughness, which is more crucial for the device electrical performance.

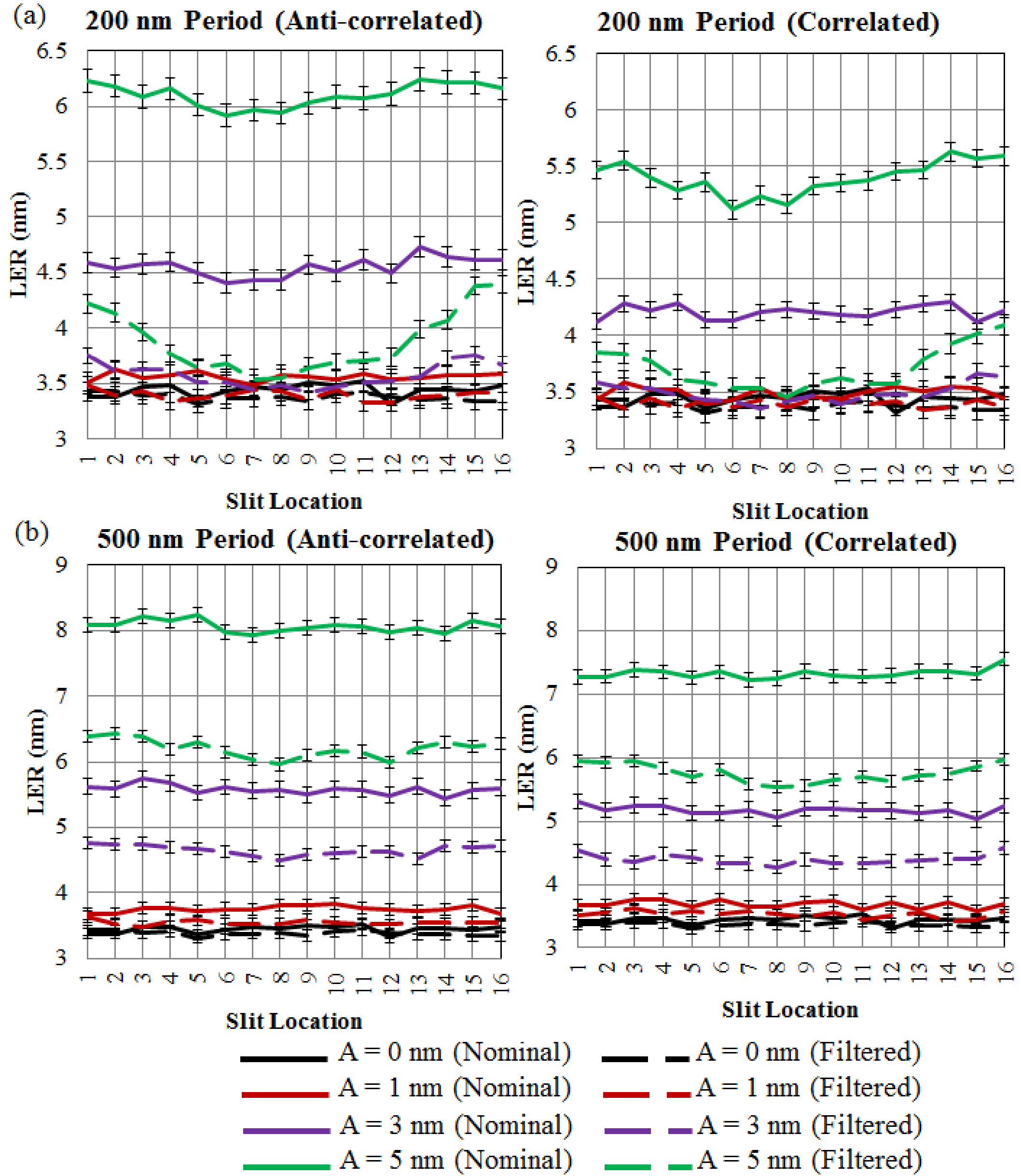

Figure 4.11: Through slit LER values for the nominal and phase filtered cases programmed with periods of (a) 200 nm and (b) 500 nm, in both correlation types. Error bars correspond to average 1σ LER variations.

These figures show that the systematic mask contribution to the wafer LER increases for large programmed roughness amplitudes. However, the phase filter reduces this contribution significantly, especially for the target period of 200 nm. The slit center has the highest roughness mitigation (shown separately in Fig. 4.13).

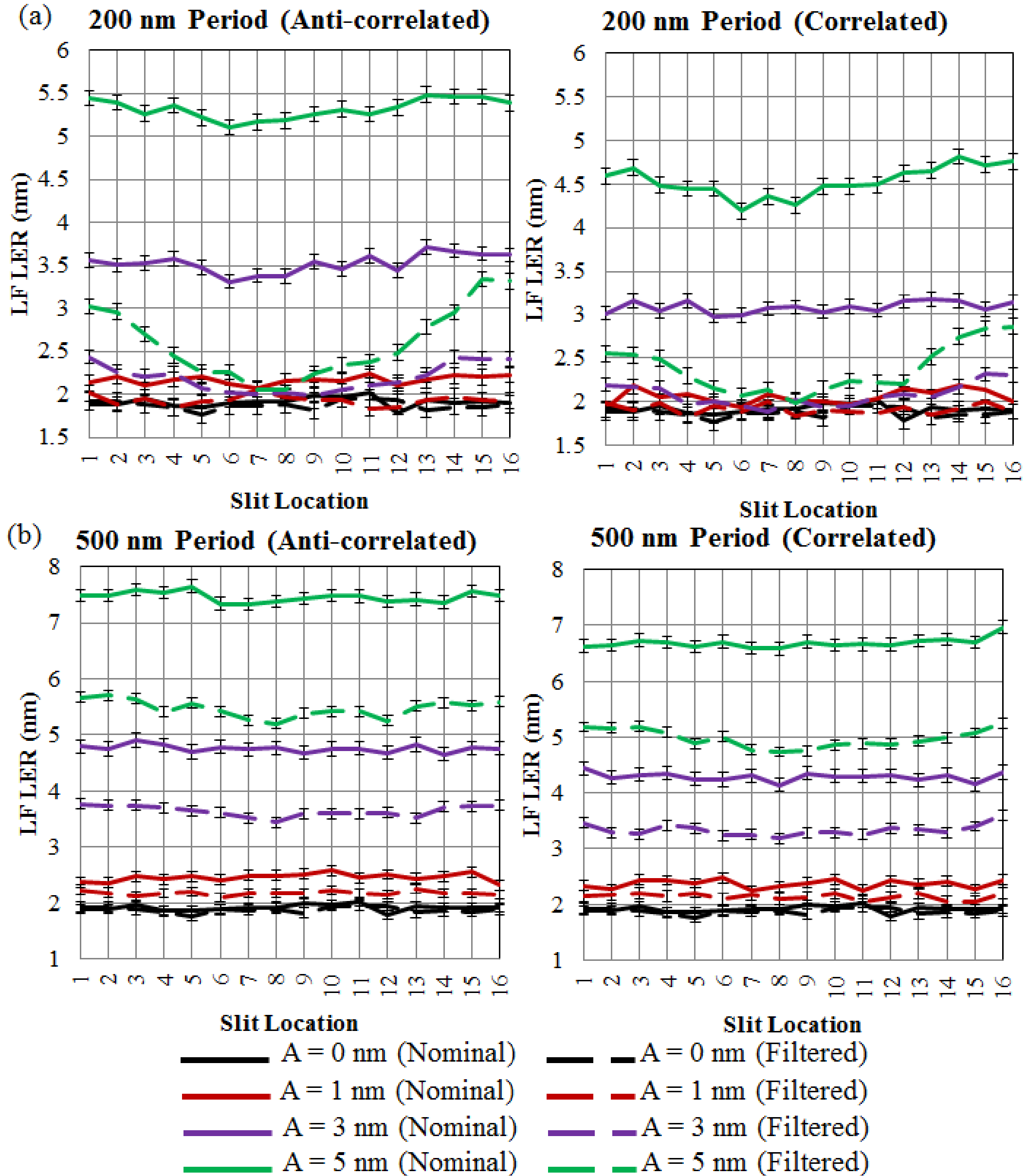

Figure 4.12: Through slit LF LER values for the nominal and wavefront cases programmed with periods of (a) 200 nm and (b) 500 nm, in both correlation types. Error bars correspond to average 1σ LER variations.

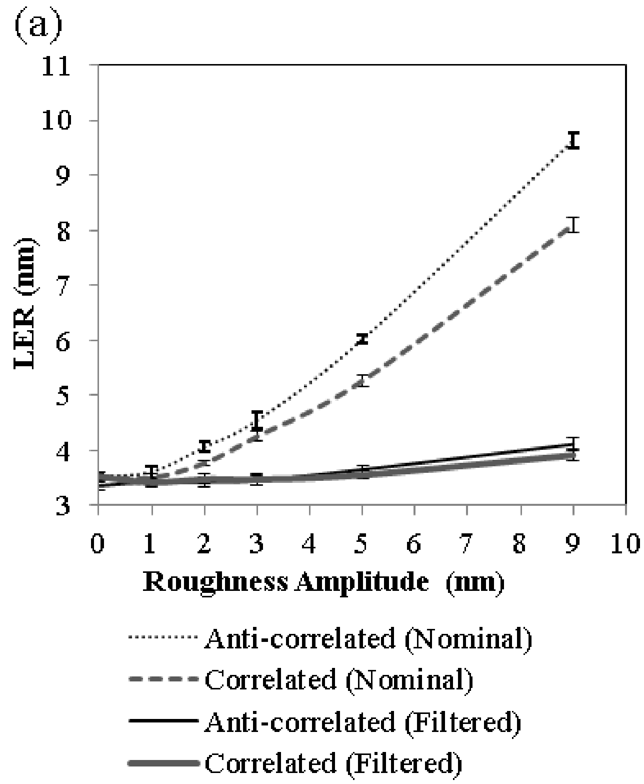

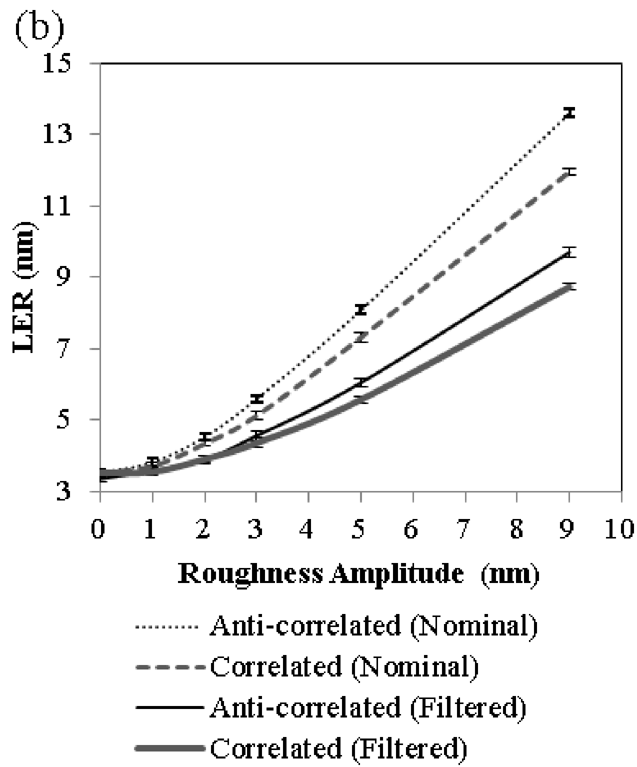

Figure 4.13: Slit center LER values for (a) 200 nm, and (b) 500 nm roughness periods at the slit center. Both correlation types are considered [19].

The effect of phase filtering on LER power spectral density is shown in Fig. 4.14, for amplitudes of 1nm/edge and 5nm/edge programmed in anti-correlated fashion. The peaks at 5/µm in (a) and (b) correspond to the 200 nm roughness period, and the peaks at 2/µm in (c) and (d) correspond to 500 nm roughness period. The peak at 5/µm frequency is significantly reduced as evident from Fig. 4.14 (a) and (b). The rest of the LER PSD seems unchanged.

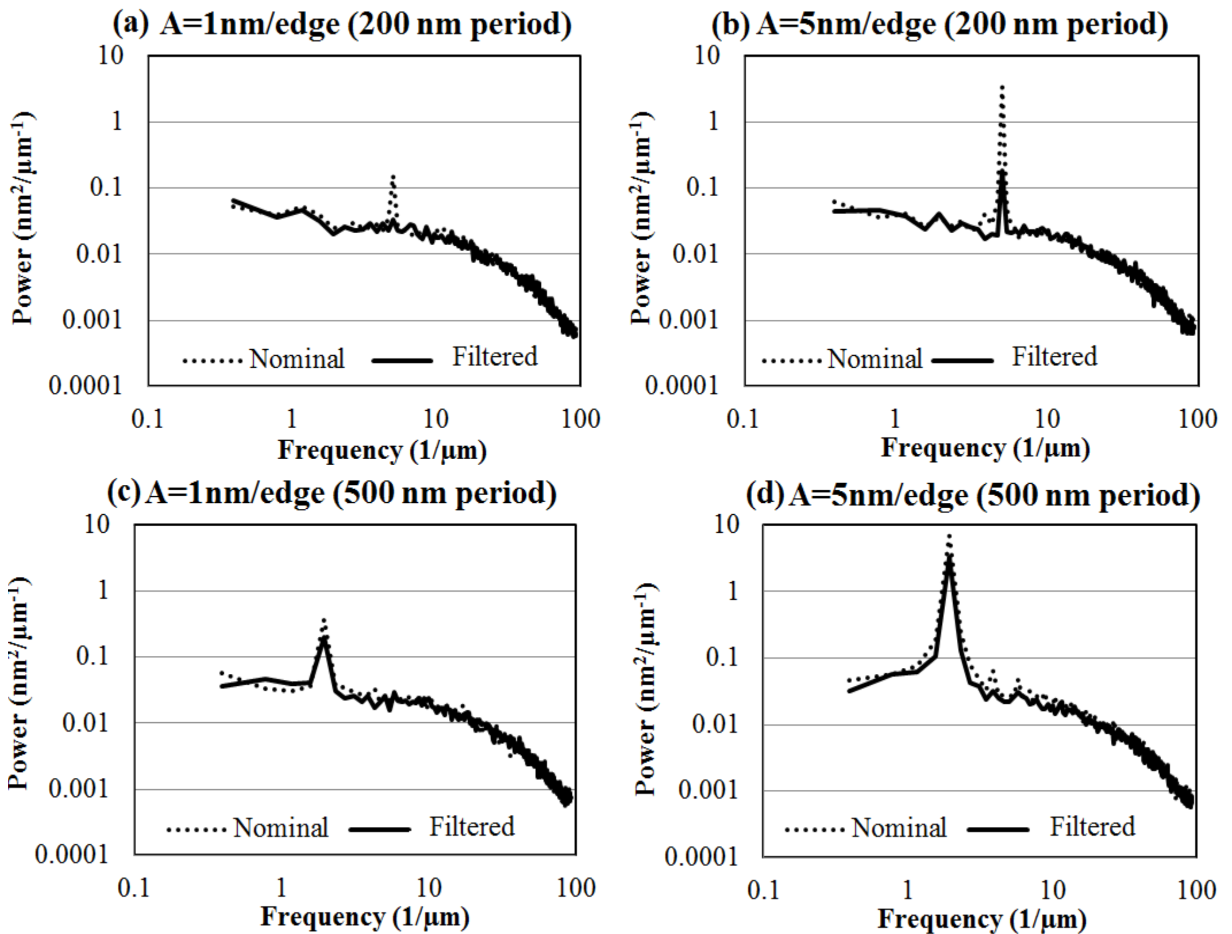

Figure 4.14: LER PSD of nominal and phase filtered wafers. Comparison for 200 nm roughness period with amplitudes of (a) 1nm/edge and (b) 5nm/edge. Comparison for 500 nm roughness period with amplitudes of (c) 1nm/edge and (d) 5nm/edge.

The LER and LWR are related to each other through the correlation between the two edges. The following describes this relation mathematically [98]

$$\sigma_{LWR}^2 = \sigma_{LER,L}^2 + \sigma_{LER,R}^2 + 2CF\sigma_{LER.L}\sigma_{LER.R} \quad (4.1)$$

where -1<CF<1. When there is a correlation between the edges (either in perfectly correlated or anticorrelated fashions), the amplitude of CF will reach 1. If there is no correlation between the edges, the CF will be around 0 [98]. The former case corresponds to the situations, where there is more systematic contributions to the wafer LER (such as mask roughness). Therefore, as shown in Fig. 4.15, the CF goes to either 1 or -1 for increasing values of roughness amplitude for the nominal cases. The phase filter reduces the magnitude of CF, indicating mitigation of the systematic contributions to the wafer LER. As expected, the impact is more visible for the 200 nm period roughness.

Since the mask roughness is not a major contributor to the wafer LER, the effect of phase filtering on reference lines with no programmed roughness (A=0) was expected to be very small. Fig. 4.16 (a) verifies this expectation by plotting 3σ LER values for smooth features through mask bias.

It has been aforementioned that the HF filtering effect on mask roughness does not translate directly to LER; however, when the amplitude is large enough (e. g., >10% of CD), it starts to degrade NILS and indirectly increase the roughness [97]. Fig. 4.16 (b) shows this phenomenon where simulated NILS reduction is overlaid on top of the measured resist LER of the phase filtered case, for various roughness amplitudes. The decrease in NILS is greater than 1% when the amplitude is greater than 10% of the CD and the 3σ LWR starts to increase.

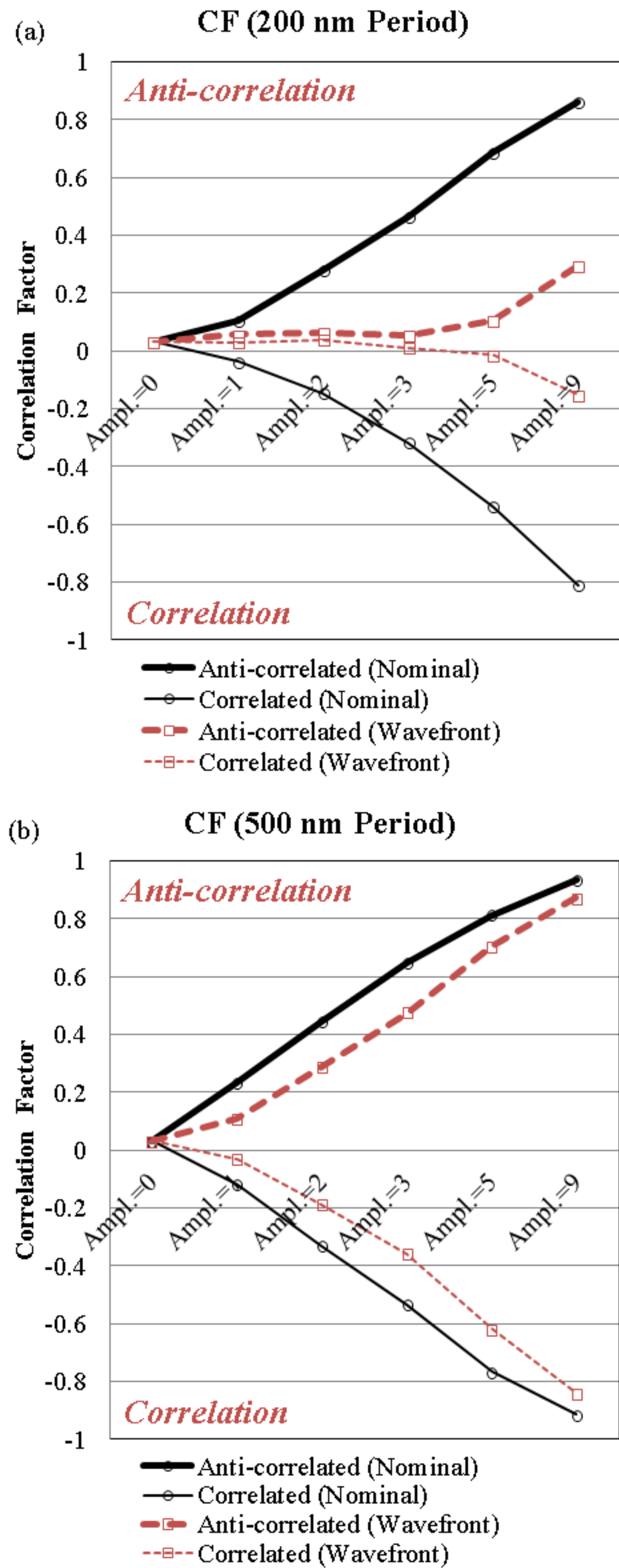

Figure 4.15: Experimentally calculated CF for (a) 200 nm, (b) 500 nm roughness periods.

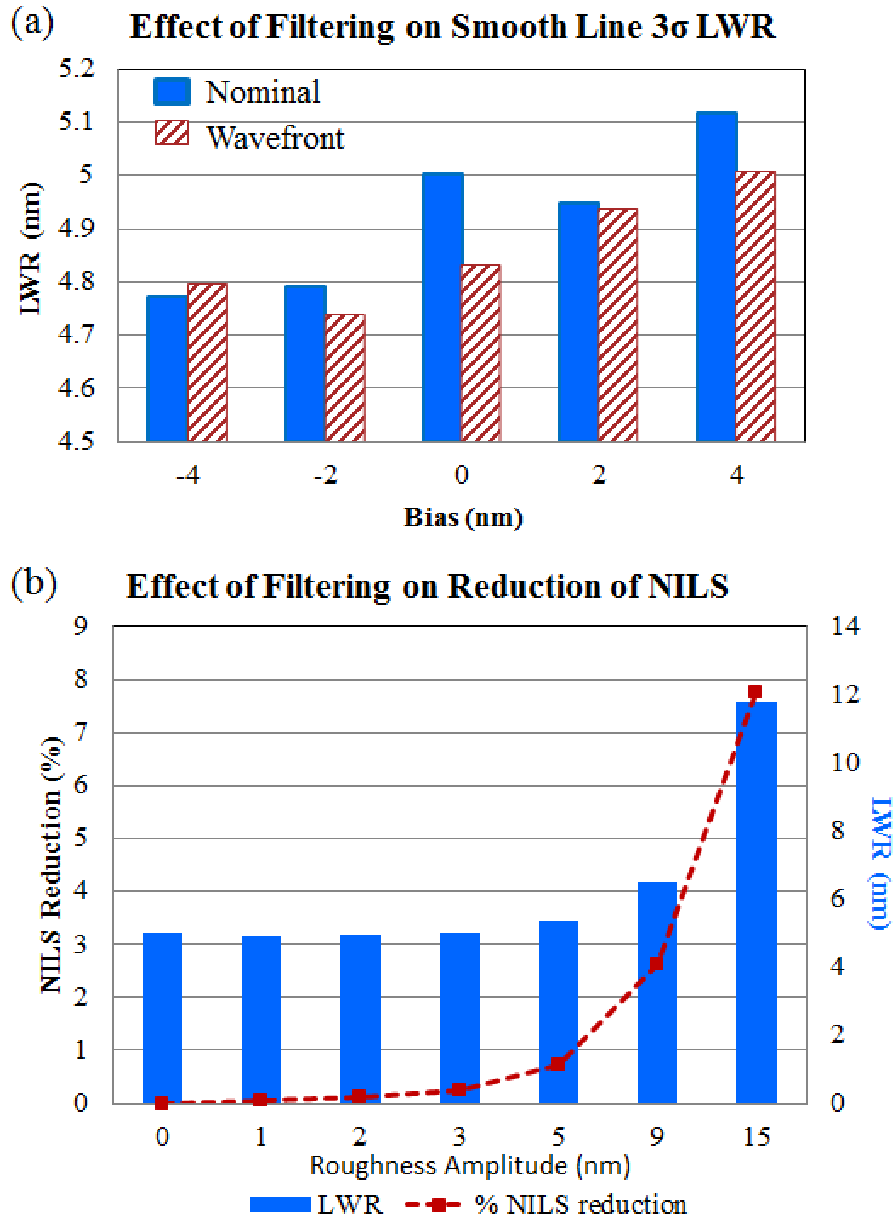

Figure 4.16: Effect of filtering on (a) smooth line 3σ LWR through bias. (b) NILS reduction and LWR increase through roughness amplitude for the filtered case.

In case of the HF filtering of the optical system, diffraction orders are always outside the resolution limit of the system; therefore, they cannot be translated to the aerial

image directly. This kind of filtering will always result in reduction of the NILS and deterioration of LER, to a very small extent.

However, in the situations where the orders would actually be captured at the pupil plane; if the filter is not utilized, it is easily seen from Fig. 4.13 that the direct transfer of these roughness orders results in much higher roughness values. For instance, when the anti-correlated roughness amplitude is 9 nm per edge, the reduction in NILS is 2.6% due to filtering resulting in a 3σ LER of 4.05 nm; yet, the nominal case would have a 3σ LER value of 9.5 nm for the same amplitude.

4.2 Magnification Correction Results

The main objective of pitch fine tuning was to show the ability of changing the pitch in a reduction Talbot IL set up by less than 1 nm accuracy. Fig. 4.17 shows the pattern pitch at wafer plane as a function of the rotation angle. Through the full available span of angles (a range of 60°), the maximum change in the pitch is 4.5 nm.

The minimum deviation from the wedges was achieved at about θ=24º, where the beam passing through the prism is parallel to the base of the wedge. As it is seen, in the vicinity of minimum deviation point, i.e., 10º<θ<30º, less than 0.5 nm pitch adjustment is achieved. For finer adjustments, wedges with smaller apex angles can be utilized.

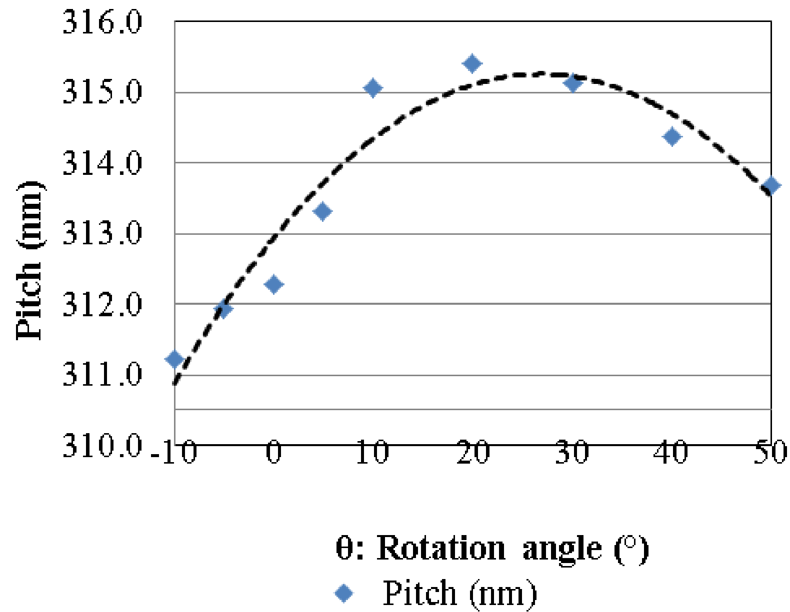

Figure 4.17: Pitch fine tuning via change in rotational angle of the wedge prism holder. Dashed line corresponds to a trend line fit to the experimental data points shown with blue diamonds.

4.3 Maskless IL Results

Maskless IL experiments were performed to see the qualitative effect of OPD on the image fidelity. The ELS4600 laser has 0.7 pm laser bandwidth, therefore the temporal coherence length is about 87 mm. When OPD between the interfering beams become comparable to the coherence length, the ability of the constructively and destructively interfering is diminished.

Figure 4.18 (a) shows the field center SEM images for different amounts of OPD values introduced between the two interfering beams. The image pitch was 300 nm and the SEM magnification was 32kX. Initially, there was a mismatch between the intensities of interfering orders, which effectively resulted in 25% DC. The intensity matching

between the orders was achieved by making small adjustments in the beam splitter and M_3 rotations. The remaining effective DC value was around 2%.

Figures 4.18 (b), (c), and (d) shows the field center of 2% DC die at a magnification of 6kX. The pattern fidelity is degraded due to the increased OPD. Assuming the pattern quality of (b) and (d) are acceptable, the max field size of the 300 nm pitch IL pattern would be less than 10 mm. Further quantitative discussions cannot be pursued due to the dose instability of the ELS 4600.

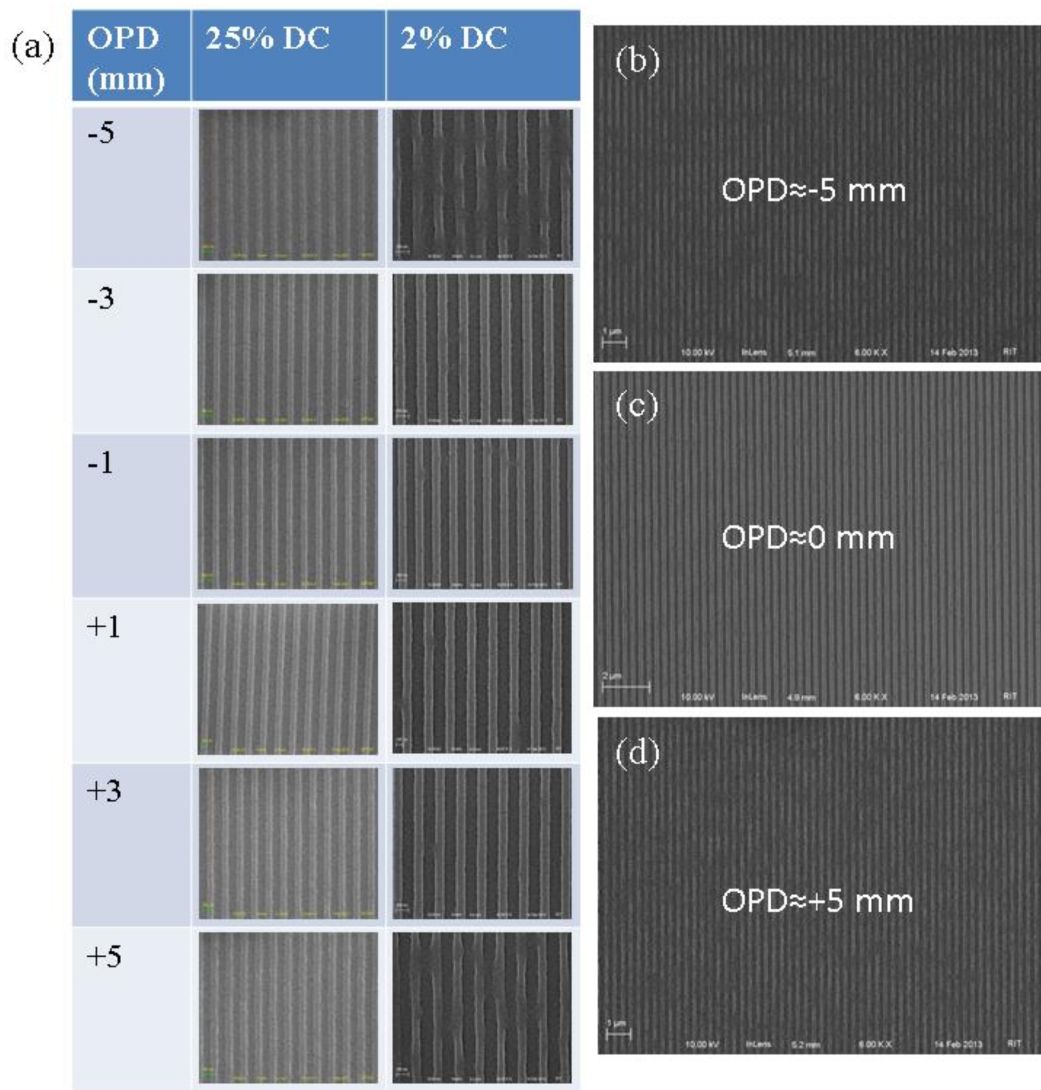

Figure 4.18: Effect of OPD on image quality as a function of DC.

5. CONCLUSIONS

Line edge roughness is seen as one of the most crucial challenges to be addressed in advanced technology nodes. In order to alleviate this problem, several options were explored in this work for the interference like lithography imaging conditions.

The most straight forward option was to scale IL for large field integrated circuit (IC) applications and benefit from the inherent LER mitigation due to the high image contrast. However, there are challenges that would prohibit this approach. Two of the challenges were addressed in this work: (1) theoretical and practical field size limitations, and (2) magnification correction (pitch fine-tuning) ability.

The effect of OPD on image fidelity was shown qualitatively with a maskless IL set up at 300 nm image pitch, where the OPD between the two interfering arms was changed systematically with a micrometer translation stage. The image fidelity degraded significantly for OPD values greater than 5 mm. Therefore, the large field for this particular case should be less than 10 mm. A practical limit on the field size was set by the image placement error (IPE) between the IL defined periodic grid and a subsequent trim exposure. The practical IL field sizes were calculated to be less than 9 mm, assuming 100μ° uncorrectable (residual) interference angle error, for the DRAM half pitches down to 28 nm.

The magnification correction capability for the reduction Talbot IL set up was achieved by inserting two fused silica wedges mounted on rotational stages between the

wafer plane and the first diffraction order collecting mirrors. Less than 0.5 nm pitch adjustment was successfully shown at around the minimum deviation angle of the prism.

In addition, two other LER reduction approaches, which are also applicable to projection lithography under interference-like conditions, were explored through mitigating the mask absorber roughness contribution: (1) aerial image averaging via directional translation, and (2) pupil plane filtering.

LER experiments by utilizing and IL set up showed daily variations and location dependent results. Therefore, scanner experiments were pursued for the mask roughness mitigation part of the research. Aerial image averaging via directional translation results showed that there wasn't a significant amount of LER change between the nominal and image averaged dies. In order to yield more conclusive results, a 1D mask with programmed roughness of known frequency and amplitudes was needed (not available at the time).

Pupil plane filtering technique served better for the purpose of mask roughness mitigation. A target phase filter was realized by ASML's FlexWAVE wavefront manipulator to mitigate 200 nm roughness period programmed on 64 nm vertical line/space patterns through various roughness amplitudes. The experimental results showed the transfer of mask roughness at the target frequency was eliminated when the optimized phase filter was utilized. There was some amount of reduction for the transfer of 500 nm roughness period as well. The focus dependency of the mitigation can be overcome by performing transmission filtering instead of the phase filtering.

6. APPENDIX A

Since it is one of the goals of this research to increase field size of IL exposure as large as possible, OPD should be characterized and its dependence on the system parameters needs to be understood. In order to calculate the OPD for the source point originating from point C (field edge) and interfering at focal plane, optical path lengths (OPL) of ±1 orders need to be found.

The optical path length of (-1) order, $OPLc_{(-1)}$, can be calculated from two triangles: CE_1R and SE_1J, giving the following relationships, respectively

$$|CE_1| = \frac{|CR|}{\sin(\beta + \alpha)} \qquad \text{and} \qquad |E_1J| = \frac{|SJ|}{\sin(\beta - \alpha)} \qquad (A1)$$

So, optical path length of (-1) order can be given as the summation of above two

$$OPL_{C(-1)} = |CE_1| + |E_1J| = \frac{|CR|}{\sin(\beta + \alpha)} + \frac{|SJ|}{\sin(\beta - \alpha)} = \frac{|CR|}{\sin(\beta + \alpha)} + \frac{|BI| - |CR|}{\sin(\beta - \alpha)}$$

$$= |CR| * \left[\frac{1}{\sin(\beta + \alpha)} - \frac{1}{\sin(\beta - \alpha)}\right] + \frac{|BI|}{\sin(\beta - \alpha)} \qquad (A2)$$

Similarly, the optical path length of (+1) order, $OPLc_{(+1)}$, can be calculated from two triangles, CG_2P and OG_2J, giving the following relationships, respectively

$$|CG_2| = \frac{|CP|}{\sin(\beta + \alpha)} \qquad \text{and} \qquad |G_2J| = \frac{|OJ|}{\sin(\beta - \alpha)} \qquad (A3)$$

So, optical path length of (+1) order can be given as

$$OPL_{C(+1)} = |CG_2| + |G_2J| = \frac{|CP|}{\sin(\beta+\alpha)} + \frac{|OJ|}{\sin(\beta-\alpha)} = \frac{|CP|}{\sin(\beta+\alpha)} + \frac{|BI|-|CP|}{\sin(\beta-\alpha)}$$

$$= |CP| * \left[\frac{1}{\sin(\beta+\alpha)} - \frac{1}{\sin(\beta-\alpha)}\right] + \frac{|BI|}{\sin(\beta-\alpha)} \qquad (A4)$$

Optical path length difference between ±1 orders is $OPD_{C(\pm1)}=OPL_{C(-1)}- OPL_{C(+1)}$, and equal to

$$OPD_{C(\pm1)} = |CR| * \left[\frac{1}{\sin(\beta+\alpha)} - \frac{1}{\sin(\beta-\alpha)}\right] + \frac{|BI|}{\sin(\beta-\alpha)} -$$

$$|CP| * \left[\frac{1}{\sin(\beta+\alpha)} - \frac{1}{\sin(\beta-\alpha)}\right] - \frac{|BI|}{\sin(\beta-\alpha)}$$

$$OPD_{C(\pm1)} = [|CR| - |CP|] * \left[\frac{1}{\sin(\beta+\alpha)} - \frac{1}{\sin(\beta-\alpha)}\right] \qquad (A5)$$

By using the following relationships

$$|CR| - |CP| = -|PR|$$

$$\cos(\alpha) = \frac{|PR|}{|E_1G_1|} = \frac{|PR|}{|E_2G_2|}$$

$$|E_1G_1| = |AC| * \frac{\cos(\theta)}{\sin(\theta+\alpha)}$$

$$-|PR| = \cos(\alpha) * |E_1G_1| = -|AC| * \cos(\alpha) * \frac{\cos(\theta)}{\sin(\theta+\alpha)}$$

Finally yielding

$$\mathrm{OPD}_{C(\pm 1)} = [|CR| - |CP|] * \left[\frac{1}{\sin(\beta+\alpha)} - \frac{1}{\sin(\beta-\alpha)}\right]$$

$$= -|PR| * \left[\frac{1}{\sin(\beta+\alpha)} - \frac{1}{\sin(\beta-\alpha)}\right]$$

$$= -|AC| * \cos(\alpha) * \frac{\cos(\theta)}{\sin(\theta+\alpha)} * \left[\frac{1}{\sin(\beta+\alpha)} - \frac{1}{\sin(\beta-\alpha)}\right]$$

$$= (-1) * |AC| * \cos(\alpha) * \frac{\cos(\theta)}{\sin(\theta+\alpha)}$$

$$* \left[\frac{1}{\cos(\theta)} - \frac{1}{\cos(\theta+2\alpha)}\right] \qquad \text{(A6)}$$

Following same approach, we can calculate the OPD as a function of source size |AC| for a point source A, which is on the opposite site but same distance away from the origin as

$$\mathrm{OPD}_{A(\pm 1)} = [|AV| - |AT|] * \left[\frac{1}{\sin(\beta+\alpha)} - \frac{1}{\sin(\beta-\alpha)}\right]$$

$$= |PR| * \left[\frac{1}{\sin(\beta+\alpha)} - \frac{1}{\sin(\beta-\alpha)}\right]$$

$$= (+1) * |AC| * \cos(\alpha) * \frac{\cos(\theta)}{\sin(\theta+\alpha)} * \left[\frac{1}{\sin(\beta+\alpha)} - \frac{1}{\sin(\beta-\alpha)}\right]$$

$$= (+1) * |AC| * \cos(\alpha) * \frac{\cos(\theta)}{\sin(\theta+\alpha)}$$

$$* \left[\frac{1}{\cos(\theta)} - \frac{1}{\cos(\theta+2\alpha)}\right] \qquad \text{(A7)}$$

It can be seen from equations (18) and (19) that optical path difference is increasing linearly as we move away from the field center, with same amount but

opposite signs on opposite sides of the beam center. The magnitude of the OPD can be derived in terms of the exposure field size as follows

$$|\mathrm{OPD}| = |\mathrm{HJ}| * \frac{\cos(\alpha)}{\tan(\theta+\alpha)} * \left[\frac{1}{\cos(\theta)} - \frac{1}{\cos(\theta+2\alpha)}\right]$$

$$= |\mathrm{HJ}| * \mathrm{OPD}_{\mathrm{Coefficient}} \qquad (A8)$$

where $\mathrm{OPD}_{\mathrm{Coefficient}}$ is a lumped parameter that has angular dependencies. It should be also noted that the mirror tilt has a stronger effect on $\mathrm{OPD}_{\mathrm{Coefficient}}$ than the grating angle.

7. APPENDIX B

```
%% Uncomment below to calculate convolved images.
%% Last Edit:11/8/12 by Burak Baylav
clear all;
close all;
clc;
% Option 1: If want to filter out the noise in the initial image
  Q=imread('Amphibian full mod_Cont_25pLess.bmp'); % Load image
  T=double(rgb2gray(Q));
  wndwSize = 1;
  h = ones(1,wndwSize)/wndwSize;     % Moving average window
  R0 = filter(h,1,T);

% Enter the pixel size in nm as "scale" term below
scale=0.5; %pixel size

% The displacement functions are given below
% g1-Gaussian (~Triangular) type displacement
% g2-Sinusoidal type displacement
% g3-Uniform type displacement
% The size of the displacements (length of g's) is scale*lenght(g) (nm)
% Option 1: If want to have a short smearing, invoke below g's
% Option 2: If want to have a medium size smearing, invoke below g's
g1= [(1:131)';(130:-1:1)'];
g2= [(14:-2:2)'; ones(247,1); (2:2:14)'];
g3= ones(261,1);
disp('amount of P-P displacement (in nm) applied is:');
disp(length(g1)*scale);

% In order to make the original SEM same size with the convolved images
% need to remove some of its elements. Hence, R is the static image.
R=R0; R(1:(length(g1)+1)/2,:)=[]; R((end-(length(g1)+1)/2+1):end,:)=[];
figure(1); imagesc(R); % initial image

% Converting grayscale images to binary image (B/W)
% Assume a threshold brightness that is middle way between darkest and
% brightest pixel of the static image (50% Waveform Threshold)
THR=((max(max(R))+(min(min(R)))))/2;
H_R =R(:,:)>=THR;
k=1;
y_R=zeros(size(H_R,1),1);
for i=1:1:size(H_R,1);
    for j=1:1:size(H_R,2);
        if H_R(i,j)==1;
            y_R(k)=j;
            break;
        end
    end
     k=k+1;
end
```

```
unconv=detrend(y_R); %remove mean and trend in pixels
% Image rotation is performed here, if the SEM picture is tilted
tilt=(y_R-mean(y_R))-unconv;
tilt_angle=atan((max(tilt)-min(tilt))/size(tilt,1));
w=ceil(max(tilt)-min(tilt));
s=imrotate(R,sign(tilt(1))*tilt_angle*180/pi,'crop');
s(1:(w+1),:)=[];
s((end-w+1):end,:)=[];
s(:,1:(w+1))=[];
s(:,(end-w+1):end)=[];
s(:,(end-w+1):end)=[];
figure(2); imagesc(s); % tilt removed image

R=s; R(1:(length(g1)+1)/2,:)=[]; R((end-(length(g1)+1)/2+1):end,:)=[];

% Colvolving the original picture with some sample displacement
functions
% Also, some of the first and last elemnts are removed to discard
transient
P1=conv2(s,g1/sum(g1)); P1(1:length(g1),:)=[]; P1((end-
length(g1)+1):end,:)=[];
P2=conv2(s,g2/sum(g2)); P2(1:length(g2),:)=[]; P2((end-
length(g2)+1):end,:)=[];
P3=conv2(s,g3/sum(g3)); P3(1:length(g3),:)=[]; P3((end-
length(g3)+1):end,:)=[];

%converting grayscale images to binary image (B/W)
% Assume a threshold brightness that is middle way between darkest and
% brightest pixel of the static image (50% Waveform Threshold)
THR=((max(max(R))+(min(min(R)))))/2;
H_R =R(:,:)>=THR;
H_P1=P1(:,:)>=THR;
H_P2=P2(:,:)>=THR;
H_P3=P3(:,:)>=THR;

% Option 1: If want to see the effect of convolution for 3 different
displacments
figure(3); subplot(2,2,1); imshow(H_R); title('Static Image
(Is)','Fonts',16);hold on;
           subplot(2,2,2); imshow(H_P1);title('Gaussian Displ.
Image','Fonts',16);
           subplot(2,2,3); imshow(H_P2);title('Sinusoidal Displ.
Image','Fonts',16);
           subplot(2,2,4); imshow(H_P3);title('Uniform Displ.
Image','Fonts',16);
           hold off;

% Option 2: If want to see the effect of convolution for uniform
displacements
% figure(3); subplot(1,2,1); imshow(H_R); title('Static Image
(Is)','Fonts',16);hold on;
%            subplot(1,2,2); imshow(H_P3);title('Uniform Displ.
Image','Fonts',16);
%            hold off;

% Performing horizontal cutlines at center of each un/convolved image
```

```
cut_H_50_R=R(ceil(size(R,1)*0.50),ceil(size(R,2)*0.3):ceil(size(R,2)*0.
75));
cut_H_50_P1=P1(ceil(size(P1,1)*0.50),ceil(size(P1,2))*0.3:ceil(size(P1,
2))*0.75);
cut_H_50_P2=P2(ceil(size(P2,1)*0.50),ceil(size(P2,2))*0.3:ceil(size(P2,
2))*0.75);
cut_H_50_P3=P3(ceil(size(P3,1)*0.50),ceil(size(P3,2))*0.3:ceil(size(P3,
2))*0.75);

% Calculating cut lines
figure(4); plot(cut_H_50_R,'k','LineWidth',2); hold on; grid on;
           plot(cut_H_50_P1,'r','LineWidth',2);
           plot(cut_H_50_P2,'g','LineWidth',2);
           plot(cut_H_50_P3,'b','LineWidth',2); hold off; grid off;
           title('Cutline across the images','Fonts',16);
           legend('Static Image (Is)', 'Gaussian Disp.
Image','Sinusoidal Disp. Image','Uniform Disp. Image');
           set(legend,'FontSize',14);
           xlabel('Pixel indices along horizontal
direction','Fonts',16); ylabel('Pixel Brightness','Fonts',16);
% Calculating the normalized variance (wrt static image) for Columns
V_var_RN=var(R,1,1);
V_var_R=V_var_RN/max(V_var_RN);
V_var_P1=var(P1,1,1)/max(V_var_RN);
V_var_P2=var(P2,1,1)/max(V_var_RN);
V_var_P3=var(P3,1,1)/max(V_var_RN);
%Plotting the normalized standard deviations (wrt R) for Columns
figure (5); plot(sqrt(V_var_R),'k','LineWidth',2); hold on; grid on;
            plot(sqrt(V_var_P1),'r','LineWidth',2);
            plot(sqrt(V_var_P2),'g','LineWidth',2);
            plot(sqrt(V_var_P3),'b','LineWidth',2); hold off; grid off;
            title('Normalized pixel brightness std. dev. (wrt.
Is)','Fonts',16)
            legend('Static Image (Is)', 'Gaussian Disp.','Sinusoidal
Disp.','Uniform Disp.');
            set(legend,'FontSize',14);
            xlabel('Pixel indices along horizontal
direction','Fonts',16);
            ylabel('Standard Deviation (a.u.)','Fonts',16);

figure(6);   subplot(2,2,1); hist(V_var_R); title('Static Image
(Is)','Fonts',16); grid on;
             xlabel('Standard Deviation Bins','Fonts',16);
ylabel('Counts','Fonts',16);
             subplot(2,2,2); hist(V_var_P1);title('Gaussian Disp.
Image','Fonts',16); grid on;
             xlabel('Standard Deviation Bins','Fonts',16);
ylabel('Counts','Fonts',16);
             subplot(2,2,3); hist(V_var_P2);title('Sinusoidal Disp.
Image','Fonts',16); grid on;
             xlabel('Standard Deviation Bins','Fonts',16);
ylabel('Counts','Fonts',16);
             subplot(2,2,4); hist(V_var_P3);title('Uniform Disp.
Image','Fonts',16); grid on;
             xlabel('Standard Deviation Bins','Fonts',16);
ylabel('Counts','Fonts',16);
```

```
%% Uncomment Below to calculate the edge roughness.     Last
Edit:5/1/12
close all;
k=1;
y_R=zeros(size(H_R,1),1);
for i=1:1:size(H_R,1);
    for j=1:1:size(H_R,2);
        if H_R(i,j)==1;
            y_R(k)=j;
            break;
        end
    end
     k=k+1;
end
k=1;
y_P1=zeros(size(H_P1,1),1);
for i=1:1:size(H_P1,1);
    for j=1:1:size(H_P1,2);
        if H_P1(i,j)==1;
            y_P1(k)=j;
            break;
        end
    end
     k=k+1;
end
k=1;
y_P2=zeros(size(H_P2,1),1);
for i=1:1:size(H_P2,1);
    for j=1:1:size(H_P2,2);
        if H_P2(i,j)==1;
            y_P2(k)=j;
            break;
        end
    end
     k=k+1;
end
k=1;
y_P3=zeros(size(H_P3,1),1);
for i=1:1:size(H_P3,1);
    for j=1:1:size(H_P3,2);
        if H_P3(i,j)==1;
            y_P3(k)=j;
            break;
        end
    end
     k=k+1;
end
% Converting pixels into nm via multiplication of scale;
y_R=scale*y_R;
y_P1=scale*y_P1;
y_P2=scale*y_P2;
y_P3=scale*y_P3;

% Option 1:If remove the mean value and the trend (slope) from each of
them:
% for untilting purposes
% unconv=detrend(y_R-mean(y_R));
```

```
% conv_1=detrend(y_P1-mean(y_P1));
% conv_2=detrend(y_P2-mean(y_P2));
% conv_3=detrend(y_P3-mean(y_P3));

% Option 2: If remove just the mean value from each of them:
unconv=(y_R-mean(y_R));   %in nm
conv_1=(y_P1-mean(y_P1)); %in nm
conv_2=(y_P2-mean(y_P2)); %in nm
conv_3=(y_P3-mean(y_P3)); %in nm

% Image statistics in nm
Three_sigma_y_R=3*std(unconv);
Three_sigma_y_P1=3*std(conv_1);
Three_sigma_y_P2=3*std(conv_2);
Three_sigma_y_P3=3*std(conv_3);
Three_sigma_all=[Three_sigma_y_R, Three_sigma_y_P1, Three_sigma_y_P2,
Three_sigma_y_P3];
roughness_range_Y=max(unconv)+abs(min(unconv));
roughness_range_P1=max(conv_1)+abs(min(conv_1));
roughness_range_P2=max(conv_2)+abs(min(conv_2));
roughness_range_P3=max(conv_3)+abs(min(conv_3));
Roughness_all=[roughness_range_Y,
roughness_range_P1,roughness_range_P2, roughness_range_P3];
All_statistics=[Three_sigma_all; Roughness_all];
figure(7); bar(All_statistics,'Grouped'); grid on;
legend('Static Image','Gaussian Disp.','Sinusoidal Disp.','Uniform
Disp.');
set(legend,'FontSize',14);
title('3 Sigma LER (1) and Roughness Range (2)','fonts',18);
ylabel('Value (nm)','fonts',18);

% if want to use filtered (smoothened) data, uncomment below
% wndwSize = 20;
% h = ones(1,wndwSize)/wndwSize;      % equiv to a moving average
window
% unconv_smooth=filter(h, 1, unconv);
unconv_smooth(1:wndwSize)=[];unconv_smooth(end-wndwSize+1:end)=[];
% conv_1_smooth=filter(h, 1, conv_1);
conv_1_smooth(1:wndwSize)=[];conv_1_smooth(end-wndwSize+1:end)=[];
% conv_2_smooth=filter(h, 1, conv_2);
conv_2_smooth(1:wndwSize)=[];conv_2_smooth(end-wndwSize+1:end)=[];
% conv_3_smooth=filter(h, 1, conv_3);
conv_3_smooth(1:wndwSize)=[];conv_3_smooth(end-wndwSize+1:end)=[];
% unconv=unconv_smooth;
% conv_1=conv_1_smooth;
% conv_2=conv_2_smooth;
% conv_3=conv_3_smooth;


figure(8);
edge=(1:length(unconv))'*scale;
subplot(2,2,1); plot(edge,unconv,'-k*','MarkerSize',3,'LineWidth',1);
legend('Original LER')%hold on; plot(y_R_smooth,'-r','LineWidth',2);
%camroll(-90);
```

```
xlim([0,max(edge)/2]); ylim([-
(max(abs(unconv)))*1.2,(max(abs(unconv)))*1.2]); grid on; title('Static
Image LER','fonts',16);
xlabel('Edge Distance (nm)','fonts',16); ylabel('Roughness
(nm)','fonts',16);
subplot(2,2,2); plot(edge,conv_1,'-r*','MarkerSize',3,'LineWidth',1);
legend('Triangular VH LER')%hold on; plot(y_P1_smooth,'-
r','LineWidth',2);%camroll(-90);
xlim([0,max(edge)/2]); ylim([-
(max(abs(unconv)))*1.2,(max(abs(unconv)))*1.2]); grid on;
title('Gaussian Disp. LER','fonts',16);
xlabel('Edge Distance (nm)','fonts',16); ylabel('Roughness
(nm)','fonts',16);
subplot(2,2,3); plot(edge,conv_2,'-m*','MarkerSize',3,'LineWidth',1);
legend('Sinusoidal VH LER')%hold on; plot(y_P2_smooth,'-
r','LineWidth',2);%camroll(-90);
xlim([0,max(edge)/2]); ylim([-
(max(abs(unconv)))*1.2,(max(abs(unconv)))*1.2]); grid on;
title('Sinusoidal Disp. LER','fonts',16);
xlabel('Edge Distance (nm)','fonts',16); ylabel('Roughness
(nm)','fonts',16);
subplot(2,2,4); plot(edge,conv_3,'-b*','MarkerSize',3,'LineWidth',1);
legend('Uniform VH LER')%hold on; plot(y_P3_smooth,'-
r','LineWidth',2);%camroll(-90);
xlim([0,max(edge)/2]); ylim([-
(max(abs(unconv)))*1.2,(max(abs(unconv)))*1.2]); grid on;
title('Uniform Disp. LER','fonts',16);
xlabel('Edge Distance (nm)','fonts',16); ylabel('Roughness
(nm)','fonts',16);

%Overlay plot of all roughnesses is given below
figure(9);
plot(edge,unconv,'-ko','MarkerSize',3,'LineWidth',2); hold on;
plot(edge,conv_1,'-r*','MarkerSize',3,'LineWidth',2);
hold on; plot(edge,conv_2,'-mx','MarkerSize',3,'LineWidth',2);hold on;
plot(edge,conv_3,'-b+','MarkerSize',3,'LineWidth',2);
xlim([0,max(edge)/2]); ylim([-
(max(abs(unconv)))*1.2,(max(abs(unconv)))*1.2]); grid on; hold
on;plot(1:size(unconv,1),0,'LineWidth',4,'Color','r')
title('Overlay of Different Disp. LERs','fonts',18);
legend('Static Image LER','Gaussian Disp. LER','Sinusoidal Disp.
LER','Uniform Disp. LER');
set(legend,'FontSize',14);
xlabel('Edge Distance (nm)','fonts',18); ylabel('Roughness
(nm)','fonts',18);



%% Calculating PSD via Periodogram (preferred over Correlogram)  5/1/12
% Estimate the PSD
% 1) Trend should be removed from the data (mean=0)
close all;
NSAMP  = ceil(size(unconv,1)/4); % 2) Select segment length
NSHIFT = ceil(size(unconv,1)/100); % 3) Select shift between segments
% 4) Compute fft for each segment
% 5) Compute PSD by averaging fft values of each segment
S = zeros(1,NSAMP); %unconv
```

```
R = zeros(1,NSAMP); %conv_1
U = zeros(1,NSAMP); %conv_2
V = zeros(1,NSAMP); %conv_3
% for the unconv case
n1 = 1; n2 = n1 + NSAMP-1; k = 0;
while n2 <= size(unconv,1);
k = k+1;
S(k,:) = abs(fft(unconv(n1:n2))).^2;
R(k,:) = abs(fft(conv_1(n1:n2))).^2;
U(k,:) = abs(fft(conv_2(n1:n2))).^2;
V(k,:) = abs(fft(conv_3(n1:n2))).^2;
n1 = n1+NSHIFT;
n2 = n1+NSAMP-1;
end
S = S/NSAMP;
Savg = mean(S,1); %unconv
R = R/NSAMP;
Ravg = mean(R,1); %conv_1
U = U/NSAMP;
Uavg = mean(U,1); %conv_2
V = V/NSAMP;
Vavg = mean(V,1); %conv_3

f = 2*(0:NSAMP-1)/NSAMP/scale; %per nm
nf = floor(NSAMP/2);
figure(10);
loglog(f(1:nf),Savg(1:nf),'k','LineWidth',2);
hold on; loglog(f(1:nf),Ravg(1:nf),'r','LineWidth',2);
hold on; loglog(f(1:nf),Uavg(1:nf),'m','LineWidth',2);
hold on; loglog(f(1:nf),Vavg(1:nf),'b','LineWidth',2);
grid on;
title('LER PSD','fonts',18)
xlabel('Frequency','fonts',18)
ylabel('Power (a.u.)','fonts',18)
legend('Static Image LER','Gaussian Disp. LER','Sinusoidal Disp.
LER','Uniform Disp. LER');
set(legend,'FontSize',14);
% axis([0.01 1 0.001 1000]);
```

8. APPENDIX C

```
function burak_Zernike_FINAL_w_CostFunct(desiredPUPIL)
%Last edit: 04/24/2013 by Burak Baylav
% clc;
% close all;
% clear all;
resol=1/((size(desiredPUPIL,1)-1)/2);
[X,Y] = meshgrid(-1:(resol):1,-1:(resol):1);
costfilter=double(abs(X)<=1&abs(Y)<=1); % for no cost function
%costfilter=double(abs(X)>=0.28 & abs(X)<=0.76 & abs(Y)<=1); % cost
filter for 500nm period
[a,r] = cart2pol(X,Y);
% filter=double(r<=1);
filter=costfilter.*double(r<=1);% maybe I can use these filters for
assigning weight on cost function across pupil locations

% % Select Zernike's to be fitted here:
% S4=1;   S5=1;   S6=1;   S7=1;   S8=1;   S9=1;   S10=1;  S11=1;
% S12=1;  S13=1;  S14=1;  S15=1;  S16=1;  S17=1;  S18=1;  S19=1;
% S20=1;  S21=1;  S22=1;  S23=1;  S24=1;  S25=1;  S26=1;  S27=1;
% S28=1;  S29=1;  S30=1;  S31=1;  S32=1;  S33=1;  S34=1;  S35=1;
% S36=1;  S37=1;  S38=1;  S39=1;  S40=1;  S41=1;  S42=1;  S43=1;
% S44=1;  S45=1;  S46=1;  S47=0;  S48=0;  S49=1;  S50=1;  S51=1;
% S52=1;  S53=1;  S54=1;  S55=1;  S56=1;  S57=1;  S58=1;  S59=1;
% S60=1;  S61=1;  S62=1;  S63=1;  S64=1;
% %%%%%%%%%%%%%%

% Select Zernike's to be fitted here:
S4=1;   S5=1;   S6=1;   S7=1;   S8=1;   S9=1;   S10=1;  S11=1;
S12=1;  S13=1;  S14=1;  S15=1;  S16=1;  S17=1;  S18=1;  S19=1;
S20=1;  S21=1;  S22=1;  S23=1;  S24=1;  S25=1;  S26=1;  S27=1;
S28=1;  S29=1;  S30=1;  S31=1;  S32=1;  S33=1;  S34=1;  S35=1;
S36=1;  S37=1;  S38=0;  S39=0;  S40=0;  S41=0;  S42=0;  S43=0;
S44=0;  S45=0;  S46=0;  S47=0;  S48=0;  S49=0;  S50=0;  S51=0;
S52=0;  S53=0;  S54=0;  S55=0;  S56=0;  S57=0;  S58=0;  S59=0;
S60=0;  S61=0;  S62=0;  S63=0;  S64=0;
%%%%%%%%%%%%%%%


% Define Zernikes below,
Z4=2*(r.^2)-1;  a4=0;
Z5=(r.^2).*cos(2*a);    a5=0;
Z6=(r.^2).*sin(2*a);    a6=0;
Z7=(3*(r.^3)-2*r).*cos(a);  a7=0;
Z8=(3*(r.^3)-2*r).*sin(a);  a8=0;
Z9=(6*(r.^4)-6*(r.^2))+1; a9=0;
Z10=(r.^3).*cos(3*a);   a10=0;
Z11=(r.^3).*sin(3*a);   a11=0;
Z12=(4*(r.^4)-3*(r.^2)).*cos(2*a);  a12=0;
Z13=(4*(r.^4)-3*(r.^2)).*sin(2*a);  a13=0;
```

```
Z14=(10*(r.^5)-12*(r.^3)+3*r).*cos(a);  a14=0;
Z15=(10*(r.^5)-12*(r.^3)+3*r).*sin(a);  a15=0;
Z16=20*(r.^6)-30*(r.^4)+12*r.^2-1;  a16=0;
Z17=(r.^4).*cos(4*a);   a17=0;
Z18=(r.^4).*sin(4*a);   a18=0;
Z19=(5*(r.^5)-4*(r.^3)).*cos(3*a);  a19=0;
Z20=(5*(r.^5)-4*(r.^3)).*sin(3*a);  a20=0;
Z21=(15*(r.^6)-20*(r.^4)+6*(r.^2)).*cos(2*a);   a21=0;
Z22=(15*(r.^6)-20*(r.^4)+6*(r.^2)).*sin(2*a);   a22=0;
Z23=(35*(r.^7)-60*(r.^5)+30*(r.^3)-4*r).*cos(a);    a23=0;
Z24=(35*(r.^7)-60*(r.^5)+30*(r.^3)-4*r).*sin(a);    a24=0;
Z25=70*r.^8-140*r.^6+90*r.^4-20*r.^2+1; a25=0;
Z26=r.^5.*cos(5*a); a26=0;
Z27=r.^5.*sin(5*a); a27=0;
Z28=(6*(r.^6)-5*(r.^4)).*cos(4*a);  a28=0;
Z29=(6*(r.^6)-5*(r.^4)).*sin(4*a);  a29=0;
Z30=(21*(r.^7)-30*(r.^5)+10*(r.^3)).*cos(3*a);  a30=0;
Z31=(21*(r.^7)-30*(r.^5)+10*(r.^3)).*sin(3*a);  a31=0;
Z32=(56*(r.^8)-105*(r.^6)+60*(r.^4)-10*(r.^2)).*cos(2*a);   a32=0;
Z33=(56*(r.^8)-105*(r.^6)+60*(r.^4)-10*(r.^2)).*sin(2*a);   a33=0;
Z34=(126*(r.^9)-280*(r.^7)+210*(r.^5)-60*(r.^3)+5*r).*cos(a);   a34=0;
Z35=(126*(r.^9)-280*(r.^7)+210*(r.^5)-60*(r.^3)+5*r).*sin(a);   a35=0;
Z36=252*(r.^10)-630*(r.^8)+560*(r.^6)-210*(r.^4)+30*(r.^2)-1;   a36=0;
Z37=(r.^6).*cos(6*a);   a37=0;
Z38=(r.^6).*sin(6*a);   a38=0;
Z39=(r.^5).*(-6+7*(r.^2)).*cos(5*a);   a39=0;
Z40=(r.^5).*(-6+7*(r.^2)).*sin(5*a);   a40=0;
Z41=(r.^4).*(15-42*(r.^2)+28*(r.^4)).*cos(4*a);   a41=0;
Z42=(r.^4).*(15-42*(r.^2)+28*(r.^4)).*sin(4*a);   a42=0;
Z43=(r.^3).*(-20+105*(r.^2)-168*(r.^4)+84*(r.^6)).*cos(3*a);   a43=0;
Z44=(r.^3).*(-20+105*(r.^2)-168*(r.^4)+84*(r.^6)).*sin(3*a);   a44=0;
Z45=(r.^2).*(15-140*(r.^2)+420*(r.^4)-504*(r.^6)+210*(r.^8)).*cos(2*a);
a45=0;
Z46=(r.^2).*(15-140*(r.^2)+420*(r.^4)-504*(r.^6)+210*(r.^8)).*sin(2*a);
a46=0;
Z47=r.*(-6+105*(r.^2)-560*(r.^4)+126*(r.^6)-
1260*(r.^8)+462*(r.^10)).*cos(a);   a47=0;
Z48=r.*(-6+105*(r.^2)-560*(r.^4)+126*(r.^6)-
1260*(r.^8)+462*(r.^10)).*sin(a);   a48=0;
Z49=1-42*(r.^2)+420*(r.^4)-1680*(r.^6)+3150*(r.^8)-
2772*(r.^10)+924*(r.^12);   a49=0;
Z50=(r.^7).*cos(7*a);   a50=0;
Z51=(r.^7).*sin(7*a);   a51=0;
Z52=(r.^6).*(-7+8*(r.^2)).*cos(6*a);   a52=0;
Z53=(r.^6).*(-7+8*(r.^2)).*sin(6*a);   a53=0;
Z54=(r.^5).*(21-56*(r.^2)+36*(r.^4)).*cos(5*a);   a54=0;
Z55=(r.^5).*(21-56*(r.^2)+36*(r.^4)).*sin(5*a);   a55=0;
Z56=(r.^4).*(-35+168*(r.^2)-252*(r.^4)+120*(r.^6)).*cos(4*a);   a56=0;
Z57=(r.^4).*(-35+168*(r.^2)-252*(r.^4)+120*(r.^6)).*sin(4*a);   a57=0;
Z58=(r.^3).*(35-280*(r.^2)+756*(r.^4)-840*(r.^6)+330*(r.^8)).*cos(3*a);
a58=0;
Z59=(r.^3).*(35-280*(r.^2)+756*(r.^4)-840*(r.^6)+330*(r.^8)).*sin(3*a);
a59=0;
Z60=(r.^2).*(-21+280*(r.^3)-1260*(r.^4)+2520*(r.^6)-
2310*(r.^8)+792*(r.^10)).*cos(2*a);   a60=0;
Z61=(r.^2).*(-21+280*(r.^3)-1260*(r.^4)+2520*(r.^6)-
2310*(r.^8)+792*(r.^10)).*sin(2*a);   a61=0;
```

```
Z62=r.*(7-168*(r.^2)+1260*(r.^4)-4200*(r.^6)+6930*(r.^8)-
5544*(r.^10)+1716*(r.^12)).*cos(a);   a62=0;
Z63=r.*(7-168*(r.^2)+1260*(r.^4)-4200*(r.^6)+6930*(r.^8)-
5544*(r.^10)+1716*(r.^12)).*sin(a);   a63=0;
Z64=-1+56*(r.^2)-756*(r.^4)+4200*(r.^6)-11550*(r.^8)+16632*(r.^10)-
12012*(r.^12)+3432*(r.^14);   a64=0;

simPUPIL=zeros(size(X,2),size(Y,1));
lowlim=-0.1; highlim=0.1; res=0.01;  kk=(lowlim:res:highlim);

%%%%%%%%%%%%%%%%%%%%%%%%%%%%%%
if S4==1; % optimization for Z4 is wanted, otherwise a4=0;
k=1; Error=zeros(1,length(kk));
for a4=(lowlim:res:highlim);
    simPUPIL=a4*Z4+a5*Z5+a6*Z6+a7*Z7+a8*Z8+a9*Z9+a10*Z10 ...

+a11*Z11+a12*Z12+a13*Z13+a14*Z14+a15*Z15+a16*Z16+a17*Z17+a18*Z18+a19*Z1
9+a20*Z20 ...

+a21*Z21+a22*Z22+a23*Z23+a24*Z24+a25*Z25+a26*Z26+a27*Z27+a28*Z28+a29*Z2
9+a30*Z30 ...

+a31*Z31+a32*Z32+a33*Z33+a34*Z34+a35*Z35+a36*Z36+a37*Z37+a38*Z38+a39*Z3
9+a40*Z40 ...

+a41*Z41+a42*Z42+a43*Z43+a44*Z44+a45*Z45+a46*Z46+a47*Z47+a48*Z48+a49*Z4
9+a50*Z50 ...

+a51*Z51+a52*Z52+a53*Z53+a54*Z54+a55*Z55+a56*Z56+a57*Z57+a58*Z58+a59*Z5
9+a60*Z60 ...
    +a61*Z61+a62*Z62+a63*Z63+a64*Z64;
    diffPUPIL=filter.*(simPUPIL)-filter.*(desiredPUPIL);
    Error(k)=sqrt(mean(diffPUPIL(:).^2));
    k=k+1;
end
[~,I]=min(Error);
a4=lowlim+(I-1)*res; % optimum a4 is found
end
%%%%%%%%%%%%%%%%%%%%%%%%%%%%% Section Z start %%%%%
if S5==1;
k=1; Error=zeros(1,length(kk));
for a5=(lowlim:res:highlim);
    simPUPIL=a4*Z4+a5*Z5+a6*Z6+a7*Z7+a8*Z8+a9*Z9+a10*Z10 ...

+a11*Z11+a12*Z12+a13*Z13+a14*Z14+a15*Z15+a16*Z16+a17*Z17+a18*Z18+a19*Z1
9+a20*Z20 ...

+a21*Z21+a22*Z22+a23*Z23+a24*Z24+a25*Z25+a26*Z26+a27*Z27+a28*Z28+a29*Z2
9+a30*Z30 ...

+a31*Z31+a32*Z32+a33*Z33+a34*Z34+a35*Z35+a36*Z36+a37*Z37+a38*Z38+a39*Z3
9+a40*Z40 ...

+a41*Z41+a42*Z42+a43*Z43+a44*Z44+a45*Z45+a46*Z46+a47*Z47+a48*Z48+a49*Z4
9+a50*Z50 ...
```

```
+a51*Z51+a52*Z52+a53*Z53+a54*Z54+a55*Z55+a56*Z56+a57*Z57+a58*Z58+a59*Z5
9+a60*Z60 ...
    +a61*Z61+a62*Z62+a63*Z63+a64*Z64;
    diffPUPIL=filter.*(simPUPIL)-filter.*(desiredPUPIL);
    Error(k)=sqrt(mean(diffPUPIL(:).^2));
    k=k+1;
end
[~,I]=min(Error);
a5=lowlim+(I-1)*res; % optimum a5 found
end
%%%%%%%%%%%%%%%%%%%%%%%%%%%%%%%%% Section Z end %%%%%
```

Section Z repeated for Zernikes Z6 through Z63

```
%%%%%%%%%%%%%%%%%%%%%%%%%%%%%%%%%
if S64==1;
k=1; Error=zeros(1,length(kk));
for a64=(lowlim:res:highlim);
    simPUPIL=a4*Z4+a5*Z5+a6*Z6+a7*Z7+a8*Z8+a9*Z9+a10*Z10 ...

+a11*Z11+a12*Z12+a13*Z13+a14*Z14+a15*Z15+a16*Z16+a17*Z17+a18*Z18+a19*Z1
9+a20*Z20 ...

+a21*Z21+a22*Z22+a23*Z23+a24*Z24+a25*Z25+a26*Z26+a27*Z27+a28*Z28+a29*Z2
9+a30*Z30 ...

+a31*Z31+a32*Z32+a33*Z33+a34*Z34+a35*Z35+a36*Z36+a37*Z37+a38*Z38+a39*Z3
9+a40*Z40 ...

+a41*Z41+a42*Z42+a43*Z43+a44*Z44+a45*Z45+a46*Z46+a47*Z47+a48*Z48+a49*Z4
9+a50*Z50 ...

+a51*Z51+a52*Z52+a53*Z53+a54*Z54+a55*Z55+a56*Z56+a57*Z57+a58*Z58+a59*Z5
9+a60*Z60 ...
    +a61*Z61+a62*Z62+a63*Z63+a64*Z64;
    diffPUPIL=filter.*(simPUPIL)-filter.*(desiredPUPIL);
    Error(k)=sqrt(mean(diffPUPIL(:).^2));
    k=k+1;
end
[ss,I]=min(Error);
a64=lowlim+(I-1)*res; % optimum a64 found
end
%%%%%%%%%%%%%%%%%%%%%%%%%%%%%%%%%

        fprintf('Coefficient of Z4 is %6.3f \n', a4)
        fprintf('Coefficient of Z5 is %6.3f \n', a5)
        fprintf('Coefficient of Z6 is %6.3f \n', a6)
        fprintf('Coefficient of Z7 is %6.3f \n', a7)
        fprintf('Coefficient of Z8 is %6.3f \n', a8)
        fprintf('Coefficient of Z9 is %6.3f \n', a9)
        fprintf('Coefficient of Z10 is %6.3f \n', a10)
        fprintf('Coefficient of Z11 is %6.3f \n', a11)
        fprintf('Coefficient of Z12 is %6.3f \n', a12)
        fprintf('Coefficient of Z13 is %6.3f \n', a13)
```

```
fprintf('Coefficient of Z14 is %6.3f \n', a14)
fprintf('Coefficient of Z15 is %6.3f \n', a15)
fprintf('Coefficient of Z16 is %6.3f \n', a16)
fprintf('Coefficient of Z17 is %6.3f \n', a17)
fprintf('Coefficient of Z18 is %6.3f \n', a18)
fprintf('Coefficient of Z19 is %6.3f \n', a19)
fprintf('Coefficient of Z20 is %6.3f \n', a20)
fprintf('Coefficient of Z21 is %6.3f \n', a21)
fprintf('Coefficient of Z22 is %6.3f \n', a22)
fprintf('Coefficient of Z23 is %6.3f \n', a23)
fprintf('Coefficient of Z24 is %6.3f \n', a24)
fprintf('Coefficient of Z25 is %6.3f \n', a25)
fprintf('Coefficient of Z26 is %6.3f \n', a26)
fprintf('Coefficient of Z27 is %6.3f \n', a27)
fprintf('Coefficient of Z28 is %6.3f \n', a28)
fprintf('Coefficient of Z29 is %6.3f \n', a29)
fprintf('Coefficient of Z30 is %6.3f \n', a30)
fprintf('Coefficient of Z31 is %6.3f \n', a31)
fprintf('Coefficient of Z32 is %6.3f \n', a32)
fprintf('Coefficient of Z33 is %6.3f \n', a33)
fprintf('Coefficient of Z34 is %6.3f \n', a34)
fprintf('Coefficient of Z35 is %6.3f \n', a35)
fprintf('Coefficient of Z36 is %6.3f \n', a36)
fprintf('Coefficient of Z37 is %6.3f \n', a37)
fprintf('Coefficient of Z38 is %6.3f \n', a38)
fprintf('Coefficient of Z39 is %6.3f \n', a39)
fprintf('Coefficient of Z40 is %6.3f \n', a40)
fprintf('Coefficient of Z41 is %6.3f \n', a41)
fprintf('Coefficient of Z42 is %6.3f \n', a42)
fprintf('Coefficient of Z43 is %6.3f \n', a43)
fprintf('Coefficient of Z44 is %6.3f \n', a44)
fprintf('Coefficient of Z45 is %6.3f \n', a45)
fprintf('Coefficient of Z46 is %6.3f \n', a46)
fprintf('Coefficient of Z47 is %6.3f \n', a47)
fprintf('Coefficient of Z48 is %6.3f \n', a48)
fprintf('Coefficient of Z49 is %6.3f \n', a49)
fprintf('Coefficient of Z50 is %6.3f \n', a50)
fprintf('Coefficient of Z51 is %6.3f \n', a51)
fprintf('Coefficient of Z52 is %6.3f \n', a52)
fprintf('Coefficient of Z53 is %6.3f \n', a53)
fprintf('Coefficient of Z54 is %6.3f \n', a54)
fprintf('Coefficient of Z55 is %6.3f \n', a55)
fprintf('Coefficient of Z56 is %6.3f \n', a56)
fprintf('Coefficient of Z57 is %6.3f \n', a57)
fprintf('Coefficient of Z58 is %6.3f \n', a58)
fprintf('Coefficient of Z59 is %6.3f \n', a59)
fprintf('Coefficient of Z60 is %6.3f \n', a60)
fprintf('Coefficient of Z61 is %6.3f \n', a61)
fprintf('Coefficient of Z62 is %6.3f \n', a62)
fprintf('Coefficient of Z63 is %6.3f \n', a63)
fprintf('Coefficient of Z64 is %6.3f \n', a64)

    simPUPIL=a4*Z4+a5*Z5+a6*Z6+a7*Z7+a8*Z8+a9*Z9+a10*Z10 ...

+a11*Z11+a12*Z12+a13*Z13+a14*Z14+a15*Z15+a16*Z16+a17*Z17+a18*Z18+a19*Z1
9+a20*Z20 ...
```

```
+a21*Z21+a22*Z22+a23*Z23+a24*Z24+a25*Z25+a26*Z26+a27*Z27+a28*Z28+a29*Z2
9+a30*Z30 ...

+a31*Z31+a32*Z32+a33*Z33+a34*Z34+a35*Z35+a36*Z36+a37*Z37+a38*Z38+a39*Z3
9+a40*Z40 ...

+a41*Z41+a42*Z42+a43*Z43+a44*Z44+a45*Z45+a46*Z46+a47*Z47+a48*Z48+a49*Z4
9+a50*Z50 ...

+a51*Z51+a52*Z52+a53*Z53+a54*Z54+a55*Z55+a56*Z56+a57*Z57+a58*Z58+a59*Z5
9+a60*Z60 ...
    +a61*Z61+a62*Z62+a63*Z63+a64*Z64;
  filter=double(r<=1);
                finalPUPIL=(filter.*simPUPIL);
                diffPUPIL=filter.*(desiredPUPIL)-filter.*(simPUPIL);
RMSsimPUPIL=std(finalPUPIL(:))
RMSdesiredPUPIL=std(desiredPUPIL(:))
RMSerror=std(diffPUPIL(:))
figure;
      subplot(1,2,1); surf(X,Y,(filter.*desiredPUPIL));
      subplot(1,2,2); surf(X,Y,finalPUPIL);
```

9. REFERENCES

[1] "*Intel 22nm Technology*". Available: http://www.intel.com/content/www/us/en/silicon-innovations/intel-22nm-technology.html

[2] *"Intel Backgrounder-Over 6 Decades of Continued Transistor Shrinkage, Innovation"*. Available: http://download.intel.com/newsroom/kits/22nm/pdfs/Intel_Transistor_Backgrounder.pdf,.

[3] C. A. Mack, *Fundamental principles of optical lithography : the science of microfabrication*. Chichester, West Sussex, England ; Hoboken, NJ, USA: Wiley, 2007.

[4] G. E. Moore, "Lithography and the future of Moore's law," in *Proc. SPIE 2438, Advances in Resist Technology and Processing XII*, Santa Clara, Ca, pp. 2-17, 1995.

[5] K. Suzuki and B. W. Smith, *Microlithography : science and technology*, 2nd ed. Boca Raton: CRC Press, 2007.

[6] L. Rayleigh, "On the Theory of Optical Images, with special reference to the Microscope," *Journal of the Royal Microscopical Society,* vol. 23, pp. 474-482, 1903.

[7] F. M. Schellenberg, *Selected papers on resolution enhancement techniques in optical lithography*. Bellingham, Wash.: SPIE Press, 2004.

[8] A. K.-K. Wong, *Resolution enhancement techniques in optical lithography*. Bellingham, Wash.: SPIE Press, 2001.

[9] N. B. Cobb, A. Zakhor, M. Reihani, F. Jahansooz, and V. N. Raghavan, "Experimental results on optical proximity correction with variable-threshold resist model," in *Proc. SPIE 3051, Optical Microlithography X*, pp. 458-468, 1997.

[10] O. W. Otto, J. G. Garofalo, K. K. Low, C.-M. Yuan, R. C. Henderson, C. Pierrat, *et al.*, "Automated optical proximity correction: a rules-based approach," in *Proc. SPIE 2197, Optical/Laser Microlithography VII*, 1994, pp. 278-293.

[11] M. D. Levenson, N. S. Viswanathan, and R. A. Simpson, "Improving resolution in photolithography with a phase-shifting mask," *Electron Devices, IEEE Transactions on Electron Devices,* vol. 29, pp. 1828-1836, 1982.

[12] T. A. Brunner, "Rim phase-shift mask combined with off-axis illumination: a path to 0.5(lambda)/numerical aperture geometries," *Optical Engineering,* vol. 32, pp. 2337-2343, 1993.

[13] W. N. Partlo, P. J. Tompkins, P. G. Dewa, and P. F. Michaloski, "Depth of focus and resolution enhancement of i-line and deep-UV lithography using annular illumination," in *Proc. SPIE 1927, Optical/Laser Microlithography*, pp. 137-157, 1993.

[14] D. Melville, A. E. Rosenbluth, K. Tian, K. Lai, S. Bagheri, J. Tirapu-Azpiroz*, et al.*, "Demonstrating the benefits of source-mask optimization and enabling

technologies through experiment and simulations," in *Proc. SPIE 7640, Optical Microlithography XXIII*, pp. 764006-764006-18, 2010.

[15] X. Ma and G. R. Arce, "Pixel-based simultaneous source and mask optimization for resolution enhancement in optical lithography," *Optics Express, Vol. 17, Issue 7, pp. 5783-5793,* 2009.

[16] P. Xie, "Scanning evanescent wave lithography for sub-22 nm generations," *ProQuest Dissertations and Theses* pp. 144. 2012. ISBN: 9781267889591

[17] J. d. Klerk, C. Wagner, R. Droste, L. Levasier, L. Jorritsma, E. v. Setten*, et al.*, "Performance of a 1.35NA ArF immersion lithography system for 40nm applications," in *Proc. SPIE 6520, Optical Microlithography XX*, San Jose, CA, pp. Y5201-Y5201, 2007.

[18] B. Baylav, A. Estroff, P. Xie, and B. W. Smith, "Line edge roughness (LER) mitigation studies specific to interference-like lithography," in *Proc. SPIE 8683, Optical Microlithography XXVI*, pp. 86831Y-86831Y-12, 2013.

[19] B. Baylav, C. Maloney, Z. Levinson, J. Bekaert, A. V. Pret, and B. W. Smith, "Impact of pupil plane filtering on mask roughness transfer," *Journal of Vacuum Science & Technology B, 31, 06F801,* 2013.

[20] A. Miyaji, K. Suzuki, and A. Tanimoto, "Excimer lithography for ULSI," *Optical and Quantum Electronics,* vol. 25, pp. 297-310, 1993.

[21] K. Jain, *Excimer laser lithography*: Bellingham, WA (USA); SPIE Society of Photo-Optical Instrumentation Engineers, 1990.

[22] H. Mizoguchi, O. Wakabayashi, N. Ito, M. Kowaka, J. Fujimoto, Y. Kobayashi*, et al.*, "Narrow band KrF excimer laser for mass production of ULSI ICs," in *Proc. SPIE 1674, Optical/Laser Microlithography V*, pp. 532-542, 1992.

[23] N. Furuya, T. Ono, N. Horiuchi, K. Yamanaka, and T. Miyata, "High-power and narrow-band excimer laser with a polarization-coupled resonator," in *Proc. SPIE 1264, Optical/Laser Microlithography III*, pp. 520-531, 1990.

[24] O. Wakabayashi, M. Kowaka, and Y. Kobayashi, "High-average-power narrow-band KrF excimer laser," in *Proc. SPIE 1463, Optical/Laser Microlithography IV*, pp. 617-628, 1991.

[25] P. Lokai, U. Rebhan, U. Stamm, H. Buecher, H.-J. Kahlert, and D. Basting, "High-spectral-brightness 1.0-pm bandwidth DUV lithography excimer laser," in *Proc. SPIE 1674, Optical/Laser Microlithography V*, pp. 669-680, 1992.

[26] R. K. Brimacombe, T. J. McKee, E. D. Mortimer, B. Norris, J. Reid, and T. A. Znotins, "Performance Characteristics Of A Narrow Band Industrial Excimer Laser," in *Proc. SPIE 1088, Optical/Laser Microlithography II*, pp. 416-423, 1989.

[27] R. L. Sandstrom, "Measurements of beam characteristics relevant to DUV microlithography on a KrF excimer laser," in *Proc. SPIE 1264, Optical/Laser Microlithography III*, pp. 505-519, 1990.

[28] T. Ishihara, R. L. Sandstrom, C. Reiser, and U. K. Sengupta, "Advanced krypton fluoride excimer laser for microlithography," in *Proc. SPIE 1674, Optical/Laser Microlithography V*, pp. 473-485, 1992.

[29] T. E. Jewell, J. H. Bennewitz, G. C. Escher, and V. Pol, "Effect Of Laser Characteristics On The Performance Of A Deep UV Projection System," in *Proc. SPIE 0774, Lasers in Microlithography*, pp. 124-132, 1987.

[30] Y. Ichihara, S. Kawata, I. Hikima, M. Hamatani, Y. Kudoh, and A. Tanimoto, "Illumination System Of An Excimer Laser Stepper," in *Proc. SPIE 1138, Optical Microlithography and Metrology for Microcircuit Fabrication*, pp. 137-145, 1989.
[31] *Excimer Laser Basics*. Available:
http://www.gamlaser.com/excimer_laser_basics.htm
[32] *ITRS 2011 Edition*. Available:
http://www.itrs.net/Links/2011ITRS/2011Chapters/2011Lithography.pdf
[33] A. J. Hazelton, S. Wakamoto, M. McCallum, N. Magome, C. Lapeyre, I. Guilmeau*, et al.*, "Double-patterning requirements for optical lithography and prospects for optical extension without double patterning," *Journal of Micro/Nanolithography, MEMS, and MOEMS,* vol. 8, pp. 011003-011003-11, 2009.
[34] C. Bencher, Y. Chen, H. Dai, W. Montgomery, and L. Huli, "22nm half-pitch patterning by CVD spacer self alignment double patterning (SADP)," in *Proc. SPIE 6924, Optical Microlithography XXI*, pp. 69244E-69244E-7, 2008.
[35] B. J. Lin, "NGL comparable to 193-nm lithography in cost, footprint, and power consumption," *Microelectronic Engineering,* vol. 86, pp. 442-447, Apr-Jun 2009.
[36] M. Dusa, J. Quaedackers, O. F. A. Larsen, J. Meessen, E. v. d. Heijden, G. Dicker*, et al.*, "Pitch doubling through dual-patterning lithography challenges in integration and litho budgets," in *Proc. SPIE 6520, Optical Microlithography XX*, pp. 65200G-65200G-10, 2007.
[37] K. Ronse, P. Jansen, R. Gronheid, E. Hendrickx, M. Maenhoudt, V. Wiaux*, et al.*, "Lithography Options for the 32 nm Half Pitch Node and Beyond," *Circuits and Systems I: Regular Papers, IEEE Transactions on,* vol. 56, pp. 1884-1891, 2009.
[38] C. Bencher, H. Dai, and Y. Chen, "Gridded design rule scaling: taking the CPU toward the 16nm node," in *SPIE Advanced Lithography*, pp. 72740G-72740G-10, 2009.
[39] P. Zimmerman, "Double patterning lithography: double the trouble or double the fun?," *SPIE Newsroom 20,* 2009.
[40] *The Nikon eReview: Lithography Basics: Extreme UltraViolet Lithography (EUVL) Technology*. Available:
http://www.nikonprecision.com/newsletter/fall_2008/article_05.html
[41] P. J. Silverman, "Extreme ultraviolet lithography: overview and development status," *Journal of Micro/Nanolithography, MEMS, and MOEMS,* vol. 4, pp. 011006-011006-5, 2005.
[42] B. Wu and A. Kumar, "Extreme ultraviolet lithography: A review," *Journal of Vacuum Science & Technology B: Microelectronics and Nanometer Structures,* vol. 25, pp. 1743-1761, 2007.
[43] P. P. Naulleau, C. N. Anderson, L.-M. Baclea-an, P. Denham, S. George, K. A. Goldberg*, et al.*, "Critical challenges for EUV resist materials," in *Proc. SPIE 7972, Advances in Resist Materials and Processing Technology XXVIII*, pp. 797202-797202-10, 2011.
[44] H. I. Smith, R. Menon, A. Patel, D. Chao, M. Walsh, and G. Barbastathis, "Zone-plate-array lithography: A low-cost complement or competitor to scanning-

electron-beam lithography," *Microelectronic Engineering,* vol. 83, pp. 956-961, 2006.

[45] S. Matsui and Y. Ochiai, "Focused ion beam applications to solid state devices," *Nanotechnology,* vol. 7, pp. 247-258, 1996.

[46] S. Reyntjens and R. Puers, "A review of focused ion beam applications in microsystem technology," *J. Micromech. Microeng.* ***11*** *287,* 2001.

[47] C. R. K. Marrian, E. A. Dobisz, and J. A. Dagata, "Electron-beam lithography with the scanning tunneling microscope," *Journal of Vacuum Science & Technology B: Microelectronics and Nanometer Structures,* vol. 10, pp. 2877-2881, 1992.

[48] R. F. W. Pease, "Electron beam lithography," *Contemporary Physics,* vol. 22, pp. 265-290, 1981.

[49] E. Platzgummer, "Maskless lithography and nanopatterning with electron and ion multibeam projection," in *Proc. SPIE 7637, Alternative Lithographic Technologies II*, pp. 763703-763703-12, 2010.

[50] E. Slot, M. J. Wieland, G. d. Boer, P. Kruit, G. F. t. Berge, A. M. C. Houkes*, et al.*, "MAPPER: high throughput maskless lithography," in *Proc. SPIE 6921, Emerging Lithographic Technologies XII*, pp. 69211P-69211P-9, 2008.

[51] M. J. Wieland, G. d. Boer, G. F. t. Berge, R. Jager, T. v. d. Peut, J. J. M. Peijster*, et al.*, "MAPPER: high-throughput maskless lithography," in *Proc. SPIE 7271, Alternative Lithographic Technologies*, pp. 72710O-72710O-8, 2009.

[52] C. Klein, J. Klikovits, L. Szikszai, E. Platzgummer, and H. Loeschner, "50 keV electron-beam projection maskless lithography (PML2): results obtained with 2,500 programmable 12.5-nm sized beams," in *Proc. SPIE 7637, Alternative Lithographic Technologies II*, pp. 76370B-76370B-6, 2010.

[53] P. Petric, C. Bevis, A. Carroll, H. Percy, M. Zywno, K. Standiford*, et al.*, "REBL: A novel approach to high speed maskless electron beam direct write lithography," *Journal of Vacuum Science & Technology B: Microelectronics and Nanometer Structures,* vol. 27, pp. 161-166, 2009.

[54] S. Y. Chou, P. R. Krauss, and P. J. Renstrom, "Nanoimprint lithography," *Journal of Vacuum Science & Technology B: Microelectronics and Nanometer Structures,* vol. 14, 1996.

[55] M. Colburn, S. C. Johnson, M. D. Stewart, S. Damle, T. C. Bailey, B. Choi*, et al.*, "Step and flash imprint lithography: a new approach to high-resolution patterning," in *Proc. SPIE 3676, Emerging Lithographic Technologies III*, pp. 379-389, 1999.

[56] H. Gao, H. Tan, W. Zhang, K. Morton, and S. Y. Chou, "Air Cushion Press for Excellent Uniformity, High Yield, and Fast Nanoimprint Across a 100 mm Field," *Nano Letters,* vol. 6, pp. 2438-2441, 2006.

[57] C. J. Hawker and T. P. Russell, "Block Copolymer Lithography: Merging “Bottom-Up” with “Top-Down” Processes," *MRS Bulletin,* vol. 30, pp. 952-966, 2005.

[58] T. R. Younkin, R. Gronheid, P. R. Delgadillo, B. T. Chan, N. Vandenbroeck, S. Demuynck*, et al.*, "Progress in directed self-assembly hole shrink applications," in *Proc. SPIE 8682, Advances in Resist Materials and Processing Technology XXX*, pp. 86820L-86820L-11, 2013.

[59] Y. Seino, H. Yonemitsu, H. Sato, M. Kanno, H. Kato, K. Kobayashi*, et al.*, "Contact hole shrink process using directed self-assembly," in *Proc. SPIE 8323, Alternative Lithographic Technologies IV*, pp. 83230Y-83230Y-7, 2012.
[60] S. B. Darling, "Directing the self-assembly of block copolymers," *Progress in Polymer Science,* vol. 32, pp. 1152-1204, 2007.
[61] L. Oria, A. R. d. Luzuriaga, X. Chevalier, J. A. Alduncin, D. Mecerreyes, R. Tiron*, et al.*, "Guided self-assembly of block-copolymer for CMOS technology: a comparative study between grapho-epitaxy and surface chemical modification," in *Proc. SPIE 7970, Alternative Lithographic Technologies III*, pp. 79700P-79700P-10, 2011.
[62] D. P. Sanders, J. Cheng, C. T. Rettner, W. D. Hinsberg, H.-C. Kim, H. Trung*, et al.*, "Integration of Directed Self-Assembly with 193 nm Lithography," *Journal of Photopolymer Science and Technology,* vol. 23, pp. 11-18, 2010.
[63] D. J. C. Herr, "Directed block copolymer self-assembly for nanoelectronics fabrication," *Journal of Materials Research,* vol. 26, pp. 122-139, 2011.
[64] C. Bencher, J. Smith, L. Miao, C. Cai, Y. Chen, J. Y. Cheng*, et al.*, "Self-Assembly Patterning for sub-15nm Half-Pitch: A Transition from Lab to Fab," in *Proc. SPIE 7970, Alternative Lithographic Technologies III*, San Jose, CA, 2011.
[65] B. W. Smith, H. Kang, A. Bourov, F. Cropanese, and Y. Fan, "Water immersion optical lithography for 45-nm node," in *Proc. SPIE 5040, Optical Microlithography XVI*, pp. 679-689, 2003.
[66] B. W. Smith, A. Bourov, Y. Fan, L. V. Zavyalova, N. V. Lafferty, and F. C. Cropanese, "Approaching the numerical aperture of water immersion lithography at 193-nm," in *Proc. SPIE 5377, Optical Microlithography XVII*, pp. 273-284, 2004.
[67] F. C. Cropanese, A. Bourov, Y. F. Fan, J. M. Zhou, L. Zavyalova, and B. W. Smith, "Synthetic defocus for interferometric lithography," in *Proc. SPIE 5754, Optical Microlithography XVIII*, San Jose, CA, pp. 1769-1779, 2005.
[68] B. W. Smith, A. Bourov, Y. F. Fan, F. Cropanese, and P. Hammond, "Amphibian XIS: An immersion lithography microstepper platform," in *Proc. SPIE 5754, Optical Microlithography XVIII*, San Jose, CA, pp. 751-759, 2005.
[69] A. Bourov, Y. F. Fan, and F. C. Cropanese, "Immersion microlithography at 193 nm with a Talbot prism interferometer," in *Proc. SPIE 5377, Optical Microlithography XVII*, Santa Clara, CA, pp. 1573-1578, 2004.
[70] S. H. Zaidi, S. R. J. Brueck, F. M. Schellenberg, R. S. Mackay, K. Uekert, and J. J. Persoff, "Interferometric lithography exposure tool for 180-nm structures," in *SPIE Proceedings Vol. 3048 Emerging Lithographic Technologies*, Santa Clara, Ca, pp. 248-254, 1997.
[71] H. H. Solak, C. David, J. Gobrecht, L. Wang, and F. Cerrina, "Multiple-beam interference lithography with electron beam written gratings," *Journal of Vacuum Science & Technology B,* vol. 20, pp. 2844-2848, Nov-Dec 2002.
[72] H. H. Solak, C. David, J. Gobrecht, V. Golovkina, F. Cerrina, S. O. Kim*, et al.*, "Sub-50 nm period patterns with EUV interference lithography," *Microelectronic Engineering,* vol. 67–68, pp. 56-62, 2003.
[73] A. Fernandez, J. Y. Decker, S. M. Herman, D. W. Phillion, D. W. Sweeney, and M. D. Perry, "Methods for fabricating arrays of holes using interference

lithography," *Journal of Vacuum Science & Technology B: Microelectronics and Nanometer Structures,* vol. 15, pp. 2439-2443, 1997.
[74] A. Bourov, Y. F. Fan, F. C. Cropanese, and B. W. Smith, "Photoresist modulation curves," in *Proc. SPIE 5754, Optical Microlithography XVIII*. vol. 5754, pp. 1762-1768, 2005.
[75] A. Bourov, S. A. Robertson, B. W. Smith, M. Slocum, and E. C. Piscani, "Experimental measurement of photoresist modulation curves," in *Proc. SPIE 6154, Optical Microlithography XIX*, San Jose, CA, pp. U2001-U2006, 2006.
[76] A. Bourov, S. A. Robertson, B. W. Smith, M. A. Slocum, and E. C. Piscani, "Resist process window characterization for the 45-nm node using an interferometric immersion microstepper," in *Proc. SPIE 6153, Advances in Resist Technology and Processing XXIII*, San Jose, CA, pp. U368-U378, 2006.
[77] J. A. Hoffnagle, W. D. Hinsberg, R. A. Houle, and M. I. Sanchez, "Characterization of photoresist spatial resolution by interferometric lithography," in *Proc. SPIE 5038, Metrology, Inspection, and Process Control for Microlithography XVII*, Santa Clara, Ca, pp. 464-472, 2003.
[78] W. K. Choi, T. H. Liew, M. K. Dawood, H. I. Smith, C. V. Thompson, and M. H. Hong, "Synthesis of Silicon Nanowires and Nanofin Arrays Using Interference Lithography and Catalytic Etching," *Nano Letters,* vol. 8, pp. 3799-3802, 2008.
[79] J. d. Boor, N. Geyer, J. V. Wittemann, U. Gösele, and V. Schmidt, "Sub-100 nm silicon nanowires by laser interference lithography and metal-assisted etching," *Nanotechnology,* vol. 21, 2010.
[80] J. J. Wang, F. Walters, X. Liu, P. Sciortino, and X. Deng, "High-performance, large area, deep ultraviolet to infrared polarizers based on 40 nm line/78 nm space nanowire grids," *Applied Physics Letters,* vol. 90, pp. 061104-061104-3, 2007.
[81] I. Divliansky, T. S. Mayer, K. S. Holliday, and V. H. Crespi, "Fabrication of three-dimensional polymer photonic crystal structures using single diffraction element interference lithography," *Applied Physics Letters,* vol. 82, pp. 1667-1669, 2003.
[82] H. C. Guo, D. Nau, A. Radke, X. P. Zhang, J. Stodolka, X. L. Yang*, et al.*, "Large-area metallic photonic crystal fabrication with interference lithography and dry etching," *Applied Physics B,* vol. 81, pp. 271-275, 2005.
[83] H. H. Solak, "Space-invariant multiple-beam achromatic EUV interference lithography," *Microelectronic Engineering,* vol. 78-79, pp. 410-416, Mar 2005.
[84] P. P. Naulleau, C. N. Anderson, and S. F. Horne, "Extreme ultraviolet interference lithography with incoherent light," in *Proc. SPIE 6517, Emerging Lithographic Technologies XI*, pp. 65172T-65172T-8, 2007.
[85] A. Bourov, "A systematic approach to determining the limits of nanolithography at extreme NA," *ProQuest Dissertations and Theses* pp. 96. 2008. ISBN: 9780549935469.
[86] J. A. Hoffnagle, W. D. Hinsberg, M. Sanchez, and F. A. Houle, "Liquid immersion deep-ultraviolet interferometric lithography," *Journal of Vacuum Science & Technology B: Microelectronics and Nanometer Structures,* vol. 17, 1999.
[87] M. Switkes and M. Rothschild, "Immersion lithography at 157 nm," *J. Vac. Sc. Technol. B,* vol. 19, 2001.

[88] T. A. Savas, S. N. Shah, M. L. Schattenburg, J. M. Carter, and H. I. Smith, "Achromatic interferometric lithography for 100-nm-period gratings and grids," *Journal of Vacuum Science & Technology B,* vol. 13, pp. 2732-2735, Nov-Dec 1995.

[89] A. Othonos and X. Lee, "Novel and improved methods of writing Bragg gratings with phase masks," *Photonics Technology Letters, IEEE,* vol. 7, pp. 1183-1185, 1995.

[90] D. Z. Anderson, V. Mizrahi, T. Erdogan, and A. E. White, "PRODUCTION OF IN-FIBER GRATINGS USING A DIFFRACTIVE OPTICAL-ELEMENT," *Electronics Letters,* vol. 29, pp. 566-568, Mar 18 1993.

[91] B. W. Smith, "Will IL be a Main-stream, Niche, or Impractical Solution," 2010 International Symposium on Lithography Extensions, 2010.

[92] J. Jacob, J. Burnett, and E. Benck, "Development of a Full-field Interference Lithography Demonstration System," 2010 International Symposium on Lithography Extensions:
http://www.sematech.org/meetings/archives/litho/8940/pres/IL_02_John%20Burnett.pdf

[93] P. Nikolsky, N. Davydova, and R. Goossens, "Topological and model based approach to pitch decomposition for double patterning," in *Proc. SPIE 6792, 24th European Mask and Lithography Conference*, pp. 679205-679205-12, 2008.

[94] R. T. Greenway, R. Hendel, K. Jeong, A. B. Kahng, J. S. Petersen, Z. Rao*, et al.*, "Interference Assisted Lithography for Patterning of 1D Gridded Design," in *Proc. SPIE 7271, Alternative Lithographic Technologies*, San Jose, CA, 2009.

[95] M. Fritze, B. Tyrrell, D. Astolfi, D. Yost, P. Davis, B. Wheeler*, et al.*, "Gratings of regular arrays and trim exposures for ultralarge scale integrated circuit phase-shift lithography," *Journal of Vacuum Science & Technology B,* vol. 19, pp. 2366-2370, Nov-Dec 2001.

[96] M. Fritze, T. M. Bloomstein, B. Tyrrell, T. H. Fedynyshyn, N. N. Efremow, D. E. Hardy*, et al.*, "Hybrid optical maskless lithography: Scaling beyond the 45 nm node," *Journal of Vacuum Science & Technology B,* vol. 23, pp. 2743-2748, Nov-Dec 2005.

[97] C. A. Mack, "Impact of mask roughness on wafer line-edge roughness," in *Proc. SPIE 7488, Photomask Technology*, 2009.

[98] Y. Wei and R. L. Brainard, *Advanced Processes for 193-nm Immersion Lithography,* DOI: 10.1117/3.820233: SPIE, 2009.

[99] M. Chandhok, S. Datta, D. Lionberger, and S. Vesecky, "Impact of line-width roughness on Intel's 65-nm process devices," in *Proc. SPIE 6519, Advances in Resist Materials and Processing Technology XXIV*, pp. 65191A-65191A-6, 2007.

[100] J. Zhou, "Hyper-NA Imaging in Optical Lithography at Oblique Angles," Ph. D. Dissertation, Microsystems Engineering, Rochester Institute of Technology, 2008.

[101] Y. Fan, "Pushing the limits of Hyper-NA optical lithography," Ph. D. Dissertation, Microsystems Engineering, Rochester Institute of Technology, 2005.

[102] A. Lagrange, P. Bandelier, C. Charpin, and O. Lartigue, "Contrast management of 193i interferometry to be close to scanners contrast conditions," in *Proc. SPIE 6924, Optical Microlithography XXI*, pp. 69242G-69242G-10, 2008.

[103] K. Singh and R. Rattan, "Images of an incoherent annulus in the presence of transverse sinusoidal vibrations," *Pramana,* vol. 6, pp. 109-115, 1976.

[104] J. Xiao, M. Khan, R. Nachman, J. Wallace, Z. Chen, and F. Cerrina, "Modeling image formation: Application to mask optimization," *Journal of Vacuum Science & Technology B: Microelectronics and Nanometer Structures,* vol. 12, pp. 4038-4043, 1994.
[105] A. Stern and N. S. Kopeika, "Analytical method to calculate optical transfer functions for image motion and vibrations using moments," *JOSA A, Vol. 14, Issue 2, pp. 388-396,* 1997.
[106] B. J. Lin, "Vibration Tolerance in Optical Imaging," in *Proc. SPIE 1088, Optical/Laser Microlithography II*, pp. 106-114, 1989.
[107] B. J. Lin, "VIBRATION TOLERANCE IN OPTICAL IMAGING," *Optical Engineering,* vol. 32, pp. 527-535, Mar 1993.
[108] E. Hecht, *Optics (4th Edition)*: Addison-Wesley, 2001.
[109] H. B. Cao, W. Yueh, B. J. Rice, J. Roberts, T. Bacuita, and M. Chandhok, "Sources of line-width roughness for EUV resists," in *Proc. SPIE 5376, Advances in Resist Technology and Processing XXI*, pp. 757-764, 2004.
[110] T. Sandstrom and C. Rydberg, "Sources and scaling laws for LER and LWR," in *Proc. SPIE 6520, Optical Microlithography XX*, San Jose, CA, pp. X5200-X5200, 2007.
[111] C. Mack, *Field Guide to Optical Lithography*: SPIE Press Book, 2006.
[112] C. A. Mack, "Line-edge roughness and the ultimate limits of lithography," in *Proc. SPIE 7639*, pp. 763931-763931-16, 2010.
[113] O. Noordman, A. Tychkov, J. Baselmans, J. Tsacoyeanes, G. Politi, M. Patra*, et al.*, "Speckle in optical lithography and its influence on linewidth roughness," *Journal of Micro-Nanolithography Mems and Moems,* vol. 8, Oct-Dec 2009.
[114] R. D. Peters, G. Amblard, J. J. Lee, and T. Guenther, "Ultra-thin photoresists for 193 nm lithography," in *Proc. SPIE 5039, Advances in Resist Technology and Processing XX*, Santa Clara, Ca, pp. 393-403, 2003.
[115] J. H. Kim, N. Choi, Y.-H. Kim, and T.-S. Kim, "Thickness dependence of the lithographic performance in 193nm photoresists," in *Proc. SPIE 6153, Advances in Resist Technology and Processing XXIII*, San Jose, CA, pp. U1256-U1263, 2006.
[116] J. Shin, G. Han, Y. Ma, K. Moloni, and F. Cerrina, "Resist line edge roughness and aerial image contrast," *Journal of Vacuum Science & Technology B,* vol. 19, pp. 2890-2895, Nov-Dec 2001.
[117] M. I. Sanchez, W. D. Hinsberg, F. A. Houle, J. A. Hoffnagle, H. Ito, and C. Nguyen, "Aerial image contrast using interferometric lithography: Effect on line-edge roughness," in *Proc. SPIE 3678, Advances in Resist Technology and Processing XVI*, Santa Clara, Ca, pp. 160-171, 1999.
[118] S. A. Robertson, J. M. Leonard, B. W. Smith, and A. Bourov, "Comparison of immersion lithography from projection and interferometric exposure tools," in *Proc. SPIE 6154, Optical Microlithography XIX*, San Jose, CA, pp. U2568-U2576, 2006.
[119] J.-Y. Lee, J. Shin, H.-W. Kim, S.-G. Woo, H.-K. Cho, W.-S. Han*, et al.*, "Effect of line-edge roughness (LER) and line-width roughness (LWR) on sub-100-nm device performance," in *Proc. SPIE 5376*, pp. 426-433, 2004.

[120] P. Xie, H. Ren, A. Nainani, H. Dai, C. Bencher, and C. Ngai, "Understanding device impact of line edge/width roughness in frequency domain," in *Proc. SPIE 8684, Design for Manufacturability through Design-Process Integration VII*, pp. 86840J-86840J-7, 2013.

[121] A. V. Pret, R. Gronheid, T. Graves, M. D. Smith, and J. Biafore, "Mask absorber roughness impact in extreme ultraviolet lithography," *Journal of Micro/Nanolithography, MEMS, and MOEMS,* vol. 10, pp. 023012-023012-5, 2011.

[122] A. Vaglio Pret and R. Gronheid, "Mask line roughness contribution in EUV lithography," *Microelectronic Engineering,* vol. 88, pp. 2167-2170, 2011.

[123] P. P. Naulleau and G. M. Gallatin, "Line-Edge Roughness Transfer Function and its Application to Determining Mask Effects in EUV Resist Characterization," *Applied Optics, Vol. 42, Issue 17, pp. 3390-3397,* 2003.

[124] P. P. Naulleau, "Relevance of Mask-Roughness-Induced Printed Line-Edge Roughness in Recent and Future Extreme-Ultraviolet Lithography Tests," *Applied Optics, Vol. 43, Issue 20, pp. 4025-4032,* 2004.

[125] H. Tanabe, G. Yoshizawa, Y. Liu, V. L. Tolani, K. Kojima, and N. Hayashi, "LER transfer from a mask to wafers," in *Proc. SPIE 6607, Photomask and Next-Generation Lithography Mask Technology XIV*, Yokohama, JAPAN, pp. H6071-H6071, 2007.

[126] K. Garidis, "Mask absorber roughness impact on EUV and 193 nm immersion lithography," M. Sc. Thesis, Nanotechnology, Kungliga Tekniska Hogskolan (Sweden), 2011.

[127] K. Garidis, A. V. Pret, and R. Gronheid, "Mask roughness impact on extreme UV and 193nm immersion lithography," *Microelectronic Engineering,* vol. 98, pp. 138-141, 2012.

[128] P. P. Naulleau, S. A. George, and B. M. McClinton, "Mask roughness and its implications for LER at the 22- and 16nm nodes," in *Proc. SPIE 7636, Extreme Ultraviolet (EUV) Lithography*, pp. 76362H-76362H-7, 2010.

[129] A. V. Pret, R. Gronheid, T. Graves, M. D. Smith, and J. Biafore, "Impact of mask line roughness in EUV lithography," in *Proc. SPIE 7969, Extreme Ultraviolet (EUV) Lithography II*, pp. 79691T-79691T-7, 2011.

[130] P. P. Naulleau and S. A. George, "Implications of image plane line-edge roughness requirements on extreme ultraviolet mask specifications," in *Proc. SPIE 7379, Photomask and Next-Generation Lithography Mask Technology XVI*, pp. 73790O-73790O-11, 2009.

[131] A. Vaglio Pret and R. Gronheid, "Line Width Roughness mitigation in chemically amplified resist by post-litho processes," *Microelectronic Engineering,* vol. 87, pp. 1127-1130, 2010.

[132] L. Azarnouche, E. Pargon, K. Menguelti, M. Fouchier, M. Brihoum, R. Ramos*, et al.*, "Plasma treatment to improve linewidth roughness during gate patterning," in *Proc. SPIE 8328, Advanced Etch Technology for Nanopatterning*, pp. 83280H-83280H-11, 2012.

[133] A. Vaglio-Pret, R. Gronheid, and P. Foubert, "Roughness characterization in the frequency domain and LWR mitigation with post-litho processes," in *Proc. SPIE*

7639, Advances in Resist Materials and Processing Technology XXVII, pp. 763930-763930-9, 2010.
[134] P. Foubert, A. V. Pret, E. A. Sanchez, and R. Gronheid, "Impact of post-litho linewidth roughness smoothing processes on the post-etch patterning result," *Journal of Micro/Nanolithography, MEMS, and MOEMS,* vol. 10, pp. 033001-033001-6, 2011.
[135] C. Rydberg, J. Bengtsson, and T. Sandstrom, "Dynamic laser speckle as a detrimental phenomenon in optical projection lithography," *Journal of Microlithography Microfabrication and Microsystems,* vol. 5, Jul-Sep 2006.
[136] T. Sandstrom and C. Rydberg, "Dynamic laser speckle in optical projection lithography: causes, effects on CDU and LER, and possible remedies," in *Proc. SPIE 5754, Optical Microlithography XVIII*, San Jose, CA, pp. 274-284, 2005.
[137] O. Kritsun, I. Lalovic, S. Rokitski, B. Partlo, B. La Fontaine, N. Farrar*, et al.*, "Improving lithography pattern fidelity and line-edge roughness by reducing laser speckle," *Journal of Vacuum Science & Technology B,* vol. 26, pp. 2145-2150, Nov 2008.
[138] H. Fukuda, T. Terasawa, and S. Okazaki, "Spatial filtering for depth of focus and resolution enhancement in optical lithography," *Journal of Vacuum Science & Technology B: Microelectronics and Nanometer Structures,* vol. 9, pp. 3113-3116, 1991.
[139] G. McIntyre, L. Teeuwen, E. Sohmen, O. Wood, D. Corliss, T. v. d. Akker*, et al.*, "Enhancing resolution with pupil filtering for projection printing systems with fixed or restricted illumination angular distribution," in *Proc. SPIE 8679, Extreme Ultraviolet (EUV) Lithography IV*, pp. 86792N-86792N-15, 2013.
[140] M. K. Sears, J. Bekaert, and B. W. Smith, "Lens wavefront compensation for 3D photomask effects in subwavelength optical lithography," *Applied Optics, Vol. 52, Issue 3, pp. 314-322,* 2013.
[141] Y.-P. Chen, C.-H. Chen, J.-H. Chang, H.-C. Chiu, G.-Y. Chen, C.-H. Chiang*, et al.*, "Stitching periodic submicron fringes by utilizing step-and-align interference lithography," *Journal of Vacuum Science & Technology B,* vol. 27, pp. 2951-2957, Nov 2009.
[142] M. L. Schattenburg, C. G. Chen, R. K. Heilmann, P. T. Konkola, and G. S. Pati, "Progress towards a general grating patterning technology using phase-locked scanning beams," in *Proc. SPIE 4485, Optical Spectroscopic Techniques, Remote Sensing, and Instrumentation for Atmospheric and Space Research IV*, San Diego, Ca, pp. 378-384, 2001.
[143] J. C. Montoya, C. H. Chang, R. K. Heilmann, and M. L. Schattenburg, "Doppler writing and linewidth control for scanning beam interference lithography," *Journal of Vacuum Science & Technology B,* vol. 23, pp. 2640-2645, Nov-Dec 2005.
[144] P. T. Konkola, C. G. Chen, R. K. Heilmann, and M. L. Schattenburg, "Beam steering system and spatial filtering applied to interference lithography," *Journal of Vacuum Science & Technology B,* vol. 18, pp. 3282-3286, Nov-Dec 2000.
[145] T. A. Savas, M. L. Schattenburg, J. M. Carter, and H. I. Smith, "Large-area achromatic interferometric lithography for 100 nm period gratings and grids,"

Journal of Vacuum Science & Technology B, vol. 14, pp. 4167-4170, Nov-Dec 1996.
[146] A. Yen, E. H. Anderson, R. A. Ghanbari, M. L. Schattenburg, and H. I. Smith, "ACHROMATIC HOLOGRAPHIC CONFIGURATION FOR 100-NM-PERIOD LITHOGRAPHY," *Applied Optics,* vol. 31, pp. 4540-4545, Aug 1 1992.
[147] R. R. Hershey and E. N. Leith, "GRATING INTERFEROMETERS FOR PRODUCING LARGE HOLOGRAPHIC GRATINGS," *Applied Optics,* vol. 29, pp. 937-943, Mar 1990.
[148] H. Amick, "On generic vibration criteria for advanced technology facilities," *Journal of the Institute of Environmental Sciences,* vol. 40, pp. 35-44, Sep-Oct 1997.
[149] C. G. Gordon, "GENERIC CRITERIA FOR VIBRATION-SENSITIVE EQUIPMENT," in *Proc. SPIE 1619, Vibration Control in Microelectronics, Optics, and Metrology*, San Jose, Ca, 1992, pp. 71-85.
[150] M. Weber. (2012). *Piezoelectric Accelerometers*. Available:
http://www.mmf.de/pdf/an1e-introduction.pdf
[151] C. G. Gordon, "Generic vibration criteria for vibration-sensitive equipment," in *Proc. SPIE 3786, Optomechanical Engineering and Vibration Control*, pp. 22-33, 1999.
[152] A. Lagrange, A. L. Charley, O. Lartigue, and M. Derouard, "Assembly of a 193-nm interferometer for immersion lithography: vibration effects on image contrast," in *Proc. SPIE 6154, Optical Microlithography XIX*, pp. 61544O-61544O-5, 2006.
[153] *KLA Tencor PROLITH Lithography Simulation Tool – Computational Lithography and Photolithography Simulation* Available:
http://www.kla-tencor.com/lithography-modeling/chip-prolith.html
[154] *EUV Technology Corporation SuMMIT Home Page*. Available:
http://www.lithometrix.com/summit.htm
[155] MathWorks. *MATLAB - The Language of Technical Computing*. Available:
http://www.mathworks.com/products/matlab/
[156] F. Staals, A. Andryzhyieuskaya, H. Bakker, M. Beems, J. Finders, T. Hollink*, et al.*, "Advanced wavefront engineering for improved imaging and overlay applications on a 1.35 NA immersion scanner," in *Proc. SPIE 7973, Optical Microlithography XXIV*, pp. 79731G-79731G-13, 2011.
[157] M. K. Sears, "Pupil wavefront manipulation for the compensation of mask topography effects in optical nanolithography," Ph. D. Dissertation, Rochester Institute of Technology, *ProQuest Dissertations and Theses*, 2013.
[158] B. Gustavsson (2010). *Optical_bench - File Exchange - MATLAB Central*. Available:
http://www.mathworks.com/matlabcentral/fileexchange/file_infos/27412-opticalbench
[159] *ITRS 2007 Lithography Edition*. Available:
http://www.itrs.net/Links/2007ITRS/2007_Chapters/2007_Lithography.pdf
[160] B. W. Smith, E-mail communication on different IL approaches, 2011.